

# **Modified-Release Formulations for Cancer Therapy**

By

Moustafa M. Abdelaziz

B.Sc., University of Science and Technology – Zewail City, 2017

Submitted to the graduate degree program in Bioengineering and the Graduate Faculty of the University of Kansas in partial fulfillment of the requirements for the degree of Master of Science.

---

Chairperson: Dr. M. Laird Forrest

---

Dr. Stevin Gehrke

---

Dr. Mark Farrell

Date Defended: 27 April 2022

The Thesis Committee for Moustafa M. Abdelaziz certifies that this is the approved version of the following thesis:

**Modified-Release Formulations for Cancer Therapy**

---

Chairperson: Dr. M. Laird Forrest

Date Approved: 27 April 2022

## Abstract

Cancer is one of the most virulent diseases in modern times that is ranked as the second leading cause of death worldwide. The conventional and modern treatment protocols (e.g. chemotherapy and immunotherapy) for cancer still have some drawbacks that range from mild adverse effects to limited efficacy and the risk of tumor recurrence. Long-acting depots can mitigate these drawbacks and lend the current therapeutic protocols with improved efficacy and safety through their numerous advantages such as localizing the drug administration, prolonging the drug exposure, protecting the drug against degradation, conferring targeting functionality, and reducing side effects. Therefore, the utilization of long-acting depots for cancer therapy was investigated in this thesis. The first chapter describes the long-acting depots concerning their definition, historical development, advantages, and the major classes that are prevalent in the pharmaceutical market.

The second and third chapters present the utilization of long-acting depots for cancer immunotherapy. The second chapter discusses the development of multivesicular liposomes (MVLs) for the localized depot delivery of ingenol-3-angelate (I3A), a protein kinase C agonist. The *in vitro* release study, *in vitro* cytotoxicity assay, and the *in vivo* pharmacokinetics demonstrated the potential MVLs to overcome I3A's poor solubility, sustain drug release, and prevent the rapid clearance from the injection site. The third chapter describes the use of the ethyl oleate (EO) oil vehicle for prolonging the release of two developed kifunensine (KIF), named JDW-II-002 and JDW-II-008. These analogues act as potent inhibitors of type I mannosidase and potential agents for cancer immunotherapy. The therapeutic efficiency of the developed formulation was examined using an immunocompetent mice model of colon cancer which showed a delay in the tumor growth with JDW-II-008 treatments. The immunohistochemistry analysis demonstrated overexpression of high mannose N-glycans with all KIF treatments and an indication

of a possible antitumor immune response. While chapter four discusses a photodynamic therapy (PDT) approach for the treatment of head and neck squamous cell carcinoma (HNSCC). In that chapter, we relied on an alternative approach to long-acting depots, in which we developed hyaluronan nanoconjugates to enhance the specific tumor cells' uptake and retention of the photosensitizer, pyropheophorbide-a (PPa). The results demonstrated improvement in the water solubility of PPa, increase in its accumulation in HNSCC, and preservation of its photoactivity. The *in vivo* efficacy and survival time of the developed formulation were statistically better than conventional PDT therapy. Accordingly, we believe in the long-acting depots' potential to substantially contribute to the pursuit of next-generation cancer therapeutics.

## Acknowledgments

First and foremost, I would like to express my sincere gratitude to my research advisor, Dr. Laird Forrest, for his guidance, patience, flexibility, and continuous support throughout the master's degree journey. He allowed me to use his lab resources and gave me the chance to independently explore through various research projects. Thanks to him and his group members, I learned many characterization techniques, biological assays, and animal models. I would like to deeply thank the members of Dr. Forrest's lab and HylaPharm LLC: Mark Craven, Derek Mull, Dr. Chad Groer, and Dr. Sasha Wu. I shared most of my time with you in the lab and I appreciate all the friendly and scientific conversations we had over the last two years. I wish you happiness and success in your life.

I would also like to thank my committee members, Dr. Stevin Gehrke and Dr. Mark Farrell, for their valuable time and insightful feedback on the thesis and the defense. To the Department of Bioengineering's faculty and administrative officers, thank you for your immense knowledge provided to me through the academic classes I took in my master's, which helped me shape my scientific experience and research interests. Special thanks go to the Bioengineering Program Director, Dr. Ken Fischer for his wise advice, understanding, and professional communication with the Fulbright program. Also, special thanks go to the Binational Fulbright Commission in Egypt - Fulbright Egyptian Student Program. They helped me to get a visa in the middle of the COVID-19 crisis when getting one was very difficult at that unprecedented time. I owe them for being here at KU.

I would also like to thank our collaborators: Dr. Mark Farrell and Dr. David Akhavan, for the informative discussions and fruitful suggestions that contributed to the work in this thesis. Also, many thanks go to all my colleagues and faculty who supported my research including but

not limited to Aric Huang, Dr. Justin Douglas, Dr. Noraida Martinez-Rivera, Dr. Islam Khalil, Huan Gong, and Dr. Prashant Kumar.

Finally, I want to thank my family and my friends. To my fiancée, Esraa, I cannot find enough words to express my gratitude for being by my side over these two years. You cared a lot and spared no effort in offering help and advice when needed. I deeply appreciate the daily support and the long conversations to go to the school or the lab and get it together. To my family, special thanks for your endless care, support, and motivation. This accomplishment is the result of all the love you gave to me over the years. To my lovely mom, I hope I made you a little proud of your son. To my lifelong friends, I am too lucky to have loyal and good friends like you. You are partners in that humble accomplishment, and I could not make it to that point without your support.

Words cannot express how much you all mean to me.

Thank you so much!

## Table of Contents

Abstract .....	iii
Acknowledgments .....	v
Table of Contents .....	vii
Chapter I: Introduction.....	1
1.1 Immediate-release formulations .....	2
1.2 Modified-release formulations .....	4
1.2.1 Terminology.....	4
1.2.2 Historical perspective .....	6
1.2.3 Advantages.....	7
1.3 Major classes of long-acting depot formulations in the market .....	9
1.4 Long-acting depot formulations for cancer therapy .....	23
1.5 Conclusion.....	26
1.6 References .....	27
Chapter II: Development of long-acting multivesicular liposomes for the localized depot delivery of Ingenol-3-Angelate .....	39
2.1 Introduction .....	40
2.2 Materials and Methods.....	42
2.2.1 Materials.....	42
2.2.2 Preparation of MVLS .....	43
2.2.3 MVLS particle characterization.....	44
2.2.4 Confirmation of I3A complexation with SBE- $\beta$ -CD .....	45
2.2.5 HPLC method.....	45
2.2.6 Determination of entrapment efficiency .....	46
2.2.7 <i>In vitro</i> release profile.....	46
2.2.8 <i>In vitro</i> cytotoxicity assay .....	47
2.2.9 <i>In vivo</i> pharmacokinetics study.....	48
2.2.10 Statistical analysis.....	50
2.3 Results .....	51
2.3.1 MVLS particle characterization.....	51
2.3.2 Confirmation of I3A complexation with SBE- $\beta$ -CD .....	53

2.3.3 HPLC method validation .....	54
2.3.4 MVL entrapment efficiency and <i>in vitro</i> release behavior.....	57
2.3.5 <i>In vitro</i> cytotoxicity assay .....	58
2.3.6 <i>In vivo</i> pharmacokinetic study .....	59
2.4 Discussion.....	64
2.5 Conclusion.....	69
2.6 Funding .....	69
2.7 Acknowledgments.....	70
2.8 References .....	71
<b>Chapter III: Development of long-acting formulations for Kifunensine analogues as potent inhibitors of type I mannosidase and potential agents for cancer immunotherapy .....</b>	<b>79</b>
3.1 Introduction .....	80
3.2 Materials and Methods.....	82
3.2.1 Materials.....	82
3.2.2 HPLC method.....	83
3.2.3 Determination of oil-buffer distribution coefficient.....	84
3.2.4 Development of formulation strategy .....	85
3.2.5 <i>In vivo</i> antitumor activity .....	88
3.2.6 Immunohistochemistry analysis for immune markers .....	89
3.2.7 Statistical analysis .....	91
3.3 Results .....	92
3.3.1 HPLC method validation .....	92
3.3.2 Determination of oil-buffer distribution coefficient.....	92
3.3.3 Development of formulation strategy .....	93
3.3.4 <i>In vivo</i> antitumor activity .....	98
3.3.5 Immunohistochemistry analysis for immune markers .....	99
3.4 Discussion.....	106
3.5 Conclusion.....	109
3.6 Funding .....	109
3.7 Acknowledgments.....	110
3.8 References .....	111



<b>Chapter IV: Hyaluronic acid carrier-based photodynamic therapy for head and neck squamous cell carcinoma .....</b>	<b>115</b>
<b>4.1 Introduction .....</b>	<b>116</b>
<b>4.2 Materials and Methods.....</b>	<b>118</b>
4.2.1 Materials.....	118
4.2.2 Synthesis and Characterization of HA-ADH-PPa.....	119
4.2.3 Singlet Oxygen Generation .....	121
4.2.4 Cellular Uptake and Exclusion .....	121
4.2.5 Cellular Localization .....	122
4.2.6 <i>In Vitro</i> Phototoxicity .....	123
4.2.7 <i>In Vivo</i> Fluorescence Imaging .....	123
4.2.8 <i>In Vivo</i> PDT Treatment.....	124
4.2.9 Statistical Analysis.....	124
<b>4.3 Results .....</b>	<b>125</b>
4.3.1 Synthesis and Physical Characterization of HA-ADH-PPa Conjugate.....	125
4.3.2 Singlet oxygen generation of PPa from HA-ADH-PPa .....	128
4.3.3 Cellular Internalization and Exclusion of HA-ADH-PPa and PPa in MDA-1986 Cells .....	129
4.3.4 Cellular Localization of HA-ADH-PPa Vs free PPa .....	130
4.3.5 Cellular Phototoxicity of HA-ADH-PPa.....	132
4.3.6 <i>In Vivo</i> Fluorescence Imaging .....	135
4.3.7 <i>In Vivo</i> PDT Treatment.....	136
<b>4.4 Discussion.....</b>	<b>138</b>
<b>4.5 Conclusion.....</b>	<b>141</b>
<b>4.6 Funding .....</b>	<b>142</b>
<b>4.7 Acknowledgments.....</b>	<b>142</b>
<b>4.8 References .....</b>	<b>143</b>

## **Chapter I: Introduction**

## 1.1 Immediate-release formulations

An ideal drug delivery system (DDS) will administer the active pharmaceutical ingredient (API) to the site of disease at a predetermined concentration within the therapeutic range for a period that is appropriate for the disease type.<sup>1-3</sup> A DDS should also be biocompatible, biodegradable at an appropriate rate to the API release, and not harmfully interact with the API (i.e. affect stability).<sup>4,5</sup> The long-term goal of developing a DDS is to be translated into a clinical application, where it can improve patients' health and wellbeing. For that to occur, API should be formulated in an appropriate DDS in which they show promising *in vitro* results that are correlated with the *in vivo* pharmacokinetics and pharmacodynamics.<sup>6</sup> The whole process is summarized in **Figure 1**.

DDSs can be categorized according to their release mode as immediate and modified release systems. Historically, most DDSs were the immediate type, where they released the payload once came into contact with body fluids.<sup>7</sup> Immediate-release DDS allows quick attainment of therapeutic concentration, but concentrations may not stay within the therapeutic window for very long, especially for drugs having a rapid clearance rate.<sup>8</sup> Immediate-release DDS is useful when the disease condition requires quick intervention (e.g. acute diseases and painkillers).<sup>9</sup> Otherwise, frequent administration of such formulation is required to maintain a therapeutic concentration. In addition, issues associated with immediate-release forms include variation in API plasma concentration, which may risk having systemic toxicity, a requirement of patient adherence to dosing regimen, and the possibility of invasive multiple administrations, e.g. for injectables.<sup>8,10</sup> Thus, modified-release formulations have emerged as a potential solution for some problems associated with immediate-release dosage forms, especially when long-term treatment (i.e. chronic) is required.<sup>11,12</sup>

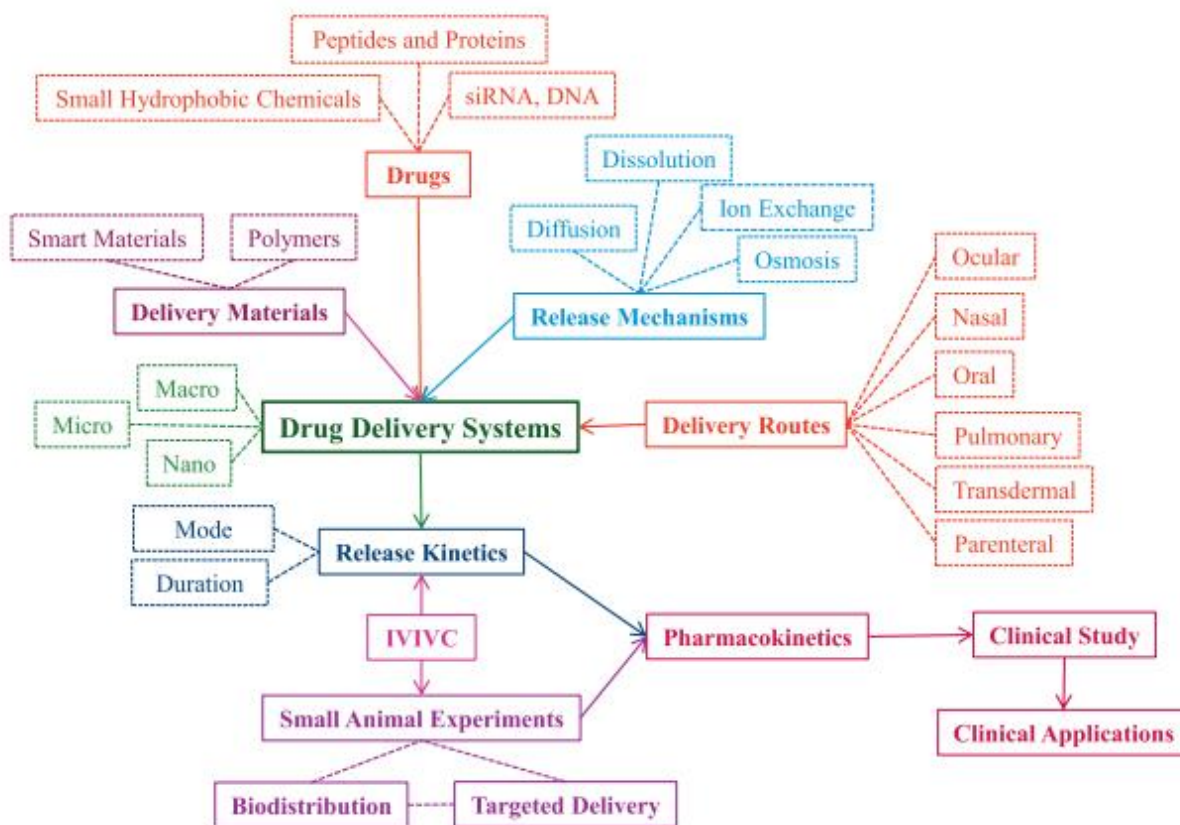


**Figure 1** The process of drug delivery from choosing the API and drug delivery vehicle to the translation into clinical applications. (Used with permission from <sup>6</sup>).

## 1.2 Modified-release formulations

### 1.2.1 Terminology

As the name suggests, modified-release formulation refers to a modification in the API release rate as opposed to the immediate-release DDSs. The family of modified-release involves other commonly used terms such as delayed-release, sustained-release, extended-release, controlled-release, long-acting formulation, depot formulation, and others.<sup>13,14</sup> Although most of them are synonyms, a few of them have marginal differences. For instance, delayed-release is different than extended-release. A delayed-release is an immediate release profile, but with a defined lag time. The amount of delayed time may depend on a specific change in the formulation environment such as pH, for example in the case of enteric coating. In that case, API release is delayed until enteric coating erodes after passing the acidic stomach media and reaching the neutral intestines, which is beneficial to protect API from acidic media and protect the stomach mucosa from adverse effects of the API.<sup>15</sup> On the other hand, extended-release DDSs prolong the API release over a longer duration of time, starting the release from the zero point (**Figure 2**). The United States Pharmacopeia (USP) deals with controlled, prolonged, extended, sustained, and long-acting releases as synonyms, and they are distinguished by sustaining the API release over a long duration compared to the immediate-release DDSs. However, they only allow the term “extended-release” for official article titles.<sup>13</sup> Whether they indicate a particular period of release, generally, these terms indicate that the modified release profile allows for a reduction in the frequency of dose administration. Thus, release may occur over hours or even days, as long as it allows for a reduction in dose frequency.<sup>16</sup> In this thesis, the modified-release term is used as the parent of that family, while extended, sustained, and prolonged are used interchangeably to

describe the same approach. We will rely more on the term “long-acting depot formulations” to refer to the injectable localized delivery of therapeutics.

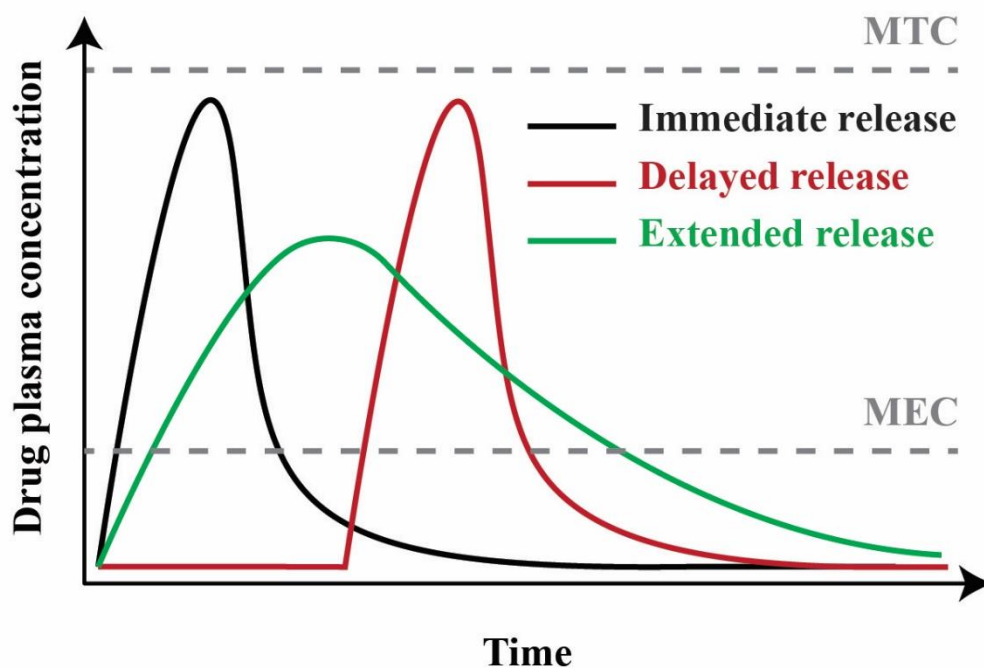


**Figure 2** Schematic diagram showing the difference between immediate-release, delayed-release, and extended-release drug delivery vehicles with respect to their behavior in releasing API over time. MTC stands for minimum toxic concentration, whereas MEC stands for minimum effective concentration.

### 1.2.2 Historical perspective

The development of modified-release formulations can be grouped into three generations from 1950 to today, that follow the building of our understanding of the physicochemical and biological barriers that need to be dealt with to control the drug release. The first-generation (G1) began in the 1950s when Smith, Kline & French company developed Dexedrine®, a twice-a-day modified-release product of dextroamphetamine.<sup>17</sup> The first generation lasted until the 1970s, and new developments and innovations were mainly for the oral and transdermal routes of administration in which they dealt with physiochemical barriers to delivery. Oral products reduced the frequency of administration to twice or once per day, while some transdermal products extended the dosing to a once per week. The major release mechanisms of G1 products were dissolution-controlled and diffusion-controlled, while other products showed different release mechanisms such as osmosis-controlled and ion-exchange formulations.<sup>7</sup> The second-generation (G2) of modified-release products development, which lasted from 1980 – 2010, included various new technologies and release mechanisms. Major efforts included the development of zero-order release kinetic technologies as it was hypothesized that this could sustain the release in the bloodstream and maximize efficacy and safety. However, the development of zero-order DDSs did not show the expected success in maintaining a constant API concentration because of the influence of absorption kinetics.<sup>6</sup> G2 technologies introduced the delivery of many biotechnological APIs such as proteins and nucleic acids, which required parental administration due to their poor stability and short half-life.<sup>18,19</sup> Nanoparticles technology was also part of G2; they were hypothesized to improve the localization and targeting of APIs using their unique properties (e.g. enhanced permeability and retention).<sup>20</sup> The concept of stimuli-responsive DDSs is also a member of G2 in which biocompatible and biodegradable polymers were utilized as smart

systems to respond to external stimuli (e.g. pH and temperature).<sup>21</sup> Although all these technologies showed impressive results in the lab, the number of concepts that were clinically translated into market products was much lower than G1.<sup>6</sup> One reason is that some technologies failed to consider the biological barriers associated with the condition they treat. For instance, insulin was developed for the pulmonary route of administration (Exubera<sup>®</sup>) as a modified-release DDS. Although the product negates the need for invasive injections, the developed system failed to consider the low absorption in the lungs compared to direct IV injections. This fact led to frequent daily doses, low patient compliance, and some adverse effects, which result in the withdrawal of the product from the market. In addition, the system failed to consider patient convenience, e.g. many patients found that a small autoinjector pen is more convenient and easy to use than a large, bulk inhalation device.<sup>22</sup> Therefore, a third-generation (G3) that is capable of addressing both the physicochemical and biological barriers is required to have better-modified-release DDSs. Some of the G3 products may target the API to the infection site to avoid adverse effects, while other systems may be capable of controlling the release according to the body's demand.<sup>6</sup>

### **1.2.3 Advantages**

The use of modified-release formulations is recommended in the case of chronic diseases, such as heart diseases and diabetes, that usually require frequent dosing, as it could reduce the dosing frequency and help improve patient adherence to the dosing regimen.<sup>11</sup> Modified-release DDSs are also useful when a constant systemic concentration is desired such as in chemotherapy and anesthetics.<sup>23</sup> The advantages of modified-release formulations are numerous and benefit the patients, healthcare providers, and pharmaceutical manufacturers. One main advantage of modified-release formulations is maintaining the API plasma concentrations within the therapeutic window, which protects patients from the occurrence of adverse effects if drug concentration



accidentally exceeds minimum toxic concentration (MTC), or low treatment efficacy if the drug concentration goes below the minimum effective concentration (MEC).<sup>24</sup> Also, the controlled exposure of API within the therapeutic window for an extended time could help improve the poor physicochemical properties of some APIs such as rapid clearance or low absorption. This effect is more observed with biotechnological APIs such as proteins and nucleic acids which exhibit poor stability and short half-life.<sup>25</sup>

Another advantage of the modified-release formulations that benefits both patients and healthcare providers is the reduced dosing frequency. From the patients' point of view, modified-release formulations boost their compliance to the dosing regimen by offering fewer doses, fewer reminders of taking doses, and thus better adherence to the dose regimen and normal daily routine. All these benefits can contribute to improved therapeutic outcomes. Likewise, for healthcare providers, improved patients' adherence to dosing regimens implies better treatment success rates, reduced stress on the healthcare facilities, capacity to accept new patients, and less overall economic burden.<sup>26</sup> Moreover, modified-release formulations hold potential for infection sites with limited API penetration such as joints, the brain, and the bladder. They can localize the API administration by direct injections into these deep tissues, which leads to better exposure to a given API dose than if it was coming from systemic delivery.<sup>27,28</sup> Local administration can also confer targeting functionality to the tissue of interest, and thus diminish the incidence of systemic toxicities which could be severe for patients. For instance, taxanes, a common family of chemotherapeutics, have very limited aqueous solubility and they were associated with many adverse effects. When they were locally administered with polymeric nanoparticles as a form of modified-release formulations, an improved tolerability was observed compared to the conventional formulations that used low molecular weight surfactants (i.e. Tween 80®).<sup>29</sup> In

regards to pharmaceutical companies, some modified-release formulations are cost-effective, simple to manufacture, and exhibit more reproducible release profiles than their counterparts in the immediate-release formulations. However, this is not always the case.<sup>30</sup> In this chapter, we will focus on injectable long-acting formulations that were or are still being explored clinically as they resemble the type of formulations developed in the following chapters.

### 1.3 Major classes of long-acting depot formulations in the market

Several long-acting depot formulations have demonstrated potential for controlling drug release over the last 70 years. However, not all of them were able to make it to the market or at least to later phases of clinical trials. In this section, we will highlight the major classes of such formulations whose products were approved by the U.S. Food and Drug Administration (FDA). These classes represent around 90% of the approved injectable depot formulations (**Figure 3**).<sup>25</sup> We will describe these major injectable depot classes, their sustained release mechanisms, advantages, and limitations.

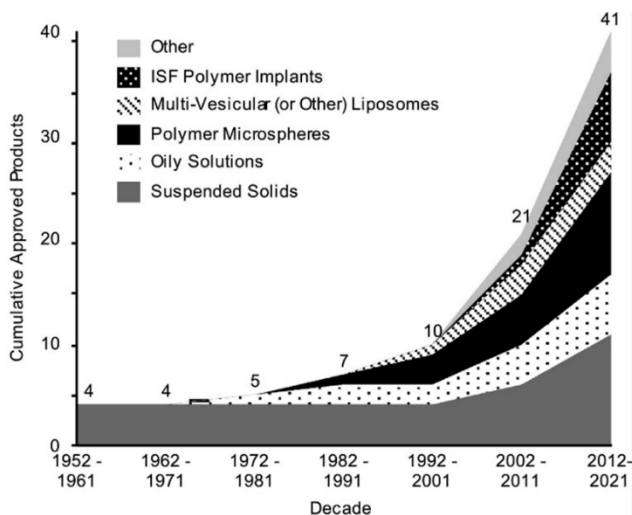


**Figure 3** The cumulative number of FDA approved long-acting depot formulations over the last 70 years. (Used with permission from <sup>25</sup>).

#### 1.2.4.1 Oil solutions

Oil solutions were the first injectable depot formulations when they were used for the intramuscular (i.m.) injection of antipsychotic drugs as early as the 1950s.<sup>31</sup> Oil solutions were reported to extend the release from days to months, given their highly lipophilic nature and high viscosity. A variety of oil vehicles were used for the purpose of extending the release, such as sesame oil, castor oil, ethyl oleate, and many others. The requirements for a potential oil depot formulation are to have high stability, low irritability, and low viscosity.<sup>32</sup> Oils with high viscosity are difficult to handle and cause pain during the injection process. Usually, long-chain esters are conjugated to the loaded API (i.e. prodrugs) to increase the affinity to the oil and further prolong the release profile. For instance, fluphenazine, a first-generation antipsychotic, was conjugated to decanoic acid forming the fluphenazine decanoate prodrug, which extended its half-life from 7.7 h (in the case of parent fluphenazine) to 9.7 days.<sup>33</sup> The mechanism of extending the release is that the oil vehicle acts as a reservoir in the injection site, where the drug slowly partitions from the oil phase to the surrounding tissue fluid where it is hydrolyzed by plasma esterases. Then, active API can transfer to the systemic circulation via the dense blood vessels in the muscles.<sup>34,35</sup> The release rate is governed by the viscosity of the oil, the clearance of the oil vehicle, and the injection site place.<sup>32</sup> Also, the lipophilicity of the drug is a major controlling factor. Oils with lower viscosities can better spread in the injection site, and thus increase the surface area for the drug partitioning which leads to relatively accelerated release.<sup>28</sup> The advantages of oil depots include the simplicity of manufacturing, short preparation time, low cost, and high stability. However, oil depots are limited to lipophilic molecules given their high lipophilicity unless hydrophilic molecules are chemically modified.

#### 1.2.4.2 Liposomes

Liposomes are one of the versatile drug delivery families that has been widely used since the 1960s.<sup>36</sup> Liposomes are spherical vesicles that are composed of phospholipid bilayers surrounding one or more aqueous compartments. Drug compounds can be encapsulated in the aqueous compartments or the lipid bilayers.<sup>37</sup> The versatility of liposomes is due to their unique structure which allows them to encapsulate hydrophilic, lipophilic, or amphiphilic molecules. In addition, the natural sources of phospholipids comprising liposomes confer high biocompatibility and biodegradability. They were utilized for various reasons such as enhancing the solubility of lipophilic molecules, reducing drug toxicity, imparting targeting functionality, or sustaining the release.<sup>38</sup> Based on composition, liposomes can be classified into conventional liposomes and multivesicular liposomes (MVLs) which vary in structure, size, and consequently application (**Figure 4**). Conventional liposomes comprise the early-reported liposomes, which are unilamellar vesicles (ULVs) with a size range of 0.1 – 0.5  $\mu\text{m}$ , and multilamellar vesicles (MLVs) with a size range of 0.2 – 5.0  $\mu\text{m}$ . Apart from the size difference between ULVs and MLVs, the structure is also different; ULVs have a single aqueous compartment surrounded by a phospholipid bilayer, whereas MLVs are composed of multiple concentric phospholipid bilayers with aqueous compartments lying in between them. Both conventional liposomes failed to extend the release for longer durations (e.g. > 24 h), which is probably due to their small size making them liable to rapid clearance.<sup>39,40</sup>

On the other hand, MVLs or DepoFoam<sup>®</sup> technology, were first prepared in 1983 by Kim et al. using the double-emulsification method.<sup>41</sup> MVLs have a unique structure of nonconcentric aqueous compartments that are connected by a continuous bilayer network (**Figure 4c**). MVLs exhibit various desirable properties that are not present in conventional liposomes, which impart

them with a capability to sustain the release.<sup>39</sup> MVLs' structure is distinguished by the presence of triolein, a neutral triglyceride lipid, which is responsible for forming the nonconcentric inner lipid network. Thus, MVLs can load both hydrophilic molecules in the aqueous compartments,<sup>42–44</sup> and lipophilic molecules in the continuous bilayer network.<sup>45</sup> Also, MVLs are giant liposomes with a size range of 5.0 – 50  $\mu\text{m}$ , which helps evade the rapid clearance by macrophages and retain them at the injection site as a drug depot.<sup>40</sup> Thus, MVLs can prolong the release from a few days to weeks.<sup>46</sup> The mechanism of sustaining the release by MVLs is probably attributed to a combined action of drug diffusion through the outermost lipid bilayer, rearrangement of inner vesicles, and erosion. The U.S. FDA has approved several MVLs products as long-acting depots such as Exparel<sup>®</sup> (bupivacaine), and DepoCyt<sup>®</sup> (cytarabine).<sup>47,48</sup> These products encapsulate hydrophilic APIs, given the high ratio of the aqueous compartments of MVLs to such molecules compared to lipid network (95:5).<sup>49</sup> However, lipophilic molecules were also encapsulated as reported by Lue et al. (2018),<sup>45</sup> while in another paper, cyclodextrin technology was utilized to enhance the loading of the lipophilic fluocinolone.<sup>50</sup> Challenges to the MVLs products include intensive manufacturing process, use of organic solvents, and the need for aseptic conditions.<sup>51</sup>

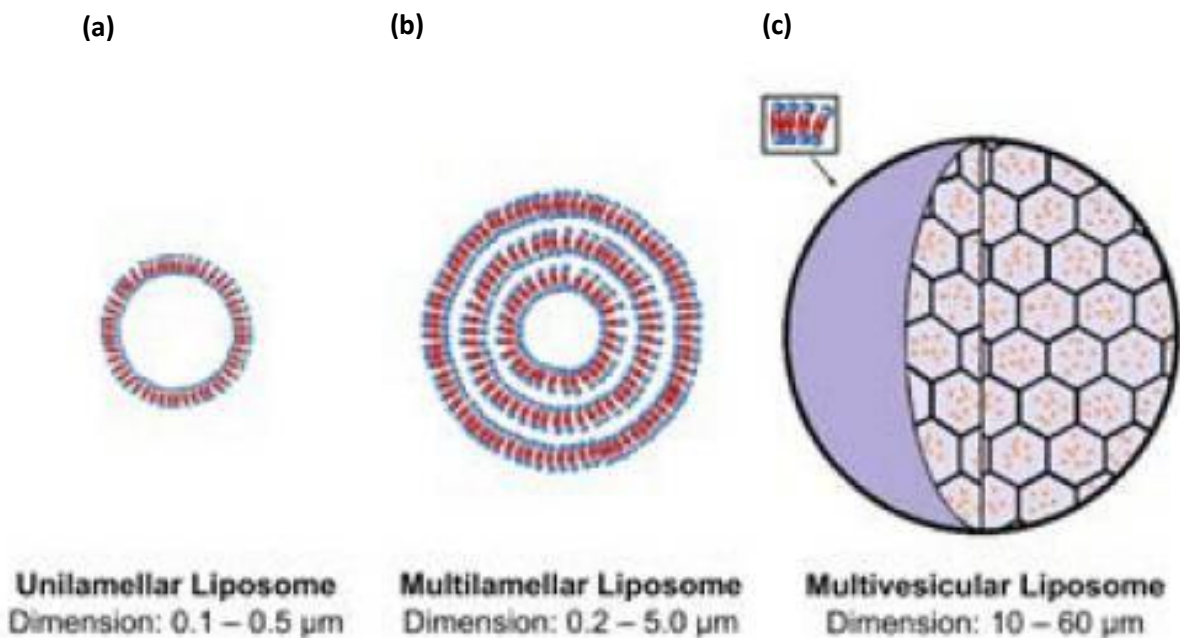


**Figure 4** Overview of the main type of liposomes: (a) unilamellar vesicles (ULVs), (b) multilamellar vesicles (MLVs), and (c) multivesicular liposomes (MVLs). (Used with permission from <sup>39</sup>).

#### 1.2.4.3 Suspended solids

Another strategy for sustaining the release is to suspend well-milled drug particles (within nanometers or a few micrometers) into water using appropriate excipients and stabilizers. Upon injection of these aqueous suspensions, drug molecules are slowly wetted and released into the tissue fluid.<sup>52,53</sup> The sustained release kinetics is governed by various factors such as the extent of drug solubility, particle size, injection site, and the available surface area within the injection site (i.e. spreading of the injection). The drug solubility is controlled by the chemical and crystal structure of the drug, while the surface area is controlled by the particles' size and surface topography.<sup>54</sup> Suspended solids are frequently used with highly lipophilic drugs or prodrugs ( $\log P > 3$ ) as a solution for formulating such difficult drug molecules. For instance, Invega Sustenna<sup>®</sup> is

a nanosuspension product for the extended release of the antipsychotic prodrug paliperidone palmitate, which had been FDA approved for once-a-month i.m. injection.<sup>55</sup> The physical stability of the suspension is very important for the administration process. For instance, if the suspension particles do not resuspend very well after sedimentation, then the whole formulation needs to be modified. Some excipients are reported to enhance suspensions' physical stability such as structured vehicles, flocculating agents, or a combination of both approaches. Structured vehicles are water-soluble polymers that increase the viscosity of the suspension, which reduces particles' sedimentation and facilitates the redispersion of the suspension upon administration.<sup>56</sup> While deflocculating agents can control the flocking of the drug particles such that they could be redispersed easily with agitation. Examples of deflocculating agents include surfactants, hydrophilic polymers, and electrolytes (**Table 1**).<sup>57</sup> It is also worth mentioning that excipients should be compatible with the drug particles and route of administration, to avoid any issues with the formulation's performance. The advantages of the suspended solids include improved API loading, improved bioavailability, and reduced side effects by limiting the amount of API reaching the systemic circulation. On the other hand, the stability of the suspension formulations remains the main challenge for this technology, which requires further research to find better stabilizers.<sup>58</sup>

Category	Examples
Surfactant	Docusate sodium
	Polysorbate 80
	Sodium lauryl sulfate
	Sorbitan monolaurate
Hydrophilic polymer	Carboxymethylcellulose sodium
	Methylcellulose
	Polyethylene glycol
	Tragacanth
Electrolyte	Xanthan gum
	Aluminum chloride
	Potassium dihydrogen phosphate
	Sodium chloride

**Table 1** Examples of deflocculating agents used in pharmaceutical suspensions. (Used with permission from <sup>57)</sup>)

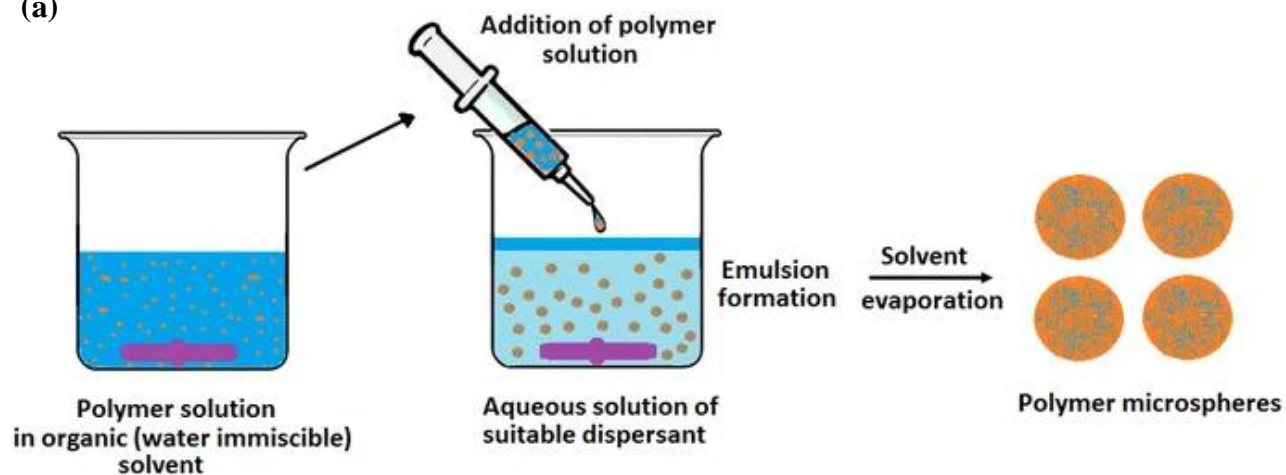


#### 1.2.4.4 Polymer microspheres

Another family of long-acting depots is polymer microspheres, where natural or synthetic biopolymers are used to encapsulate the drug molecules forming microscopic particles with a size range of about 1 – 1000  $\mu\text{m}$ .<sup>59</sup> Polymer microspheres can also encapsulate biotherapeutics such as peptides, proteins, and nucleic acids, where polymer chains surround them to form a protective shell to improve the biotherapeutics' stability.<sup>60</sup> Synthesis of polymer microspheres can be carried out by multiple methods such as solvent evaporation, ionic gelation, spray drying, and others. For example, the solvent evaporation method depends on emulsifying an organic solvent of dispersed polymer and dissolved/dispersed drug in a continuous aqueous phase (e.g. oil in water emulsion). Then, the organic solvent is evaporated at elevated temperature or under reduced pressure, which promotes the polymer particles to rearrange and limit the contact with the aqueous solution by forming precipitated microspheres (**Figure 5a**).<sup>61</sup> The characteristics of the microspheres (e.g. size, morphology, and release kinetics) are affected by variations in the synthesis techniques. For example, the emulsification power and the rate of solvent removal are the main factors that influence the microspheres' characteristics in the solvent evaporation method. When a slow rate of solvent removal is applied, the polymer chains tend to be more packed and smaller particles are observed. In contrast, when the organic solvent is quickly removed, the particle size is observed to be larger.<sup>25</sup> The drug release kinetics is also affected by such variations, besides the identity and characteristics of the used polymer (**Figure 5b**).<sup>62</sup> Generally, the release profile of drugs released from microspheres is multiphasic and involves various mechanisms such as drug diffusion, swelling of the microspheres due to the penetration of the release media, and microsphere erosion over time.<sup>63</sup> If the loaded drug is lipophilic, a burst release is initially observed, which may be attributed to adsorbed drug on the surface of the microsphere. Then, a lag phase is observed until

the release media penetrates the microspheres and allows the encapsulated drug to be slowly released. Afterward, a secondary sustained phase occurs, which may be attributed to the combined action of the drug diffusion and the polymer erosion.<sup>64</sup> The advantages of polymer microspheres include the control of the release kinetics by varying the characteristics of the microspheres (e.g. size, porosity). In addition, polymer microspheres confer biocompatibility and biodegradability which allow their wide use in drug delivery. Also, the spherical shape and small size facilitate the injection method. The limitations of polymer microspheres include low entrapment efficiency and low reproducibility of the particles' characteristics among different manufactured batches.<sup>65</sup>

(a)



(b)

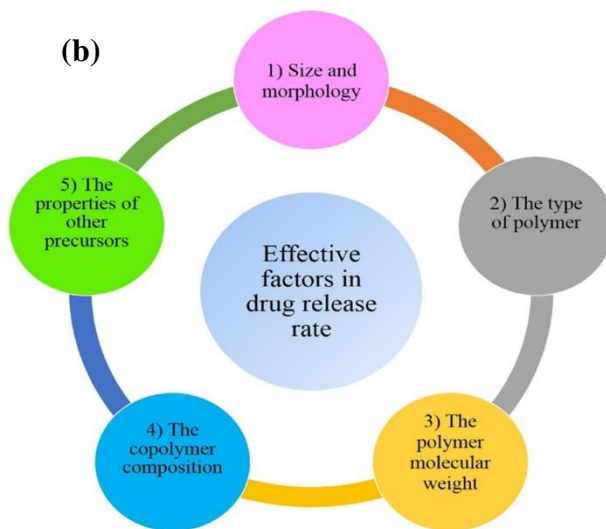


**Figure 5** (a) Graphic illustration of the solvent evaporation method used for preparing polymer microspheres (Used with permission from <sup>61</sup>), (b) factors that affect the release kinetics from polymer microspheres. (Used with permission from <sup>62</sup>)

#### 1.2.4.5 In-situ forming systems

In-situ forming (ISF) systems are another promising candidate for extending drug release. ISF systems depend in principle on gel formation upon contact with the tissue fluid after the injection. ISF systems are usually composed of API, solvent, and a polymer or lipid substance that is responsible for prolonging the API release.<sup>66</sup> An example of a common ISF polymeric system is Atrigel® technology where a combination of polymers such as poly-lactic-co-glycolic acid (PLGA) and Polylactic acid (PLA) are dissolved in an appropriate solvent such as *N*-methyl-2-pyrrolidone (NMP), and then mixed with API powder right before administration. Upon injection, an exchange of the NMP and tissue fluids occur which leads to the formation of a gel system that can prolong the API release for months (**Figure 6a**).<sup>67</sup> A similar idea is employed in phospholipid-based phase separation gels (PPSG) where the polymeric materials are replaced with natural phospholipids that can control the drug release. In PPSG, phospholipids are dissolved in EtOH, then API is added to that solution before administration. A sol-gel transformation occurs upon injection of the lipid-API solution (**Figure 6b**),<sup>68</sup> which results in a huge increase in the viscosity of the lipid system ( $10^1 - 10^6$  fold).<sup>69</sup> The formed gel can last for days or a few weeks, and so the sustained API release, as evident by fluorescence imaging.<sup>70</sup>

The release kinetics is influenced by the influx of tissue fluids, efflux of solvent, and polymer or lipid characteristics. The release profile is usually biphasic for a polymer ISF system, with an initial burst release that stems from the API diffusion during gel formation, followed by a secondary prolonged-release phase, which is the result of the combined action of polymer erosion and API diffusion.<sup>71</sup> While in PPSG, the burst release phase is much lower than in polymer ISF system, which may be ascribed to the high lipid content (70 %), which leads to a sharp viscosity increase upon injection and limits the initial API diffusion.<sup>69</sup> This could be beneficial if the API

therapeutic range is narrow, to prevent the occurrence of toxicity-related side effects. The advantages of ISF systems are numerous including easy handling, capacity to encapsulate small molecules and biotherapeutics, API protection, fewer side effects, biocompatibility and biodegradability of polymer or lipid, and simple manufacturing in comparison to polymer microspheres.<sup>66</sup> On the other hand, ISF systems have some limitations such as the difficult control of the ISF injection, which leads to variability in the *in vivo* release profiles. In addition, the use of organic solvents in ISF may cause some side effects. Another limitation for PPSG is that API must be soluble in one of a few suitable solvents, such as EtOH.<sup>16</sup> A summary of the long-acting depot formulations discussed in this section and their release mechanisms are shown in **Figure 7**.

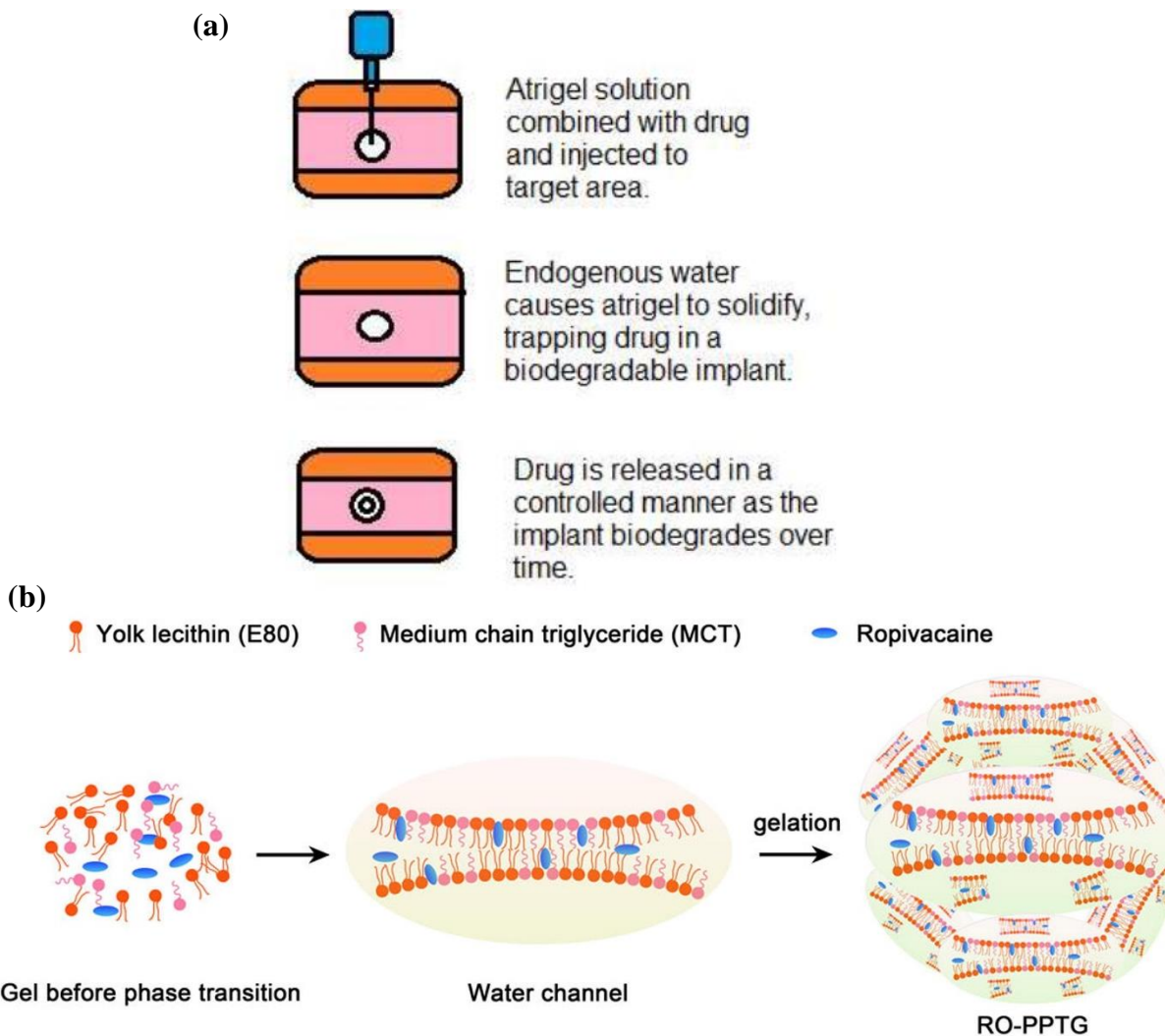


**Figure 6** (a) Graphic illustration of the Atrigel<sup>®</sup> technology used for sustaining the drug release using polymer ISF system (Used with permission from <sup>67</sup>), (b) graphic illustration of the sol-gel process observed with phospholipid-based phase separation gels (PPSG). (Used with permission from <sup>68</sup>).

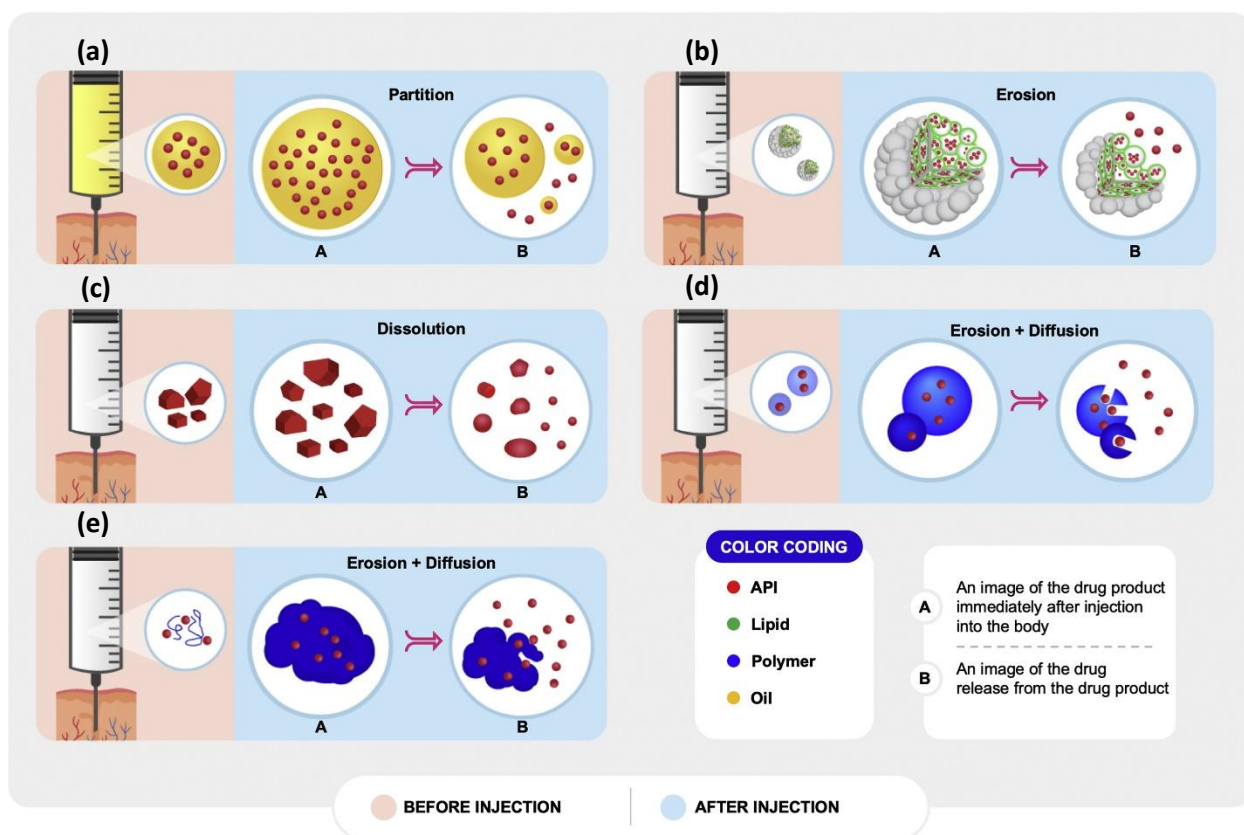


**Figure 7** A summary of the long-acting depot formulations and their release mechanisms after injection: (a) oil solutions, (b) multivesicular liposomes, (c) suspended solids, (d) polymer microspheres, and (e) in-situ forming systems. (Used with permission from <sup>25</sup>).

## 1.4 Long-acting depot formulations for cancer therapy

Cancer is a major disease worldwide and a huge burden to public health. According to the American Cancer Society 2022 report, cancer is the second leading cause of mortality in the United States. Around 1.9 million new cancer cases and 600,000 deaths are estimated this year in the United States due to cancer malignancy.<sup>72</sup> Cancer represents a huge challenge when it comes to the development of a therapeutic approach due to its various hallmarks such as avoiding immune destruction, inducing angiogenesis, the ability to metastasize, and others (**figure 8**).<sup>73</sup> The conventional treatment protocols such as chemotherapy, radiotherapy, and surgery, showed improvement in survival rates as compared to early times when these protocols were nascent.<sup>74</sup> However, they still exhibit serious drawbacks such as mild to severe adverse effects resulting from the nonspecific cytotoxicity against healthy tissues, low bioavailability, tumor recurrence, and development of multidrug resistance.<sup>75–77</sup> Therefore, there is a necessity for alternative approaches that can negate the aforementioned limitations and improve the therapeutic outcome. Among these approaches, cancer immunotherapy emerged as a promising solution, which had shown substantial insights into cancer treatment over the last decade to date. The mechanism of immunotherapeutic treatment relies on instructing the immune system to recognize and fight cancer cells, thus avoiding nonspecific toxicity and reducing the incidence of side effects.<sup>78,79</sup> In addition to immunotherapy, photodynamic therapy (PDT) also showed potential as another alternative cancer treatment. It is a non-invasive approach that relies on the administration of a photosensitizer to a tumor site, then it gets activated by a focused optical energy to destroy tumor cells through the formation of cytotoxic reactive oxygen species.<sup>80,81</sup> However, all these treatment options still encounter challenges with tumor targeting and the ability to penetrate solid tumors.



Long-acting depots can improve the efficacy of such treatments through their numerous advantages such as localizing the drug administration, prolonging the drug exposure, protecting the drug against degradation, conferring targeting functionality, and reducing side effects. Therefore, the utilization of long-acting depots for cancer therapy was investigated in this thesis. The second chapter discusses the development of long-acting multivesicular liposomes for the localized depot delivery of ingenol-3-angelate, a protein kinase C agonist. The third chapter discusses the development of long-acting formulations for two analogues of kifunensine, a type I mannosidase inhibitor. Both of the drugs used in these chapters are potential agents for cancer immunotherapy. While chapter four discusses a PDT approach for the treatment of head and neck squamous cell carcinoma. In that chapter, we relied on an alternative approach to long-acting depots, in which we developed hyaluronan nanoconjugates to enhance the specific tumor cells' uptake and retention of the photosensitizer, pyropheophorbide-a.

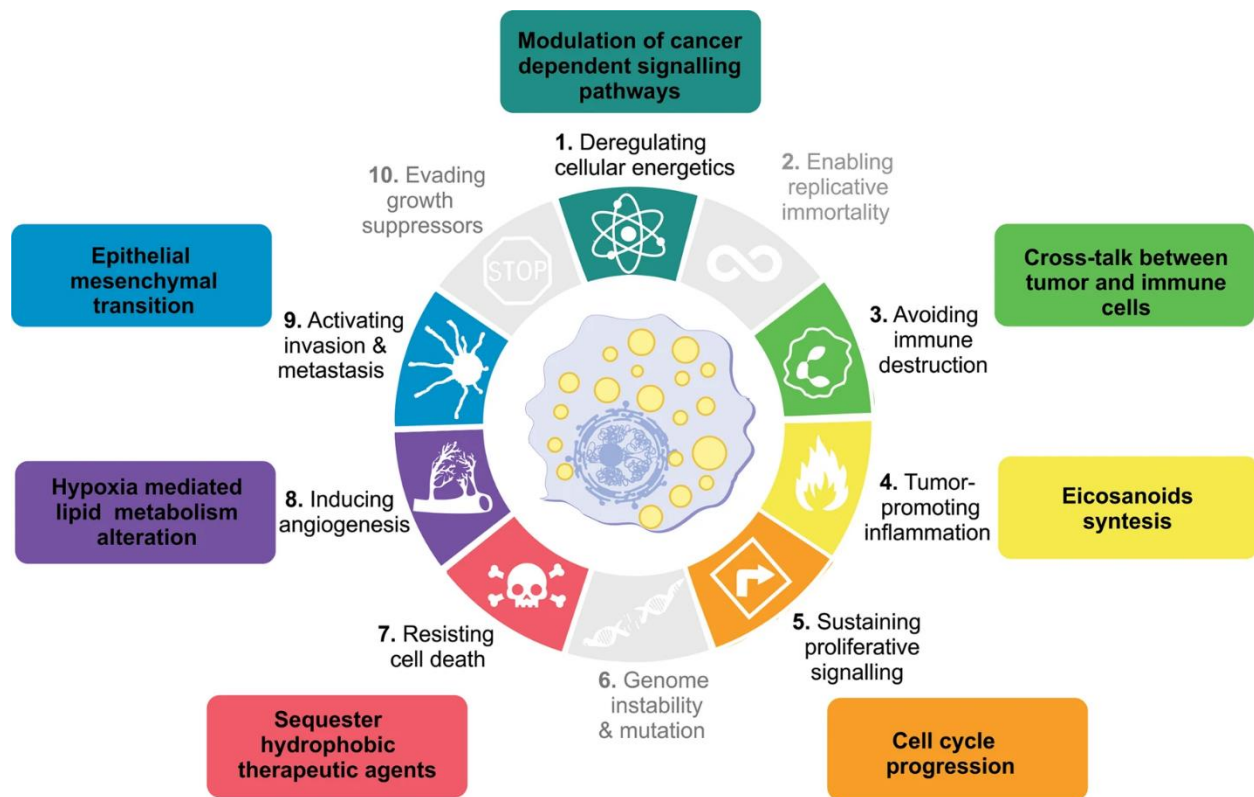


**Figure 8** A schematic illustration of the various cancer hallmarks. (Used with permission from <sup>73</sup>)

## **1.5 Conclusion**

The development of modified-release formulations is an active research area as a potential solution for the drawbacks of the immediate-release formulations, especially in the case of long-term treatment. To be able to improve the therapeutic outcome, the design of modified-release formulations should address the physicochemical properties of the loaded API and the biological barriers which they would encounter upon administration. A variety of long-acting depots have found their way into the pharmaceutical market including oil solutions, liposomes, suspended solids, polymer microspheres, and ISF systems. The utilization of long-acting depots in cancer therapy can lend the current therapeutic protocols with improved efficacy and safety. Further research in that area can lay the foundation for better cancer therapeutics in the future.

## 1.6 References

- (1) Singh, D.; Mittal Garg, N.; Kaur, G. Topical Drug Delivery Systems: A Patent Review. *Expert Opinion on Therapeutic Patents* **2015**, *26*.  
<https://doi.org/10.1517/13543776.2016.1131267>.
- (2) Tiwari, G.; Tiwari, R.; Sriwastawa, B.; Bhati, L.; Pandey, S.; Pandey, P.; Bannerjee, S. K. Drug Delivery Systems: An Updated Review. *Int J Pharm Investig* **2012**, *2* (1), 2–11.  
<https://doi.org/10.4103/2230-973X.96920>.
- (3) Wen, H.; Jung, H.; Li, X. Drug Delivery Approaches in Addressing Clinical Pharmacology-Related Issues: Opportunities and Challenges. *AAPS J* **2015**, *17* (6), 1327–1340.  
<https://doi.org/10.1208/s12248-015-9814-9>.
- (4) Kamaly, N.; Yameen, B.; Wu, J.; Farokhzad, O. C. Degradable Controlled-Release Polymers and Polymeric Nanoparticles: Mechanisms of Controlling Drug Release. *Chem Rev* **2016**, *116* (4), 2602–2663. <https://doi.org/10.1021/acs.chemrev.5b00346>.
- (5) Kohane, D. S.; Lipp, M.; Kinney, R. C.; Anthony, D. C.; Louis, D. N.; Lotan, N.; Langer, R. Biocompatibility of Lipid-Protein-Sugar Particles Containing Bupivacaine in the Epineurium. *J Biomed Mater Res* **2002**, *59* (3), 450–459. <https://doi.org/10.1002/jbm.1261>.
- (6) Park, K. Controlled Drug Delivery Systems: Past Forward and Future Back. *J Control Release* **2014**, *190*, 3–8. <https://doi.org/10.1016/j.jconrel.2014.03.054>.
- (7) Yun, Y. H.; Lee, B. K.; Park, K. Controlled Drug Delivery: Historical Perspective for the next Generation. *Journal of Controlled Release* **2015**, *219*, 2–7.  
<https://doi.org/10.1016/j.jconrel.2015.10.005>.

- (8) Burgess, D. J.; Wright, J. C. An Introduction to Long Acting Injections and Implants. In *Long Acting Injections and Implants*; Wright, J. C., Burgess, D. J., Eds.; Springer US: Boston, MA, 2012; pp 1–9. [https://doi.org/10.1007/978-1-4614-0554-2\\_1](https://doi.org/10.1007/978-1-4614-0554-2_1).
- (9) Neeraj, B.; Abhishek, K.; Abhilash, C.; Rubia, C.; Rajni, B. A REVIEW ON IMMEDIATE RELEASE DRUG DELIVERY SYSTEM. *I* **2014**, 4 (1), 78–87.
- (10) Nyol, S.; Gupta, M. M. IMMEDIATE DRUG RELEASE DOSAGE FORM: A REVIEW. *Journal of Drug Delivery and Therapeutics* **2013**, 3 (2). <https://doi.org/10.22270/jddt.v3i2.457>.
- (11) Abdelkader, H.; Fathalla, Z.; Seyfoddin, A.; Farahani, M.; Thrimawithana, T.; Allahham, A.; Alani, A. W. G.; Al-Kinani, A. A.; Alany, R. G. Polymeric Long-Acting Drug Delivery Systems (LADDs) for Treatment of Chronic Diseases: Inserts, Patches, Wafers, and Implants. *Advanced Drug Delivery Reviews* **2021**, 177, 113957. <https://doi.org/10.1016/j.addr.2021.113957>.
- (12) *Modified-Release Drug Delivery Technology*; Rathbone, M. J., Hadgraft, J., Roberts, M. S., Eds.; Drugs and the pharmaceutical sciences; Marcel Dekker: New York, 2003.
- (13) 1151 PHARMACEUTICAL DOSAGE FORMS. **2021**, 23.
- (14) Perrie, Y.; Rades, T. *FASTtrack Pharmaceuticals: Drug Delivery and Targeting*; Pharmaceutical Press, 2012.
- (15) Wheless, J. W.; Phelps, S. J. A Clinician’s Guide to Oral Extended-Release Drug Delivery Systems in Epilepsy. *J Pediatr Pharmacol Ther* **2018**, 23 (4), 277–292. <https://doi.org/10.5863/1551-6776-23.4.277>.
- (16) Rahnfeld, L.; Luciani, P. Injectable Lipid-Based Depot Formulations: Where Do We Stand? *Pharmaceutics* **2020**, 12 (6), E567. <https://doi.org/10.3390/pharmaceutics12060567>.

- (17) Blythe, R. H. Sympathomimetic Preparation. US2738303A, March 13, 1956.
- (18) Schwendeman, S. P.; Shah, R. B.; Bailey, B. A.; Schwendeman, A. S. Injectable Controlled Release Depots for Large Molecules. *Journal of Controlled Release* **2014**, *190*, 240–253. <https://doi.org/10.1016/j.jconrel.2014.05.057>.
- (19) Almeida, A. J.; Souto, E. Solid Lipid Nanoparticles as a Drug Delivery System for Peptides and Proteins. *Advanced Drug Delivery Reviews* **2007**, *59* (6), 478–490. <https://doi.org/10.1016/j.addr.2007.04.007>.
- (20) Acharya, S.; Sahoo, S. K. PLGA Nanoparticles Containing Various Anticancer Agents and Tumour Delivery by EPR Effect. *Advanced Drug Delivery Reviews* **2011**, *63* (3), 170–183. <https://doi.org/10.1016/j.addr.2010.10.008>.
- (21) Almeida, H.; Amaral, M. H.; Lobão, P. Temperature and PH Stimuli-Responsive Polymers and Their Applications in Controlled and Self-Regulated Drug Delivery. *Journal of Applied Pharmaceutical Science* **10**.
- (22) Heinemann, L. The Failure of Exubera: Are We Beating a Dead Horse? *J Diabetes Sci Technol* **2008**, *2* (3), 518–529.
- (23) Saifullah, B.; Hussein, M. Z. B.; Al Ali, S. H. H. Controlled-Release Approaches towards the Chemotherapy of Tuberculosis. *Int J Nanomedicine* **2012**, *7*, 5451–5463. <https://doi.org/10.2147/IJN.S34996>.
- (24) Hu, J.; Wang, M.; Xiao, X.; Zhang, B.; Xie, Q.; Xu, X.; Li, S.; Zheng, Z.; Wei, D.; Zhang, X. A Novel Long-Acting Azathioprine Polyhydroxyalkanoate Nanoparticle Enhances Treatment Efficacy for Systemic Lupus Erythematosus with Reduced Side Effects. *Nanoscale* **2020**, *12* (19), 10799–10808. <https://doi.org/10.1039/D0NR01308K>.

- (25) O'Brien, M. N.; Jiang, W.; Wang, Y.; Loffredo, D. M. Challenges and Opportunities in the Development of Complex Generic Long-Acting Injectable Drug Products. *Journal of Controlled Release* **2021**, *336*, 144–158. <https://doi.org/10.1016/j.jconrel.2021.06.017>.
- (26) Kamat, S. A.; Offord, S.; Docherty, J.; Lin, J.; Eramo, A.; Baker, R. A.; Gutierrez, B.; Karson, C. Reduction in Inpatient Resource Utilization and Costs Associated with Long-Acting Injectable Antipsychotics across Different Age Groups of Medicaid-Insured Schizophrenia Patients. *Drugs Context* **2015**, *4*, 212267. <https://doi.org/10.7573/dic.212267>.
- (27) Ho, M. J.; Kim, S. R.; Choi, Y. W.; Kang, M. J. Recent Advances in Intra-Articular Drug Delivery Systems to Extend Drug Retention in Joint. *J. Pharm. Investig.* **2019**, *49* (1), 9–15. <https://doi.org/10.1007/s40005-018-0383-7>.
- (28) Larsen, S. W.; Østergaard, J.; Friberg-Johansen, H.; Jessen, M. N. B.; Larsen, C. In Vitro Assessment of Drug Release Rates from Oil Depot Formulations Intended for Intra-Articular Administration. *European Journal of Pharmaceutical Sciences* **2006**, *29* (5), 348–354. <https://doi.org/10.1016/j.ejps.2006.07.002>.
- (29) Polyester-Based Micelles and Nanoparticles for the Parenteral Delivery of Taxanes. *Journal of Controlled Release* **2010**, *143* (1), 2–12. <https://doi.org/10.1016/j.jconrel.2009.11.012>.
- (30) Sumarsono, A.; Sumarsono, N.; Das, S. R.; Vaduganathan, M.; Agrawal, D.; Pandey, A. Economic Burden Associated With Extended-Release vs Immediate-Release Drug Formulations Among Medicare Part D and Medicaid Beneficiaries. *JAMA Netw Open* **2020**, *3* (2), e200181. <https://doi.org/10.1001/jamanetworkopen.2020.0181>.

- (31) Carlo Altamura, A.; Sassella, F.; Santini, A.; Montresor, C.; Fumagalli, S.; Mundo, E. Intramuscular Preparations of Antipsychotics. *Drugs* **2003**, *63* (5), 493–512. <https://doi.org/10.2165/00003495-200363050-00004>.
- (32) Larsen, S. W.; Thing, M. A.; Larsen, C. Oily (Lipophilic) Solutions and Suspensions. In *Long Acting Injections and Implants*; Wright, J. C., Burgess, D. J., Eds.; Springer US: Boston, MA, 2012; pp 113–135. [https://doi.org/10.1007/978-1-4614-0554-2\\_7](https://doi.org/10.1007/978-1-4614-0554-2_7).
- (33) Luo, J. P.; Hubbard, J. W.; Midha, K. K. Studies on the Mechanism of Absorption of Depot Neuroleptics: Fluphenazine Decanoate in Sesame Oil. *Pharm Res* **1997**, *14* (8), 1079–1084. <https://doi.org/10.1023/a:1012165731390>.
- (34) Larsen, S. W.; Rinvar, E.; Svendsen, O.; Lykkesfeldt, J.; Friis, G. J.; Larsen, C. Determination of the Disappearance Rate of Iodine-125 Labelled Oils from the Injection Site after Intramuscular and Subcutaneous Administration to Pigs. *International Journal of Pharmaceutics* **2001**, *230* (1), 67–75. [https://doi.org/10.1016/S0378-5173\(01\)00860-2](https://doi.org/10.1016/S0378-5173(01)00860-2).
- (35) Larsen, S. W.; Frost, A. B.; Østergaard, J.; Marcher, H.; Larsen, C. On the Mechanism of Drug Release from Oil Suspensions in Vitro Using Local Anesthetics as Model Drug Compounds. *European Journal of Pharmaceutical Sciences* **2008**, *34* (1), 37–44. <https://doi.org/10.1016/j.ejps.2008.02.005>.
- (36) Bangham, A. D.; Standish, M. M.; Watkins, J. C. Diffusion of Univalent Ions across the Lamellae of Swollen Phospholipids. *Journal of Molecular Biology* **1965**, *13* (1), 238–IN27. [https://doi.org/10.1016/S0022-2836\(65\)80093-6](https://doi.org/10.1016/S0022-2836(65)80093-6).
- (37) Malam, Y.; Loizidou, M.; Seifalian, A. M. Liposomes and Nanoparticles: Nanosized Vehicles for Drug Delivery in Cancer. *Trends Pharmacol Sci* **2009**, *30* (11), 592–599. <https://doi.org/10.1016/j.tips.2009.08.004>.



- (38) Bulbake, U.; Doppalapudi, S.; Kommineni, N.; Khan, W. Liposomal Formulations in Clinical Use: An Updated Review. *Pharmaceutics* **2017**, *9* (2), 12. <https://doi.org/10.3390/pharmaceutics9020012>.
- (39) Salehi, B.; Mishra, A. P.; Nigam, M.; Kobarfard, F.; Javed, Z.; Rajabi, S.; Khan, K.; Ashfaq, H. A.; Ahmad, T.; Pezzani, R.; Ramírez-Alarcón, K.; Martorell, M.; Cho, W. C.; Ayatollahi, S. A.; Sharifi-Rad, J. Multivesicular Liposome (Depofoam) in Human Diseases. *Iranian Journal of Pharmaceutical Research: IJPR* **2020**, *19* (2), 9. <https://doi.org/10.22037/ijpr.2020.112291.13663>.
- (40) Katre, N. V. Liposome-Based Depot Injection Technologies. *Am J Drug Deliv* **2004**, *2* (4), 213–227. <https://doi.org/10.2165/00137696-200402040-00002>.
- (41) Kim, S.; Turker, M. S.; Chi, E. Y.; Sela, S.; Martin, G. M. Preparation of Multivesicular Liposomes. *Biochimica et Biophysica Acta (BBA) - Biomembranes* **1983**, *728* (3), 339–348. [https://doi.org/10.1016/0005-2736\(83\)90504-7](https://doi.org/10.1016/0005-2736(83)90504-7).
- (42) Zhang, L.; Ding, L.; Tang, C.; Li, Y.; Yang, L. Liraglutide-Loaded Multivesicular Liposome as a Sustained-Delivery Reduces Blood Glucose in SD Rats with Diabetes. *Drug Deliv* **2016**, *23* (9), 3358–3363. <https://doi.org/10.1080/10717544.2016.1180723>.
- (43) Wang, T.; Gao, L.; Quan, D. Multivesicular Liposome (MVL) Sustained Delivery of a Novel Synthetic Cationic GnRH Antagonist for Prostate Cancer Treatment. *J Pharm Pharmacol* **2011**, *63* (7), 904–910. <https://doi.org/10.1111/j.2042-7158.2011.01295.x>.
- (44) Qiu, J.; Wei, X.; Geng, F.; Liu, R.; Zhang, J.; Xu, Y. Multivesicular Liposome Formulations for the Sustained Delivery of Interferon  $\alpha$ -2b. *Acta Pharmacologica Sinica* **2005**, *26* (11), 1395–1401. <https://doi.org/10.1111/j.1745-7254.2005.00188.x>.

- (45) Luo, Y.; Liu, Z.; Zhang, X.; Huang, J.; Yu, X.; Li, J.; Xiong, D.; Sun, X.; Zhong, Z. Effect of a Controlled-Release Drug Delivery System Made of Oleanolic Acid Formulated into Multivesicular Liposomes on Hepatocellular Carcinoma in Vitro and in Vivo. *Int J Nanomedicine* **2016**, *11*, 3111–3129. <https://doi.org/10.2147/IJN.S108445>.
- (46) Zhang, L.; Zhang, Q.; Wang, X.; Zhang, W.; Lin, C.; Chen, F.; Yang, X.; Pan, W. Drug-in-Cyclodextrin-in-Liposomes: A Novel Drug Delivery System for Flurbiprofen. *International Journal of Pharmaceutics* **2015**, *492* (1), 40–45. <https://doi.org/10.1016/j.ijpharm.2015.07.011>.
- (47) Commissioner, O. of the. FDA In Brief: FDA Approves New Use of Exparel for Nerve Block Pain Relief Following Shoulder Surgeries. *FDA* **2019**.
- (48) Drug Approval Package: DepoCyt (Cytarabine Liposomal) NDA# 21-041 [https://www.accessdata.fda.gov/drugsatfda\\_docs/nda/99/21-041\\_DepoCyt.cfm](https://www.accessdata.fda.gov/drugsatfda_docs/nda/99/21-041_DepoCyt.cfm) (accessed 2022 -04 -05).
- (49) Ye, Q.; Asherman, J.; Stevenson, M.; Brownson, E.; Katre, N. V. DepoFoam™ Technology: A Vehicle for Controlled Delivery of Protein and Peptide Drugs. *Journal of Controlled Release* **2000**, *64* (1), 155–166. [https://doi.org/10.1016/S0168-3659\(99\)00146-7](https://doi.org/10.1016/S0168-3659(99)00146-7).
- (50) Vafaei, S. Y.; Dinarvand, R.; Esmaeili, M.; Mahjub, R.; Toliyat, T. Controlled-Release Drug Delivery System Based on Fluocinolone Acetonide-Cyclodextrin Inclusion Complex Incorporated in Multivesicular Liposomes. *Pharm Dev Technol* **2015**, *20* (7), 775–781. <https://doi.org/10.3109/10837450.2014.920358>.
- (51) Mantripragada, S. A Lipid Based Depot (DepoFoam Technology) for Sustained Release Drug Delivery. *Prog Lipid Res* **2002**, *41* (5), 392–406. [https://doi.org/10.1016/s0163-7827\(02\)00004-8](https://doi.org/10.1016/s0163-7827(02)00004-8).

- (52) Merisko-Liversidge, E.; Liversidge, G. G. Nanosizing for Oral and Parenteral Drug Delivery: A Perspective on Formulating Poorly-Water Soluble Compounds Using Wet Media Milling Technology. *Adv Drug Deliv Rev* **2011**, *63* (6), 427–440. <https://doi.org/10.1016/j.addr.2010.12.007>.
- (53) Verma, S.; Burgess, D. Solid Nanosuspensions: The Emerging Technology and Pharmaceutical Applications as Nanomedicine. In *Pharmaceutical Suspensions: From Formulation Development to Manufacturing*; Kulshreshtha, A. K., Singh, O. N., Wall, G. M., Eds.; Springer: New York, NY, 2010; pp 285–318. [https://doi.org/10.1007/978-1-4419-1087-5\\_10](https://doi.org/10.1007/978-1-4419-1087-5_10).
- (54) Hirano, K.; Yamada, H. Studies on the Absorption of Practically Water-Insoluble Drugs Following Injection. IV. An Approach for Predicting Relative Intramuscular Absorption Rates of a Drug in Oily Solution, Aqueous Suspension and Aqueous Surfactant Solution in Rats. *Chem Pharm Bull (Tokyo)* **1981**, *29* (5), 1410–1415. <https://doi.org/10.1248/cpb.29.1410>.
- (55) Samtani, M. N.; Vermeulen, A.; Stuyckens, K. Population Pharmacokinetics of Intramuscular Paliperidone Palmitate in Patients with Schizophrenia: A Novel Once-Monthly, Long-Acting Formulation of an Atypical Antipsychotic. *Clin Pharmacokinet* **2009**, *48* (9), 585–600. <https://doi.org/10.2165/11316870-0000000000-000000>.
- (56) Kola-Mustapha, A. T.; Ghazali, Y. O.; Ayotunde, H. T.; Atunwa, S. A.; Usman, S. O. Evaluation of the Antidiarrheal Activity of the Leaf Extract of *Parquetina Nigrescens* and Formulation into Oral Suspensions. *J Exp Pharmacol* **2019**, *11*, 65–72. <https://doi.org/10.2147/JEP.S214417>.

- (57) Brunaugh, A. D.; Smyth, H. D. C.; Williams III, R. O. Disperse Systems: Suspensions. In *Essential Pharmaceutics*; Brunaugh, A. D., Smyth, H. D. C., Williams III, R. O., Eds.; Springer International Publishing: Cham, 2019; pp 91–110. [https://doi.org/10.1007/978-3-030-31745-4\\_6](https://doi.org/10.1007/978-3-030-31745-4_6).
- (58) Wang, Y.; Zheng, Y.; Zhang, L.; Wang, Q.; Zhang, D. Stability of Nanosuspensions in Drug Delivery. *J Control Release* **2013**, *172* (3), 1126–1141. <https://doi.org/10.1016/j.jconrel.2013.08.006>.
- (59) Saralidze, K.; Koole, L. H.; Knetsch, M. L. W. Polymeric Microspheres for Medical Applications. *Materials* **2010**, *3* (6), 3537–3564. <https://doi.org/10.3390/ma3063537>.
- (60) Berkland, C.; Kipper, M. J.; Narasimhan, B.; Kim, K. (Kevin); Pack, D. W. Microsphere Size, Precipitation Kinetics and Drug Distribution Control Drug Release from Biodegradable Polyanhydride Microspheres. *Journal of Controlled Release* **2004**, *94* (1), 129–141. <https://doi.org/10.1016/j.jconrel.2003.09.011>.
- (61) Hossain, K. M. Z.; Patel, U.; Ahmed, I. Development of Microspheres for Biomedical Applications: A Review. *Prog Biomater* **2015**, *4* (1), 1–19. <https://doi.org/10.1007/s40204-014-0033-8>.
- (62) Alavi, M.; Webster, T. J. Recent Progress and Challenges for Polymeric Microsphere Compared to Nanosphere Drug Release Systems: Is There a Real Difference? *Bioorganic & Medicinal Chemistry* **2021**, *33*, 116028. <https://doi.org/10.1016/j.bmc.2021.116028>.
- (63) Freiberg, S.; Zhu, X. X. Polymer Microspheres for Controlled Drug Release. *International Journal of Pharmaceutics* **2004**, *282* (1), 1–18. <https://doi.org/10.1016/j.ijpharm.2004.04.013>.

- (64) Birnbaum, D. T.; Kosmala, J. D.; Henthorn, D. B.; Brannon-Peppas, L. Controlled Release of  $\beta$ -Estradiol from PLGA Microparticles:: The Effect of Organic Phase Solvent on Encapsulation and Release. *Journal of Controlled Release* **2000**, *65* (3), 375–387. [https://doi.org/10.1016/S0168-3659\(99\)00219-9](https://doi.org/10.1016/S0168-3659(99)00219-9).
- (65) Subedi, G.; Shrestha, A. K.; Shakya, S. Study of Effect of Different Factors in Formulation of Micro and Nanospheres with Solvent Evaporation Technique. *Open Pharmaceutical Sciences Journal* **2016**, *3* (1). <https://doi.org/10.2174/1874844901603010182>.
- (66) Benhabbour, S. R.; Kovarova, M.; Jones, C.; Copeland, D. J.; Shrivastava, R.; Swanson, M. D.; Sykes, C.; Ho, P. T.; Cottrell, M. L.; Sridharan, A.; Fix, S. M.; Thayer, O.; Long, J. M.; Hazuda, D. J.; Dayton, P. A.; Mumper, R. J.; Kashuba, A. D. M.; Victor Garcia, J. Ultra-Long-Acting Tunable Biodegradable and Removable Controlled Release Implants for Drug Delivery. *Nat Commun* **2019**, *10* (1), 4324. <https://doi.org/10.1038/s41467-019-12141-5>.
- (67) Malik, K.; Singh, I.; Nagpal, M.; Arora, S. Atrigel: A Potential Parenteral Controlled Drug Delivery System. *Der Pharmacia Sinica* **2010**, *1*.
- (68) Li, H.; Liu, T.; Zhu, Y.; Fu, Q.; Wu, W.; Deng, J.; Lan, L.; Shi, S. An in Situ-Forming Phospholipid-Based Phase Transition Gel Prolongs the Duration of Local Anesthesia for Ropivacaine with Minimal Toxicity. *Acta Biomaterialia* **2017**, *58*, 136–145. <https://doi.org/10.1016/j.actbio.2017.06.013>.
- (69) Zhang, T.; Peng, Q.; San, F.-Y.; Luo, J.-W.; Wang, M.-X.; Wu, W.-Q.; Gong, T.; Zhang, Z.-R. A High-Efficiency, Low-Toxicity, Phospholipids-Based Phase Separation Gel for Long-Term Delivery of Peptides. *Biomaterials* **2015**, *45*, 1–9. <https://doi.org/10.1016/j.biomaterials.2014.12.042>.

- (70) Xiang, N.; Zhou, X.; He, X.; Zhang, Y.; Zhang, J.; Zhang, Z.-R.; Sun, X.; Gong, T.; Fu, Y. An Injectable Gel Platform for the Prolonged Therapeutic Effect of Pitavastatin in the Management of Hyperlipidemia. *J Pharm Sci* **2016**, *105* (3), 1148–1155. <https://doi.org/10.1016/j.xphs.2015.12.002>.
- (71) Ibrahim, T. M.; El-Megrab, N. A.; El-Nahas, H. M. Optimization of Injectable PLGA In-Situ Forming Implants of Anti-Psychotic Risperidone via Box-Behnken Design. *Journal of Drug Delivery Science and Technology* **2020**, *58*, 101803. <https://doi.org/10.1016/j.jddst.2020.101803>.
- (72) Siegel, R. L.; Miller, K. D.; Fuchs, H. E.; Jemal, A. Cancer Statistics, 2022. *CA: A Cancer Journal for Clinicians* **2022**, *72* (1), 7–33. <https://doi.org/10.3322/caac.21708>.
- (73) Cruz, A. L. S.; Barreto, E. de A.; Fazolini, N. P. B.; Viola, J. P. B.; Bozza, P. T. Lipid Droplets: Platforms with Multiple Functions in Cancer Hallmarks. *Cell Death Dis* **2020**, *11* (2), 1–16. <https://doi.org/10.1038/s41419-020-2297-3>.
- (74) Rossi, L.; Stevens, D.; Pierga, J.-Y.; Lerebours, F.; Rey, F.; Robain, M.; Asselain, B.; Rouzier, R. Impact of Adjuvant Chemotherapy on Breast Cancer Survival: A Real-World Population. *PLoS One* **2015**, *10* (7), e0132853. <https://doi.org/10.1371/journal.pone.0132853>.
- (75) Bukowski, K.; Kciuk, M.; Kontek, R. Mechanisms of Multidrug Resistance in Cancer Chemotherapy. *International Journal of Molecular Sciences* **2020**, *21* (9), 3233. <https://doi.org/10.3390/ijms21093233>.
- (76) Kottke, T.; Boisgerault, N.; Diaz, R. M.; Donnelly, O.; Rommelfanger-Konkol, D.; Pulido, J.; Thompson, J.; Mukhopadhyay, D.; Kaspar, R.; Coffey, M.; Pandha, H.; Melcher, A.; Harrington, K.; Selby, P.; Vile, R. Detecting and Targeting Tumor Relapse by Its Resistance

- to Innate Effectors at Early Recurrence. *Nat Med* **2013**, *19* (12), 1625–1631.  
<https://doi.org/10.1038/nm.3397>.
- (77) Qi, Y.; Min, H.; Mujeeb, A.; Zhang, Y.; Han, X.; Zhao, X.; Anderson, G. J.; Zhao, Y.; Nie, G. Injectable Hexapeptide Hydrogel for Localized Chemotherapy Prevents Breast Cancer Recurrence. *ACS Appl. Mater. Interfaces* **2018**, *10* (8), 6972–6981.  
<https://doi.org/10.1021/acsami.7b19258>.
- (78) Amos, S. M.; Duong, C. P. M.; Westwood, J. A.; Ritchie, D. S.; Junghans, R. P.; Darcy, P. K.; Kershaw, M. H. Autoimmunity Associated with Immunotherapy of Cancer. *Blood* **2011**, *118* (3), 499–509. <https://doi.org/10.1182/blood-2011-01-325266>.
- (79) Abdelbaky, S. B.; Ibrahim, M. T.; Samy, H.; Mohamed, M.; Mohamed, H.; Mustafa, M.; Abdelaziz, M. M.; Forrest, M. L.; Khalil, I. A. Cancer Immunotherapy from Biology to Nanomedicine. *Journal of Controlled Release* **2021**, *336*, 410–432.  
<https://doi.org/10.1016/j.jconrel.2021.06.025>.
- (80) Li, X.; Lee, S.; Yoon, J. Supramolecular Photosensitizers Rejuvenate Photodynamic Therapy. *Chem. Soc. Rev.* **2018**, *47* (4), 1174–1188. <https://doi.org/10.1039/C7CS00594F>.
- (81) Chen, J.; Fan, T.; Xie, Z.; Zeng, Q.; Xue, P.; Zheng, T.; Chen, Y.; Luo, X.; Zhang, H. Advances in Nanomaterials for Photodynamic Therapy Applications: Status and Challenges. *Biomaterials* **2020**, *237*, 119827.  
<https://doi.org/10.1016/j.biomaterials.2020.119827>.

**Chapter II: Development of long-acting multivesicular liposomes for the  
localized depot delivery of Ingenol-3-Angelate**



## 2.1 Introduction

Ingenol-3-Angelate (I3A) is a small molecule that chemically connects an ingenol moiety with angelic acid via an ester bond. I3A is a highly hydrophobic compound with poor aqueous solubility and high plasma protein binding (**Table 1**).<sup>1</sup> It is naturally isolated from the sap of the *Euphorbia peplus* plant<sup>2</sup>, but also reported to be semi-synthesized from the ingenol.<sup>3</sup> A gel form of I3A (Picato<sup>®</sup>) is FDA-approved as a topical treatment for Actinic Keratosis, a skin condition that results from cumulative exposure to ultraviolet sun radiation, which may develop into squamous cell carcinoma if left untreated.<sup>4-6</sup> The mechanism of I3A cytotoxicity is not fully elucidated, but based on *in vitro* and *in vivo* studies, there is evidence that correlates the exposure of I3A to imbalance in the intracellular calcium ions regulation which leads to plasma membrane disruption and mitochondria swelling.<sup>7,8</sup> Accordingly, I3A was developed clinically as a chemotherapeutic agent for skin cancers such as squamous cell carcinoma, basal cell carcinoma and melanoma.<sup>9-11</sup>

In addition to directly killing tumor cells, I3A was shown to initiate local inflammation and recruit immune cells.<sup>12,13</sup> For instance, I3A demonstrated good binding to protein kinase C-delta (PKC- $\delta$ ) which trigger an inflammatory response through the upregulation of proinflammatory cytokines such as interleukin-8 (IL-8) and tumor necrosis factor-alpha (TNF- $\alpha$ ).<sup>14,15</sup> I3A was also associated with recruiting CD8 T cells and increasing the expression of CD80 and CD86 on dendritic cells which leads to the activation of antitumor immune response.<sup>12</sup> Recently, I3A was shown to increase the expression of Interleukin-13-Receptor Alpha 2 (IL13R $\alpha$ 2).<sup>16</sup> The downregulation of IL13R $\alpha$ 2 was connected with developing resistance and reducing the efficiency of anti-IL13R $\alpha$ 2 based treatments. It is also used as a target for Chimeric Antigen Receptor-T cell (CAR-T) therapy against glioma.<sup>16,17</sup> Accordingly, the upregulation of IL13R $\alpha$ 2 through I3A

administration and the regulating immunostimulatory effects, are hypothesized to improve the eradication of glioma. The application of I3A to glioma requires intracranial injections to enable the drug to reach the tumor site. However, this administration is limited by the drug's hydrophobicity, wide tissue distribution, off-site toxicity, and rapid clearance.

To resolve these limitations, there is a need for a long-acting formulation that can localize the I3A delivery into gliomas and avoid frequent invasive injections. A potential formulation to satisfy such requirements is Multivesicular Liposomes (MVLs), which comprise nonconcentric aqueous compartments that are connected by lipid bilayers. This unique structure had been used to sustain the release of both lipophilic compounds through inner lipid network<sup>18</sup>, and hydrophilic compounds through aqueous compartments.<sup>19,20</sup> MVLs exhibit a relatively large size (5-50  $\mu\text{m}$ ), which is demanded to evade the rapid clearance by macrophages. The presence of an inner lipid network imparts the formulation with long-term stability and allows for the loading of lipophilic drugs.<sup>18</sup> However, in case of lipophilic drugs, limited amounts of drug can be encapsulated to MVLs due to the low ratio of the lipid bilayers (5%) to the aqueous compartments (95%).<sup>21</sup> Also, lipophilic drugs can hinder the lipid bilayer formation and affect its stability.<sup>22</sup> Therefore, we investigated Captisol® (Sulfobutylether- $\beta$ -Cyclodextrin) (SBE- $\beta$ -CD) as an agent to improve the loading of I3A by increasing the partitioning of the drug into the MVLs' aqueous compartments and preventing the detrimental effects on the lipid bilayer stability.

In this chapter, the preparation and characterization of MVLs for the loading of I3A is described. The sustained release of I3A was investigated *in vitro* and through an *in vivo* pharmacokinetic study. The development of MVLs-loaded I3A (MVLs-SBE- $\beta$ -CD-I3A) could pave the way for the I3A administration into glioma to examine the upregulation of IL13R $\alpha$ 2 and its potential use for CAR-T therapy.

Physicochemical properties of I3A	
Molecular weight	430.5 g/mol
Physical description	Crystalline solid powder
Formal charge	0
Computed Log P	3.12
Protein binding	> 99%
Topical bioavailability	0.21%
Water solubility	Limited ( <i>ca.</i> 4.3 ng/ml)

**Table 1** Physicochemical properties of I3A.<sup>1</sup>

## 2.2 Materials and Methods

### 2.2.1 Materials

The lipids 1,2-dipalmitoyl-sn-glycero-3-phospho-(1'-rac-glycerol) (sodium salt) (DPPG) and 1,2-dioleoyl-sn-glycero-3-phosphocholine (DOPC) were purchased from Avanti<sup>®</sup> polar lipids (Birmingham, AL). Glyceryl trioleate, cholesterol, L-lysine monohydrochloride and chloroform (ACS grade) were purchased from Sigma Aldrich (St. Louis, MO). Ingenol-3-angelate (I3A) was purchased from MedKoo Biosciences (Morrisville, NC). D-Glucose, sucrose, sodium dodecyl sulfate and HPLC grade solvents were purchased from Fisher Scientific (Hampton, NH). Doxorubicin hydrochloride salt and tacrolimus were obtained from LC labs (Woburn, MA). Float-A-Lyzer<sup>®</sup>G2 dialysis devices (MWCO: 3.5-5 kDa) were obtained from Repligen (Boston, MA).

### 2.2.2 Preparation of MVLS

The MVLS were prepared using a modified double-emulsion method.<sup>23,24</sup> Briefly, the oil phase (O) was composed of 1 ml of chloroform, in which an optimized ratio of the following lipids was dissolved: DOPC, Cholesterol, DPPG and triolein, with the molar ratio 7:11:1:1, respectively. Also, I3A was *in situ* loaded into MVLS by dissolving it into the O phase (0.7 mg/ml) due to its hydrophobicity. In a separate vial, the first water phase (W<sub>1</sub>) was prepared by dissolving 50 mg of sucrose in 1 ml of double distilled water (dd.H<sub>2</sub>O). While the second water phase (W<sub>2</sub>) was composed of 8 ml of dd.H<sub>2</sub>O with 23.5 mg L-lysine monohydrochloride and 320 mg D-Glucose dissolved within. The O and W<sub>1</sub> were emulsified together using a homogenizer (~ 10,000 rpm) for 10 min while cooling in an ice bath to prevent the build-up of heat in the emulsion. Then, 4 ml of W<sub>2</sub> phase was added to the W<sub>1</sub>/O emulsion with the use of a slow homogenizer speed (~ 1000 rpm) for 20 sec. The milky emulsion was then diluted with the remaining 4 ml of W<sub>2</sub> phase resulting in the final W<sub>1</sub>/O/W<sub>2</sub> system. Afterwards, a slow nitrogen gas flush was used to remove the chloroform, until the visual appearance of the emulsion changes from milky to transparent and slightly turbid (about 1 h). The MVL suspension was centrifuged at 100 × g to precipitate the larger-sized portion of the particles, and then washed with PBS 7.4 three times and filtered through a 70-μm Cell Strainer (Falcon®, Corning, NY) to remove any remaining lipid aggregates. The MVL suspension was stored at 4 °C for later characterization and drug quantification.

When SBE-β-CD was used in the MVL preparations, the W<sub>1</sub> phase was slightly modified. First, 1 mg of I3A was dissolved in EtOH, which was later removed by nitrogen flushing. Afterwards, 1 ml of 2% w/v SBE-β-CD and 50 mg of sucrose was added to the I3A residues and sonicated for 20 minutes. Then, the W<sub>1</sub> phase was agitated in an incubation shaker at 25 °C and 200 rpm for 2 days to ensure that all drug residues were brought into solution. The rest of the MVL

protocol was the same including the same amount of I3A added to the O phase. The preparation of MVLS-SBE- $\beta$ -CD-I3A is schematically illustrated in **Figure 1**.

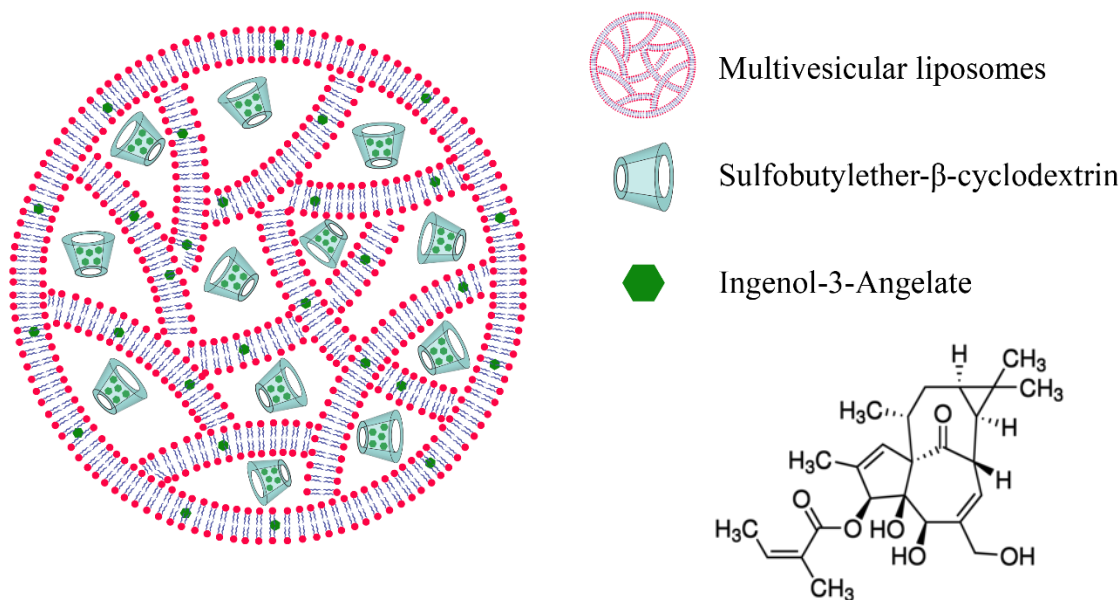


**Figure 1** Schematic diagram of the composition of MVLS loaded with I3A-complexed with SBE- $\beta$ -CD.

### 2.2.3 MVLS particle characterization

MVLS were characterized for particle size distribution, morphology, charge, and vesicle count. The measurement of MVL size and distribution was performed using a Mastersizer 3000 laser diffraction particle size analyzer (Malvern, UK). The morphology of the MVLS was examined using a brightfield upright light microscope (DM750 Leica, Germany) with 10 $\times$  and 40 $\times$  objectives. MVLS were stained with trypan blue solution 0.4% (w/v) in PBS (Corning, VA). The Zeta potential of MVLS was measured using a Zetasizer nano-ZS (Malvern, UK) and the dispersion medium was dd.H<sub>2</sub>O. Also, the stained MVLS were counted using a Luna-II<sup>TM</sup> automated cell counter (Logos Biosystems, Republic of Korea). All experiments were conducted in triplicate.

#### 2.2.4 Confirmation of I3A complexation with SBE- $\beta$ -CD

The unique structure of SBE- $\beta$ -CD can enhance the aqueous solubility of hydrophobic molecules through having an inner hydrophobic cavity that can physically partition the molecule.<sup>25</sup> In order to confirm the inclusion of I3A and the nature of occurring interaction, the chemical shifts of free I3A, SBE- $\beta$ -CD and their complex were examined using <sup>1</sup>H-NMR spectroscopy (AVIII HD 400 MHz, Bruker, MA). Free I3A (375  $\mu$ g/ml) was dissolved in DMSO-d<sub>6</sub>, free SBE- $\beta$ -CD (20 mg/ml) was dissolved in D<sub>2</sub>O, while their inclusion complex (at same concentration of both components) was dissolved in D<sub>2</sub>O. The chemical shifts were presented in ppm using tetramethylsilane (TMS) as internal reference and processed using MestReNova software 14.2.1 (Mestrelab Research, Spain).

#### 2.2.5 HPLC method

The chromatographic analysis of I3A was carried out on high performance liquid chromatography (HPLC) system (LC-2010C HT, Shimadzu) with a reverse-phase C18 column (Phenomenex, 5  $\mu$ m particle size, 4.6  $\times$  150 mm) and a photodiode array (PDA) detector measuring the 210 nm channel ( $\lambda_{\text{max}}$  of I3A). The mobile phases were 0.1% acetic acid in water (A) and 0.1% acetic acid in acetonitrile (ACN) (B). All mobile phases were degassed by sonication for 20 min and filtered using a 0.45- $\mu$ m filter under vacuum. Gradient elution (50-95% B) over 7.5 min was employed at a flow rate of 1 ml/min, oven temperature of 25  $^{\circ}$ C, and injection volume of 20  $\mu$ l.

The HPLC method was validated by testing the method's specificity, sensitivity, linearity, accuracy, and precision. Specificity was assessed by running free I3A, blank MVLs, and MVLs-SBE- $\beta$ -CD-I3A. Linearity was tested using the least square regression analysis of a calibration curve that results from five standard concentrations of 0.5 - 50  $\mu$ g/ml. Sensitivity of the method was evaluated by limit of detection (LOD) and limit of quantification (LOQ) using the formulas:

$$LOD = \frac{3.3\sigma}{S}, LOQ = \frac{10\sigma}{S}$$

where  $\sigma$  is the standard deviation of the response and  $S$  is the slope of the calibration curve. Accuracy and precision of the method were evaluated by measuring low (0.5  $\mu\text{g/ml}$ ), medium (25  $\mu\text{g/ml}$ ) and high (50  $\mu\text{g/ml}$ ) concentrations of I3A on the same and on different days and assessed by the percent accuracy and relative standard deviation (RSD) of the measurements.

## 2.2.6 Determination of entrapment efficiency

The determination of entrapment efficiency (EE%) was made by directly by comparing the content of 1 ml of MVL total solution (including free I3A, large and small particles) to the content of 1 ml large MVLs separated by centrifugation at  $100 \times g$ . Both MVL samples were disrupted by MeOH (1:10 v/v) and bath sonicated for 15 min to ensure that all loaded I3A was freed. Afterwards, both solutions were filtered through a 0.22- $\mu\text{m}$  syringe filter prior to running on HPLC with the method described above. The EE% was calculated as follows:

$$EE\% = \frac{W_{large\ MVLs}}{W_{total}} \times 100$$

Where  $W_{large\ MVLs}$  expresses the amount of I3A encapsulated into large MVLs and  $W_{total}$  expresses the amount of I3A in the total MVLs solution.

## 2.2.7 *In vitro* release profile

The donor phase consisted of freshly prepared MVL-SBE- $\beta$ -CD-I3A (1 ml) that was loaded into a Float-A-Lyzer<sup>®</sup>G2 dialysis cassette (MWCO: 3.5-5 kDa). The acceptor phase consisted of 500 ml of PBS 7.4 maintained at 37 °C and stirred at 150 rpm. The sampling aliquots (10  $\mu\text{l}$ ) were taken from inside the dialysis cell to indirectly quantify the released drug through measuring the percent drug remaining. At each time point, the solution of the dialysis cell was weighted before and after taking the sampling aliquot (10  $\mu\text{l}$ ) through density calculations as

reported before <sup>26</sup>, which were used to account for volume changes in the dialysis cassette due to osmotic effects. This indirect method was used due to the high lipophilicity of I3A, which makes it difficult to achieve a balance between sink conditions and the detection limit of the HPLC method when sampling aliquots are withdrawn from the release medium. The samples were diluted with MeOH, sonicated, centrifuged, filtered, and analyzed by HPLC to determine drug content. For comparison of the release behavior, free I3A (300 µg/ml) dissolved in DMSO was added to Float-A-Lyzer<sup>®</sup>G2 dialysis cassette (MWCO: 3.5-5 kDa) and the release profile was measured. All experiments were conducted in triplicate.

### **2.2.8 *In vitro* cytotoxicity assay**

The colon carcinoma cell line CT26WT (ATCC CRL-2638) was used to examine the cytotoxicity of I3A and blank MVLs using a Resazurin Blue assay.<sup>27</sup> PBS 7.4 was used as a negative control, while doxorubicin was used as a positive control. Briefly, CT26WT were cultured in RPMI-1640 media (ATCC, VA) supplemented with 10% FBS (Corning, VA), 1 % penicillin-streptomycin (Fisher Scientific, NH). Cells were then placed in a humidified incubator maintained at 37 °C and 5% CO<sub>2</sub> until they reached 80% confluence as observed under light microscopy. Afterwards, cells were counted using a Luna-II<sup>™</sup> automated cell counter, appropriately diluted with fresh media, and moved to 96-well plates. Into each well, 90 µl of the cell suspension was added ( $2 \times 10^4$  cells per well) and incubated for 24 h. Then, 10 µl of the treatment solutions were added to designated wells (n = 3) and incubated for 4 days at 37 °C and 5% CO<sub>2</sub>. The viability of the cells was examined using the resazurin blue assay (Acros Organics, Belgium). Briefly, 10 µl of 55 µM resazurin blue in PBS was added to each well (final concentration of 5 µM) and incubated for 4 h. Then, the 96-well plate was fluorescently analyzed using a SpectraMax Gemini XS plate reader (Molecular Devices, CA) at an excitation wavelength



of 550 nm and an emission wavelength of 605 nm. The viability of each treatment well was compared to control PBS wells and analyzed by nonlinear regression on GraphPad Prism version 8 (GraphPad, CA) to determine the IC<sub>50</sub> values. Concentrations of I3A tested were 50, 100, 300, 500 and 700 µM. While for doxorubicin, the concentrations were 5, 10, 30, 50, 70 and 100 µM. Blank MVLs were examined by varying the vesicle count to be equivalent to the loaded I3A MVLs from  $3.56 \times 10^6$  to  $3.56 \times 10^7$  vesicles/ml.

## **2.2.9 *In vivo* pharmacokinetics study**

### **2.2.9.1 Blood sampling and pretreatment**

The pharmacokinetic profile of I3A and MVLs-SBE-β-CD-I3A were carried out by injecting a single dose of both treatments subcutaneously (s.c.) into healthy C57BL/6J mice. A 25 µg dose of I3A was dissolved in 50 µl of PEG 400 and injected into five mice.<sup>12</sup> Whereas 50 µl of MVLs-SBE-β-CD-I3A loaded with 0.25 µg of I3A, due to the limited loading capacity of MVLs, was administered in PBS 7.4 to five other mice. Blood samples were withdrawn from the ophthalmic veins at predetermined five time points. For I3A, the time points were 0.5, 2, 4, 6 and 8 h (n = 2 per time point), while for MVLs-SBE-β-CD-I3A the time points were 0.5, 4, 8, 24 and 48 h (n = 2 per time point). The blood samples were immediately added to EDTA-coated vial to prevent blood clotting. Then, samples were centrifuged at  $2000 \times g$  for 5 min and the plasma supernatants were collected and stored at -80 °C for later analysis.

Samples were pretreated in order to precipitate the plasma proteins and obtain the drug aliquots for analysis. Briefly, plasma samples were allowed to thaw at room temperature for 1 h. Then, 40 µl of each sample was mixed with 4 µl of freshly prepared tacrolimus (TRL) in ACN as internal standard (final concentration of 1 µg/ml), and further diluted with 200 µl of cold ACN to precipitate the plasma proteins. The samples were thoroughly mixed together by vortexing for 5

min, then placed at  $-20\text{ }^{\circ}\text{C}$  for 1 h to help precipitate the proteins. Then, samples were centrifuged at  $13,000 \times g$  for 10 min and the supernatants were collected. The supernatant containing drug was concentrated by drying the solvent using a CentriVap concentrator (Labconco, Lenexa, KS) and then reconstituted in 40  $\mu\text{l}$  of the LC-MS/MS injection solution (50% ACN/50%  $\text{H}_2\text{O}$ /0.1% formic acid (FA)) followed by vortexing for 5 min.

#### 2.2.9.2 Sample analysis by LC-MS/MS

The analysis of I3A content in the blood samples were performed using a Shimadzu Prominence LC system (LC-20AD pumps, SIL-20AC HT autosampler, CTO-20A column oven, CBM-20A controller) coupled to an AB Sciex 3200 Q Trap LC-MS/MS system. At first, I3A and TRL were infused into the MS on positive mode using multiple reaction monitoring (MRM) in order to determine the precursor (Q1) and product (Q3) ions (Scan mode 100-1000 Da) (**Table 2**). Then, source parameters were optimized by flow injection analysis (FIA) using the Analyst software 1.5.1. The optimized source parameters were as follows: curtain gas was 11 Psi, Ion spray voltage was 5,500 V, source temperature was  $550\text{ }^{\circ}\text{C}$ , ion source gas 1 was 30 Psi, ion source gas 2 was 13 Psi, dwell time was 150 ms and the nitrogen collision gas was medium. The chromatographic separation was performed according to a modified reported protocol.<sup>28</sup> Briefly, a reversed-phase C18 column (Agilent ZORBAX Eclipse XDB-C18, 3.5  $\mu\text{m}$ ,  $2.1 \times 50\text{ mm}$ ) with an oven temperature of  $35\text{ }^{\circ}\text{C}$ , flow rate of 0.2 ml/min and injection volume of 10  $\mu\text{l}$  was used to elute the analytes into MS/MS system. The mobile phases were 0.1% FA in  $\text{H}_2\text{O}$  (A) and 0.1% FA in ACN (B) at initial B gradient of 50 %. The time program starts with isocratic 50% (B) until 1 min that was directed to the waste through the six-way switching valve to minimize the MS contamination. Then, a gradient mode was employed from 1.0 min (50% B) to 1.8 min (80% B), then to 100% B at 3.0 min, isocratic at 100% B from 3.0 – 4.0 min, then a re-equilibration step to

50 % at 5.5 min that was held until 7 min. To quantify the drug content from the intensity signals received from the LC-MS/MS, a calibration curve of seven standard concentrations (0.195 - 25 ng/ml) were run and fit using least square regression analysis with TRL (1 µg/ml) as an internal standard.

Analyte	LC-MS/MS parameters						
	Q1 (m/z)	Q3 (m/z)	RT (min)	DP (V)	EP (V)	CE (V)	CXP (V)
I3A	453.51	353.2	4.40	71	10.5	26	4
TRL	826.72	616.3	5.09	66	9.5	52	6

**Table 2** LC-MS/MS optimized parameters that were used for I3A and TRL quantification. RT stands for retention time, DP stands for declustering potential, EP stands for entrance potential, CE stands for collision energy and CXP stands for cell exit potential.

### 2.2.10 Statistical analysis

All experiments were conducted in triplicate and the data are expressed as the mean  $\pm$  standard deviation. Significant differences were examined by student t-test or one-way analysis of variance (ANOVA) followed by Tukey's post hoc tests ( $*p \leq 0.05$ ,  $**p \leq 0.01$ ,  $***p \leq 0.001$  and  $****p \leq 0.0001$ ) using GraphPad Prism Software version 8. Comparisons are considered not statistically significant (ns) when  $p > 0.05$ .

## 2.3 Results

### 2.3.1 MVLs particle characterization

The preparation of large MVLs was confirmed by characterizing their particle size and morphology. The particle distribution of MVLs and MVLs-SBE- $\beta$ -CD-I3A was measured by static light scattering given the expected micron size range. The particles' size distribution showed that MVLs are composed of micron particles with 80% of the particles in the range of 4.57 – 70.4  $\mu\text{m}$  and  $D_v(50) = 9.77 \pm 0.33 \mu\text{m}$ , while MVLs-SBE- $\beta$ -CD-I3A showed a narrower size distribution with 80% of the particles in the range of 12.3 – 46.1  $\mu\text{m}$  and larger  $D_v(50) = 23.8 \pm 0.29 \mu\text{m}$  (**Figure 2a and 2b**). The morphology of the developed MVLs, blank and drug loaded, showed that the majority of the particles were spherical and in the micron range. Also, the multiple nonconcentric aqueous vesicles, which is a main characteristic of MVLs, were clear from the particle surface texture (**Figure 2c and 2d**). The Zeta potential of blank MVLs were  $-62.2 \pm 2.58 \text{ mV}$ , while MVLs-I3A (without SBE- $\beta$ -CD) and MVLs-SBE- $\beta$ -CD-I3A were less negative at  $-58.1 \pm 1.72 \text{ mV}$  and  $-39.5 \pm 1.12 \text{ mV}$ , respectively. The vesicle counts were also measured. The vesicles in MVLs were counted to be  $3.56 \times 10^6$  vesicles/ml, which are more numerous than MVLs-SBE- $\beta$ -CD-I3A, with a vesicle count of  $1.84 \times 10^6$  vesicles/ml. These results are in accordance with the optical images of both MVLs (shown in **Figure 2c and 2d**) where blank MVLs appeared more frequently than MVLs-SBE- $\beta$ -CD-I3A. Thus, the MVLs we produced were large vesicles that should be able to circumvent macrophage clearance.

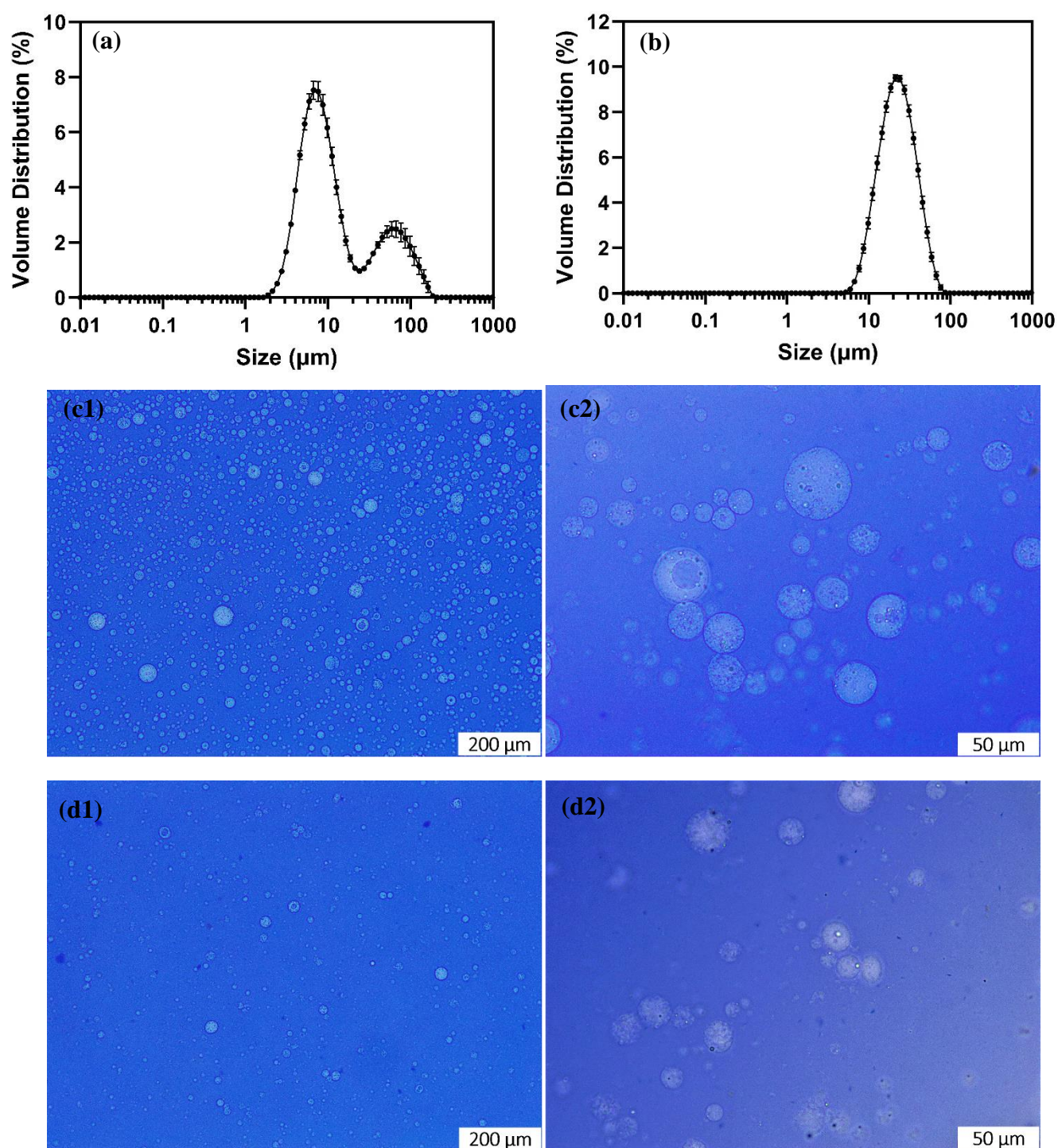


**Figure 2** MVL particle characterization: (a) volume size distribution of MVLs, (b) volume size distribution of MVLs-SBE-β-CD-I3A, (c1) Morphology of MVLs at 100×, (c2) morphology of MVLs at 400×, (d1) morphology of MVLs-SBE-β-CD-I3A at 100×, and (d2) morphology of MVLs-SBE-β-CD-I3A at 400×.

### 2.3.2 Confirmation of I3A complexation with SBE- $\beta$ -CD

SBE- $\beta$ -CD was utilized to load more I3A into the aqueous compartments of MVLs.  $^1\text{H}$ -NMR was used to confirm the complexation of I3A into the SBE- $\beta$ -CD structure. As shown in **Figure 3a and 3b**, the chemical shifts of I3A were observed in the range of 0.5 – 6.5 ppm, but SBE- $\beta$ -CD protons were primarily present in a narrower range of 1.5 – 5.5 ppm. Thus, the complexation of I3A with SBE- $\beta$ -CD may be supported if we locate the I3A protons for their inclusion complex (SBE- $\beta$ -CD-I3A) at the difference between these specified ranges (i.e. 0.5 – 1.5 ppm and 5.5 – 6.5 ppm). This is clearly shown in **Figure 3c**, where SBE- $\beta$ -CD overlaps with the I3A chemical shifts only between 1.5 – 5.5 ppm, but I3A protons appeared out of that range and were almost typical of the free I3A protons in **Figure 3a**. In addition, the  $^1\text{H}$ -NMR spectra revealed a few shifts between the free I3A and the complexed I3A protons which may be attributed to the physical interaction between the I3A and the SBE- $\beta$ -CD inner hydrophobic sites. For instance, a very characteristic proton of I3A exists at the carbon right before the ester bond (marked C3 in red on **Figure 3**) connecting the ingenol moiety to the angelate moiety.<sup>29</sup> It was observed in the free I3A spectrum at 5.77 ppm, while it was shifted to 5.65 ppm in SBE- $\beta$ -CD-I3A. This might be assigned to a physical interaction happening between the ingenol moiety (containing C3 proton) with the hydrophobic cavity of SBE- $\beta$ -CD.

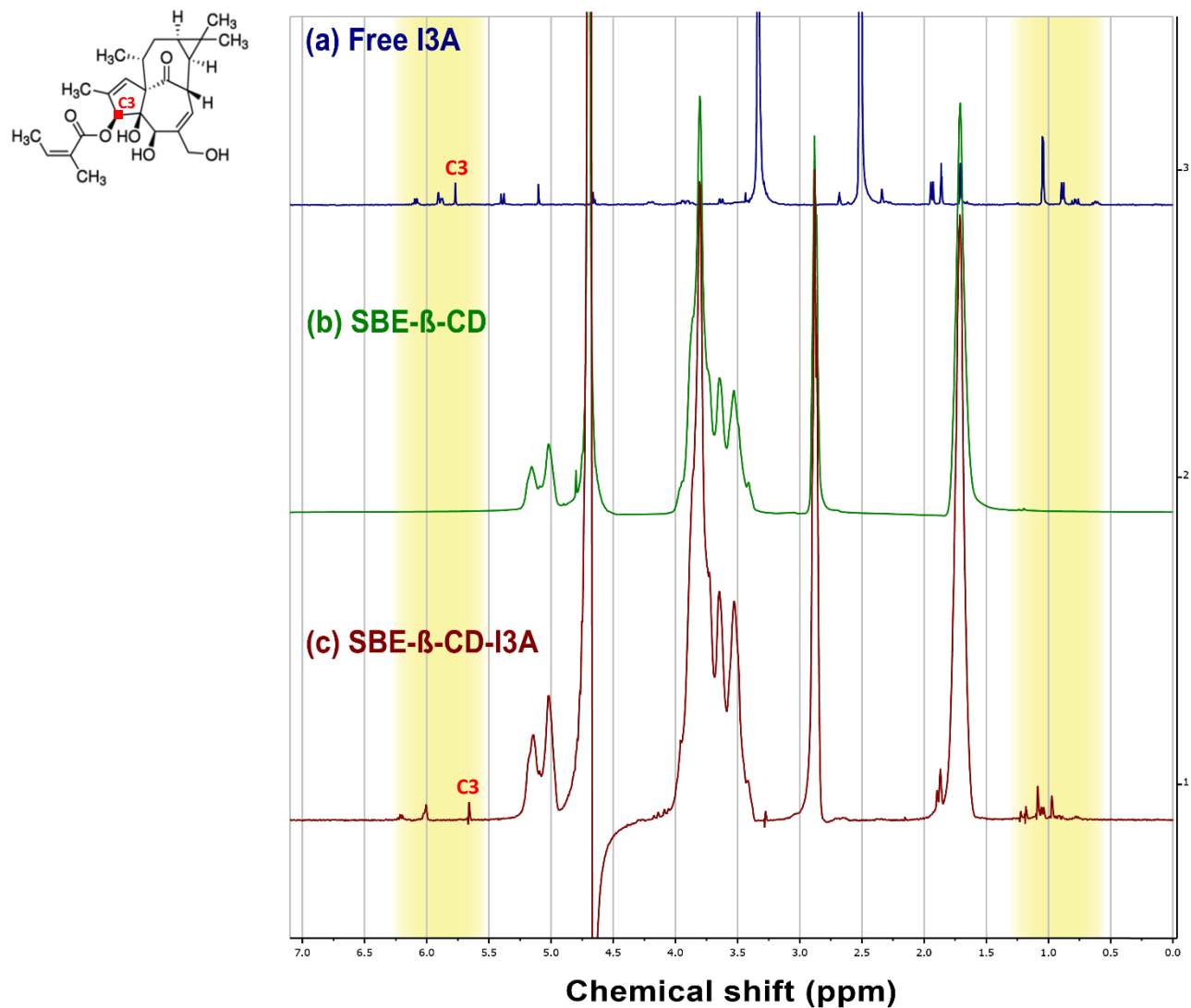


**Figure 3**  $^1\text{H}$ -NMR spectra of (a) free I3A, (b) SBE- $\beta$ -CD and (c) SBE- $\beta$ -CD-I3A, which supports the complexation of I3A into SBE- $\beta$ -CD.

### 2.3.3 HPLC method validation

The specificity of the HPLC method was confirmed by running the MeOH extraction solution, extracted blank MVLs, and extracted MVLs-SBE- $\beta$ -CD-I3A encapsulating I3A, at concentration of 192  $\mu\text{g/ml}$ . As shown in **Figure 4a**, the method was able to specifically detect I3A at a retention time of 6.95 min for MVLs-SBE- $\beta$ -CD-I3A with no interfering peaks near the

peaks of interest. In regard to the method linearity, five standard concentrations 0.5 - 50 µg/ml were used to build a calibration curve between the area of the peak (A) at 6.95 min obtained from HPLC at each corresponding concentration level (C). The least square regression analysis was used to test the linearity of the relationship between A and C which yielded  $A = (33177 \times C) + 1428.7$  and a square of the correlation coefficient ( $R^2$ ) of 0.9996 (**Figure 4b-d**). As for sensitivity, LOD of I3A was found out to be 0.15 µg/ml, while LOQ was determined to be 0.45 µg/ml. Additionally, the accuracy and precision of the method resulted in a good predictive accuracy and RSD less than 10% for drug measurements on the same and following day (**Table 3**). These results suggest the calibration curve can be used to quantify the unknown concentration of EE% and release samples.



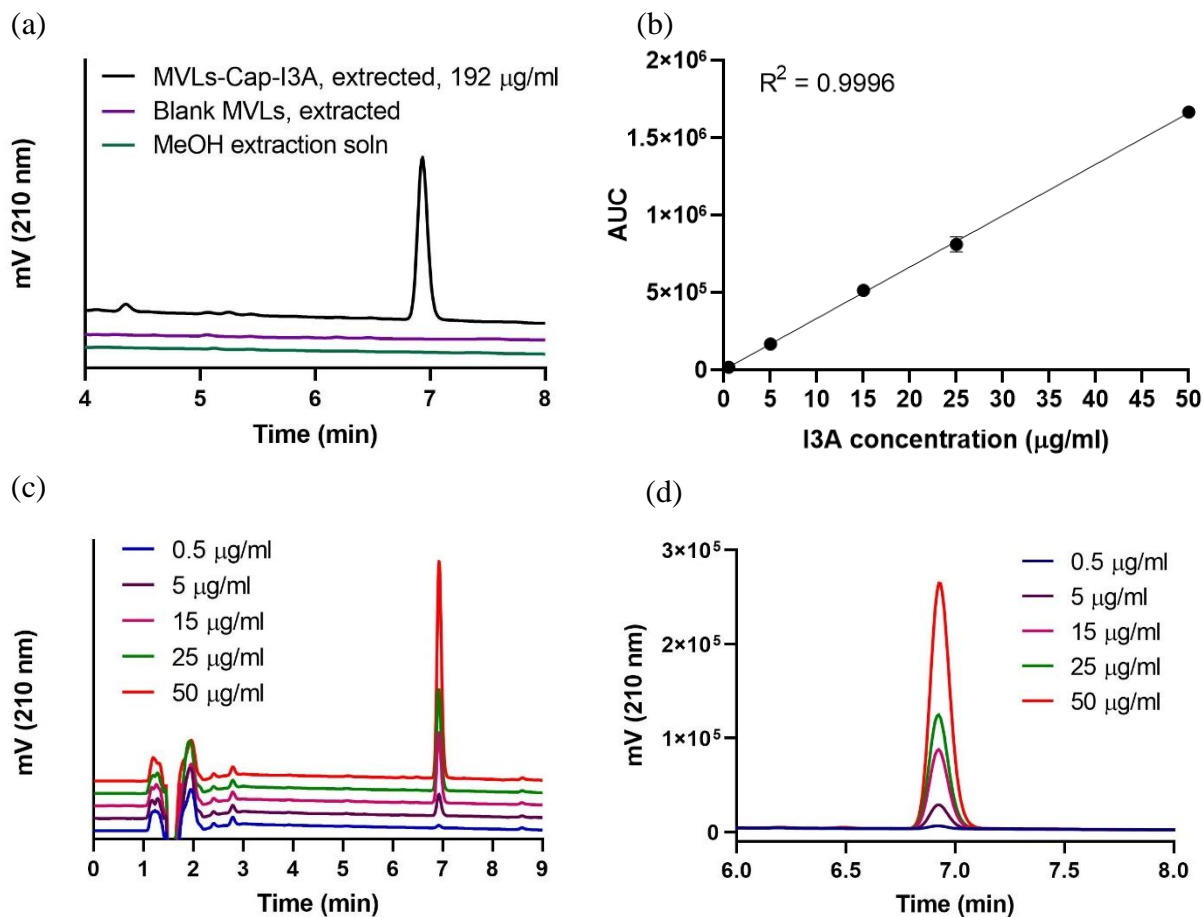


**Figure 4** (a) The specificity of the developed HPLC method for detecting I3A following its extraction from MVLs, (b) The linearity of the HPLC method as examined by the least square regression analysis, (c) (d) show the chromatogram of the five standard concentration levels that were used to build the calibration curve.

Theoretical concentration ( $\mu\text{g/ml}$ )	Intraday measurement			Inter-day measurement		
	Measured	Accuracy	RSD	Measured	Accuracy	RSD
	concentration ( $\mu\text{g/ml}$ )	(%)	(%)	concentration ( $\mu\text{g/ml}$ )	(%)	(%)
0.5	0.49	97.87	5.49	0.51	102.72	3.86
25	25.22	100.87	0.74	25.31	101.25	0.11
50	50.17	100.35	0.70	49.03	98.07	0.20

**Table 3** The accuracy and precision of the developed HPLC method for measuring I3A concentration following intra and inter-day measurements. (Values are the mean  $\pm$  SD, n = 3)

### 2.3.4 MVL entrapment efficiency and *in vitro* release behavior

The EE% of I3A into the MVLs-SBE- $\beta$ -CD was measured from triplicate samples to be  $20.51 \pm 2.29$  %. We also confirmed the effect of SBE- $\beta$ -CD on enhancing the I3A loading into MVLs by measuring the concentration of loaded I3A in MVLs formulation prepared with and without SBE- $\beta$ -CD. The results showed that with SBE- $\beta$ -CD, the concentration of loaded I3A significantly increased to  $191.81 \mu\text{g/ml}$  compared to  $11.55 \mu\text{g/ml}$  without SBE- $\beta$ -CD, which is a 17-fold improvement in the I3A loading (**Figure 5a**). The *in vitro* release study showed a prolonged release profile for MVLs-I3A over 96 h with 50% of the drug was released after 24 h, then the other 50% was slowly released in the following 72 h. For free I3A, most of the drug was released within the first 12h, in comparison. Thus, MVLs demonstrated sustained release of I3A (**Figure 5b**).

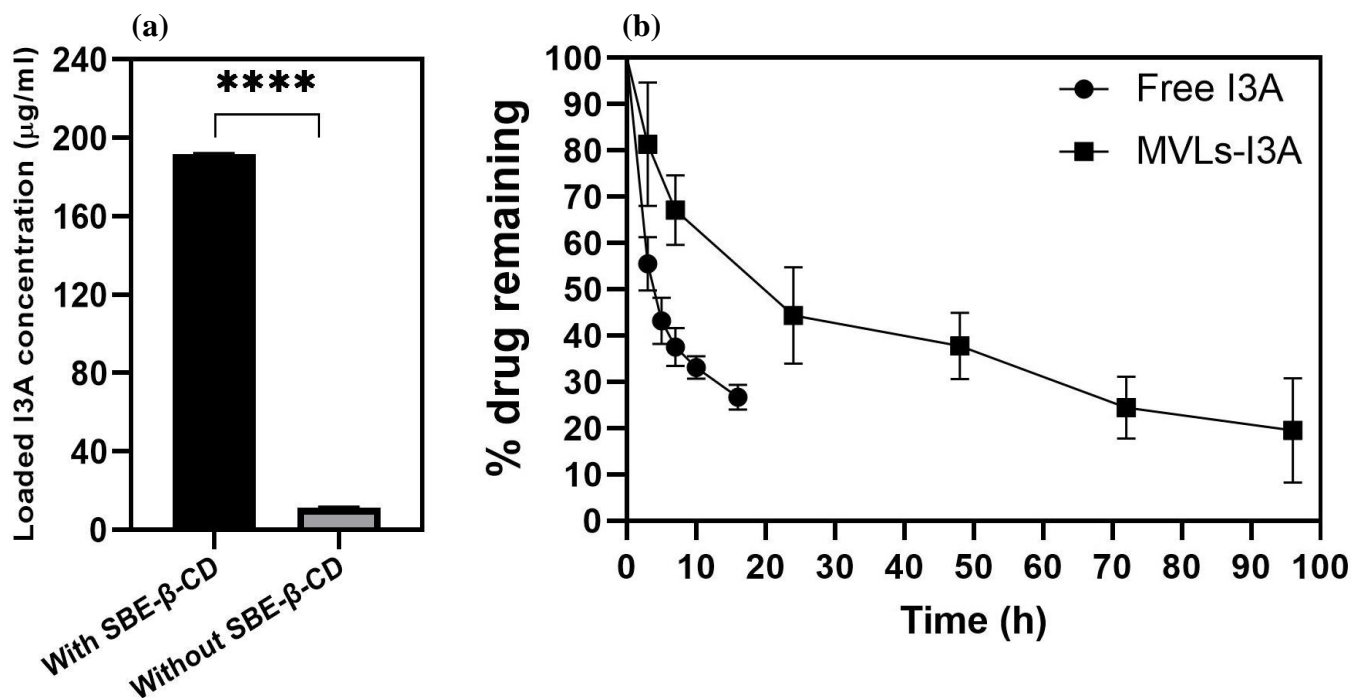


**Figure 5** (a) Effect of adding SBE-β-CD on the loading of I3A into MVLSs (\*\*\*\*  $P \leq 0.0001$ ) (b) *in vitro* release profile of MVLS-I3A demonstrates its prolonged release as compared to free I3A. (values are the mean  $\pm$  SD,  $n = 3$ ).

### 2.3.5 *In vitro* cytotoxicity assay

The potential of I3A as a cytotoxic agent on cancer cells was evaluated by examining its  $IC_{50}$  in the CT26WT cell line, with PBS 7.4 used as a negative control and doxorubicin was used as a positive control. As shown in **Figure 6a**, I3A showed cytotoxicity in CT26WT with an  $IC_{50}$  of  $132.7 \pm 31.6 \mu M$ . I3A was less potent than doxorubicin that showed  $IC_{50}$  of  $18.37 \pm 2.88 \mu g/ml$ , which suggests the requirement for larger doses of I3A in order to induce cytotoxicity. Also, blank MVLSs were tested for biocompatibility of various vesicle counts from  $3.56 \times 10^6$  to  $3.56 \times 10^7$  vesicles/ml, which showed good biocompatibility as the relative cell viability percent remained above 94% at the highest vesicle count (**Figure 6b**). Thus, blank MVLSs exhibit minimum, if any,

inherent cytotoxicity, and I3A is suggested to be the only responsible for inducing cytotoxicity at the measured  $IC_{50}$ .

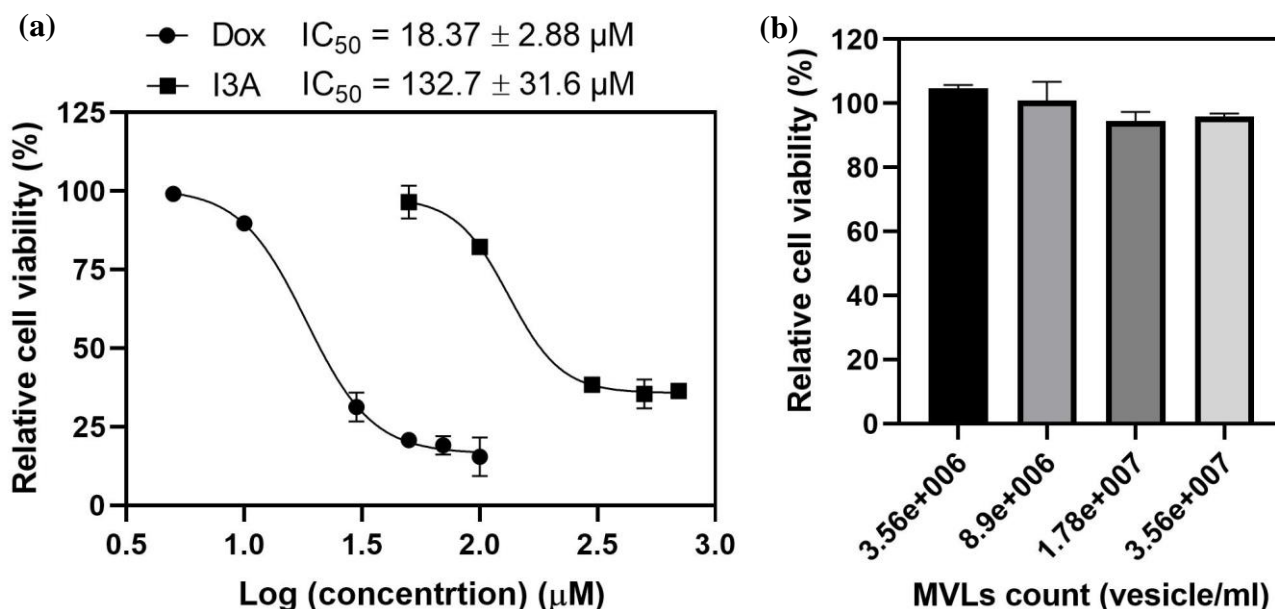


**Figure 6** The cytotoxicity study of (a) I3A in CT26WT using the Resazurin blue assay, (b) blank MVLs. The  $IC_{50}$  values were determined using nonlinear regression on GraphPad Prism 8 (% relative cell viability values are the mean  $\pm$  SD,  $n = 3$ ), doxorubicin (Dox) and PBS 7.4 were used as positive and negative controls, respectively.

### 2.3.6 *In vivo* pharmacokinetic study

#### 2.3.6.1 Sample analysis by LC-MS/MS

The infusion of I3A and TRL individually on the MS indicated the precursor ion with the highest intensity to be the sodium adduct  $[M + Na]^+$  for I3A (453.51  $m/z$ ) and also for TRL (826.72  $m/z$ ). Then, the MS/MS product ions were selected by the instrument according to the highest intensity, which revealed the product of 353.2  $m/z$  for I3A, and 616.3  $m/z$  for TRL. Then, LC method was optimized in order to detect optimum and well-separated signals for the analyte and internal standard. The developed method was tested for specificity by running blank and loaded

plasma samples. The I3A signal was detected at a retention time of 4.40 min, while the retention time of TRL was found to be 5.07 min (**Figure 7a**) with no interfering peaks from the blank plasma. The method was also tested for linearity using least square regression analysis by running calibration standards between 0.195 - 25 ng/ml with 1 µg/ml of TRL. A plot of (Analyte area/IS area) and (analyte concentration/IS concentration) was found to be linear  $R^2 = 0.9957$ , and the following regression equation was obtained: (Analyte area/IS area) =  $2.5168 \times$  (analyte concentration/IS concentration) – 0.0008 (**Figure 7b**).

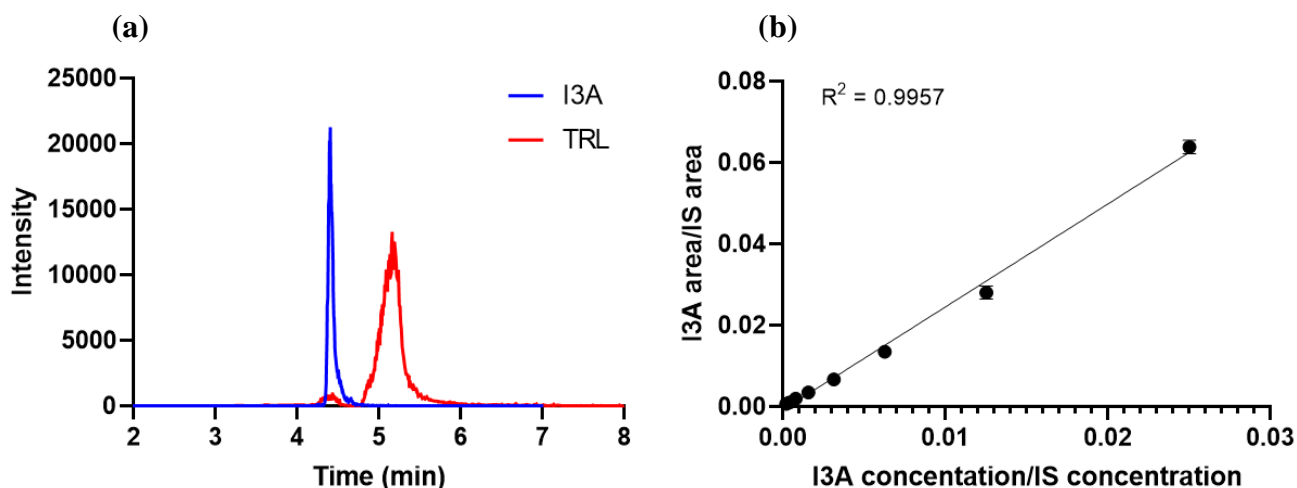


**Figure 7** (a) The LC-MS/MS chromatogram showing I3A and tacrolimus (TRL) used as internal standard, (b) the calibration curve of seven standard concentrations showing the linearity of the method as analyzed by the least square regression analysis (n = 3).

#### 2.3.6.2 Analysis of I3A pharmacokinetic profile

Based on the developed LC-MS/MS method, the collected blood samples from the mice at various predetermined points were quantified for the concentration of I3A. The concentration (ng/ml) against time (h) profile following a single s.c. injection of I3A or MVLs-I3A was plotted (**Figure 8**) to assess the differences in pharmacokinetic parameters. I3A was detectable in both samples in all the time points. In the free I3A group, the maximum plasma concentration ( $C_{max}$  of

1.637 ng/ml) occurred at the first time point 0.5 h ( $T_{\max}$ ) suggesting a rapid absorption from the injection site of the free drug. Elimination followed first order kinetics through the last sample point at 8 h (**Figure 8a**). On the other hand, the MVLs-I3A plasma concentration-time profile showed that the drug concentration increased gradually until it peaked at a later  $T_{\max}$  of 8 h, with a concentration of 0.4211 ng/ml ( $C_{\max}$ ). Then, the I3A concentration decreased more slowly than free I3A through the last sampled time point (48 h), which suggests that MVLs prolonged the release of I3A and its residence within blood (**Figure 8b**). However, it was obvious that free I3A sample exhibits higher concentrations at all time points than MVLs-I3A sample due to the difference in the injection dose (**Figure 8c**). It was also observed that the area under I3A concentration vs time curve at the last time point ( $AUC_{0-t}$ ) for MVLs-I3A is much larger than free I3A. The pharmacokinetic parameters were calculated using Excel software with the method of residuals for Flip-Flop kinetics since MVLs showed a sustained release profile (**Table 4**), consistent with absorption-controlled elimination kinetics.

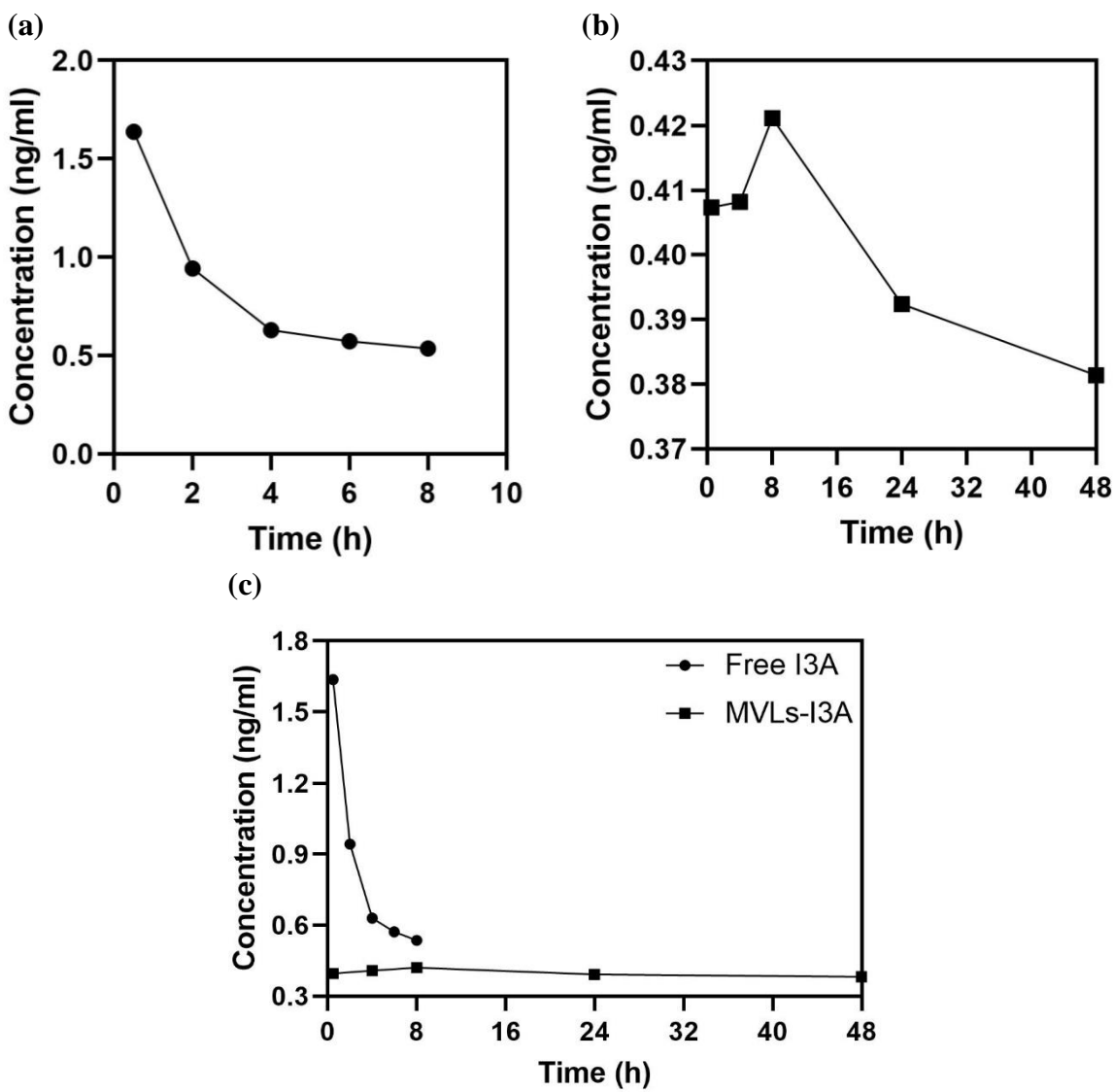


**Figure 8** The plasma concentration-time profile of (a) free I3A, (b) MVLS-I3A and (c) both of them plotted on the same graph to show the difference in concentration magnitudes between both samples. The blood samples were collected following a single s.c. injection of 25 ug free I3A dose and 0.25 ug dose of loaded I3A (data presented are the mean of two samples per each time point).

Parameter	Free I3A	MVLs-I3A
$C_{\max}$ (ng/ml)	1.637	0.4211
$C_{\max}/\text{dose}$ (ng/ml.μg)	0.0655	1.6844
$T_{\max}$ (h)	0.5	8
$K_e$ (h <sup>-1</sup> )	0.0393	0.0393
$K_a$ (h <sup>-1</sup> )	0.8251	0.0012
$AUC_{0-t}$ (ng.h/ml)	When t = 8 h, 5.814	When t = 8 h, 3.066
		When t = 48 h, 18.86
		When t = 8 h, 12.264
$AUC_{0-t}/\text{dose}$ (ng.h/ml.μg)	When t = 8 h, 0.2326	When t = 48 h, 75.44

**Table 4** The pharmacokinetic parameters extracted from the plasma-concentration time profile of free I3A (0 – 8 h) Vs MVLs-I3A (0 – 48 h) following a single s.c. injection of 25 μg free I3A dose and 0.25 μg dose of loaded I3A (data presented are the mean of two samples per each time point).



## 2.4 Discussion

The potential of I3A as a dual chemotherapeutic and immunotherapeutic agent has encouraged the drug's investigation as a therapy for cancers such as brain tumors (e.g. glioma).<sup>30,31</sup> However, the poor water solubility of the drug, wide tissue distribution and the rapid clearance by macrophages impede its use for that purpose. To solve those issues, MVLs were investigated as a long-acting vehicle that can circumvent the rapid clearance due to their large particle size (5-50  $\mu\text{m}$ ).<sup>21,24</sup> Besides, MVLs were shown to sustain the drug release given the presence of the unique inner lipid networks that retard the diffusion of the entrapped drug and thus prolong the release.<sup>18</sup> However, the ratio between the MVLs lipid network to the aqueous compartments (5:95) limit the MVLs loading capacity for lipophilic drugs such as I3A. To solve such issue, it was proposed to introduce I3A into the large aqueous compartments through complexing it with a well-known solubility enhancer such as SBE- $\beta$ -CD.<sup>25,32</sup> We originally designed MVLs for glioma administration to examine I3A's potential in the upregulation of IL13R $\alpha$ 2. In this chapter, we just developed MVLs as long-acting formulation for the localized delivery of I3A. The preparation, particles characterization, drug content quantification, *in vitro* release profile study and *in vivo* pharmacokinetic profile were examined for MVLs-SBE- $\beta$ -CD-I3A. Given the successful preparation of MVLs, we plan to utilize this formulation in glioma treatment with our collaborator in the near future.

The successful preparation of MVLs was facilitated by the optimization of several parameters such as lipid composition, use of emulsion stabilizers, homogenization power, and rate of nitrogen flushing. The preparation protocol used in this study relied on optimization studies reported before that produced stable MVLs structure that can sustain the drug release.<sup>18,23</sup> DOPC and DPPG are the phospholipids responsible for forming the double bilayers of MVLs. Cholesterol

is reported to impart rigidity to the inner lipid network of MVLs, thus preventing the nonconcentric compartments from falling apart, forming a barrier to prevent payload leakage, and helping to sustain the release.<sup>33</sup> Triolein is a unique lipid component that distinguishes MVLs over conventional liposomes. It is thought to be responsible for stabilizing the intersections between the inner lipid network, and thus could be tailored to control the release profile.<sup>34,35</sup> The use of emulsion stabilizers is also essential for imparting good stability to MVLs. For instance, L-lysine plays a vital role in preventing emulsion drops from aggregating by imparting negative charges, thus they repel each other.<sup>36</sup> Moreover, the homogenization power is essential for preparing MVLs. When the homogenization power was weak ( $< 10,000$  rpm) when emulsifying W<sub>1</sub>/O, phase separation was observed and MVLs were not obtained. The last critical factor is the removal of the chloroform from the emulsion to obtain MVLs. We found that when the rate of nitrogen flushing was too high, the emulsion became partially or totally cracked depending on the length of flushing. Thus, a low nitrogen purging for 1-2 h is necessary to slowly remove the chloroform and obtain MVLs.

The particle size analysis demonstrated that loaded MVLs exhibit a single narrow peak with 80% of the particles having a size greater than 5  $\mu\text{m}$  for which is required to avoid the macrophage uptake.<sup>37</sup> The characteristic morphology of MVLs was observed using brightfield light microscopy, which showed spherical particles with rough surface texture, indicating the presence of the interconnected lipid network. The Zeta potential analysis showed that all MVLs, blank and loaded, have high negative charge (less than  $-30$  mV) which indicate high emulsion stability of the particles and in accordance with the MVLs prepared by Li et al.<sup>38</sup> The loaded MVLs were relatively less negative than blank MVLs, which may be attributed to the presence of I3A molecules. The Zeta was more reduced for MVLs-SBE- $\beta$ -CD-I3A ( $-39.5 \pm 1.12$  mV) than MVLs-

I3A (no SBE- $\beta$ -CD) ( $-58.1 \pm 1.72$  mV), which may be assigned to the higher loading of I3A when SBE- $\beta$ -CD was used. The interaction between I3A and SBE- $\beta$ -CD was confirmed using  $^1\text{H-NMR}$  through shifting of the characteristic protons of I3A in the spectrum of SBE- $\beta$ -CD-I3A. The analysis of the  $^1\text{H-NMR}$  spectra suggested that I3A and SBE- $\beta$ -CD are physically interacting with each other due to few shifts in the I3A protons after the complexation.

The use of SBE- $\beta$ -CD in loading I3A significantly increased the loaded amount into MVLs. The unique structure of SBE- $\beta$ -CD allows lipophilic drugs to be complexed within its cavity and then the hydrophilic portions of the SBE- $\beta$ -CD help dissolve the whole complex in water.<sup>25</sup> Azzi et al. (2018) used a similar approach to enhance the loading of quercetin into a liposomal formulation. They were able to enhance total loading of the lipophilic molecule quercetin into the liposomes; however, they reported a low EE% of  $27.9 \pm 6.7\%$  which is similar to what we measured,  $20.51 \pm 2.29\%$ . They attributed the low encapsulation efficiency to the inability of the liposomes' aqueous compartments to host much complexed SBE- $\beta$ -CD, and thus much of the complex is not entrapped.<sup>39</sup> However, this low entrapped complex still contributed into getting 17-fold more of the I3A loaded into MVLs than without using it. Actually, when we tried the same amount of I3A (1.7 mg) without SBE- $\beta$ -CD, the emulsion cracked, which may be attributed to the harmful effect of the lipophilic drug on lipid bilayer formation as reported by Zhang et al.<sup>22</sup> The *in vitro* release study demonstrated the potential of MVLs as a long-acting formulation, where it sustained the I3A release over 96 h, compared to the free solution which completed in 12 h. In the case of lipophilic molecules, the release occurs from the outermost lipid bilayers, then inner entrapped molecules start to gradually diffuse into the outer bilayer until the whole particles erode.<sup>19</sup> MVLs were reported to be stable from days to a few weeks and the concentration of triolein plays a vital role in sustaining the release. In our study, we used a low triolein concentration

(1.7 mM) in order to maximize the EE%, as excess triolein (3 – 5 mM) was reported to compete with lipophilic molecules in the lipid bilayers, and thus lower EE%.<sup>40</sup> A similar sustained profile was reported by Luo et al. (2016), where MVLs were used for loading oleanolic acid. Their release profile is consistent with ours, where 50% of the drug was released after ~12 h and then 80% was released over 125 h.<sup>18</sup> To evaluate the retention of MVLs in the injection site, we plan to use a similar approach to the one reported by Zhang et al. (2016) where they used fluorescently-labeled phospholipids in preparing MVLs. Then, they used an *in vivo* imaging system to real-time monitor the changes in MVLs fluorescence intensity in the injection site over time. In their study, MVLs showed retention in the injection site over 144 h as evident by the reduction in the MVLs fluorescence intensity.<sup>20</sup>

The cytotoxicity of MVLs was examined by varying the vesicle count to be equivalent to the loaded I3A-MVLs from  $3.56 \times 10^6$  to  $3.56 \times 10^7$  vesicles/ml, and the results showed high relative cell viability for the blank vehicle at all tested counts (> 94%). This biocompatibility of the MVLs is probably due to the natural sources of the lipids used in MVLs preparation.<sup>21,41</sup> For I3A cytotoxicity, a broad range was tested on the CT26WT cell line, since the sensitivity to the drug varies from one cell line to another. For instance, the IC<sub>50</sub> of I3A on HCC2998 human colon carcinoma cell line was reported to be 30 µM, whereas in a less sensitive human colorectal carcinoma cell line such as HCT116, the IC<sub>50</sub> was found to be 120 µM.<sup>42</sup> For CT26WT, the IC<sub>50</sub> was found to be  $132.7 \pm 31.6$  µM suggesting it is a low sensitivity cell line. Since the long-term objective of the study is the administration of MVLs-I3A into glioma, the cytotoxicity will be examined on a glioma cell line in the future to test the sensitivity of the cell line to I3A.

The pharmacokinetic behavior of free and loaded I3A was examined by a pilot study following a single s.c. dose of free I3A and MVLs-I3A into C57BL/6J mice at 25 and 0.25 µg

doses, respectively. The free I3A profile showed a quick absorption, and the first time point ( $T_{\max}$  of 0.5 h) corresponded to the  $C_{\max}$  of 1.637 ng/ml, then the drug was quickly removed from the body with about 70% eliminated in 8 h. Assuming first order of elimination kinetics and using the method of residuals, the elimination rate constant ( $K_e$ ) could be calculated from the free I3A plasma-concentration time profile since the absorption phase was almost immediate ( $< 0.5$ h).  $K_e$  was determined by calculating the slope of the steep elimination phase of the free I3A points (4, 6 and 8 h time points) and equalizing it to  $-K_e/2.3$ .<sup>43</sup>  $K_e$  was calculated to be  $0.03933 \text{ h}^{-1}$  which should be equal in free and loaded I3A. The absorption rate constant ( $K_a$ ) of free I3A was calculated from the residual line slope which resulted in  $0.8251 \text{ h}^{-1}$ . On the contrary, MVLs-I3A showed a sustained release profile with a delayed  $T_{\max}$  of 8 h and a lower value of  $C_{\max}$ , 0.4211 ng/ml. The shape of the MVLs-I3A graph (**Figure 6b**) demonstrated a slow absorption phase followed by higher elimination phase, besides near plateau values were dominating the whole profile. This is a typical characteristic of Flip-Flop kinetics where  $K_a$  is the rate-limiting step of the pharmacokinetics ( $K_a < K_e$ ). Flip-Flop kinetics is commonly applied to sustained-release formulations such as MVLs since they demonstrate prolonged release from a few days to weeks.<sup>21</sup> To determine  $K_a$  of MVLs-I3A, the slope of the terminal part was calculated and equalized to  $-K_a/2.3$ . The calculation showed a lower  $K_a$  of  $0.00115 \text{ h}^{-1}$ , compared to about 34-fold  $K_e$  of  $0.03933 \text{ h}^{-1}$  which is consistent with Flip-Flop kinetics ( $K_a < K_e$ ). Also, the  $K_a$  of the MVLs-I3A ( $0.00115 \text{ h}^{-1}$ ) was much lower than  $K_a$  of free I3A ( $0.8251 \text{ h}^{-1}$ ) which is consistent with the difference in absorption rate in each case. The slow release from MVLs may be attributed to their large size, thus avoid macrophage clearance, and also the difficulty of drug diffusion given the presence of multiple lipid barriers. Lastly, the  $AUC_{0-t}$  was calculated demonstrating a 3-fold larger area for MVLs than free I3A. This result is usually observed when the dose is equivalent as an

indication of the improved bioavailability due to the prolonging effect of MVLS.<sup>18,19,35</sup> However, in our case the dose was not equivalent. We plan to investigate such observation in a future study when we administer equivalent dose for both samples, given the improvement of loading due to SBE- $\beta$ -CD, and increase the number of mice per time point.

## 2.5 Conclusion

MVLS were prepared and characterized as a long-acting formulation for I3A. Particle size analysis and light microscopy confirmed the characteristics of MVLS such as large size ( $> 5 \mu\text{m}$ ), that helps evade the macrophage clearance, and the presence of an inner lipid network that helps sustain the drug release in loaded MVLS. The use of SBE- $\beta$ -CD in I3A loading demonstrated a significant improvement in the MVLS' loading capacity probably by introducing more of I3A into the aqueous compartments. The *in vitro* release study and the *in vivo* pharmacokinetic profile confirmed the drug release prolonging potential of MVLS when compared to free drug solution. MVLS were also shown as a biocompatible vehicle, while the cytotoxicity of I3A was observed at CT26WT. In summary, the study proved the concept of using MVLS to overcome I3A's poor solubility, wide tissue distribution and rapid clearance from injection site. The future direction of the project is to administer MVLS-SBE- $\beta$ -CD-I3A into glioma to examine the upregulation of IL13R $\alpha$ 2 and the potential use for CAR-T therapy.

## 2.6 Funding

This work was funded by the Brandmeyer family foundation. MMA acknowledges the Binational Fulbright Commission in Egypt - Fulbright Egyptian Student Program for their financial support during the master's degree.

## 2.7 Acknowledgments

I would like to thank our collaborator Dr. David Akhavan for providing I3A and all the fruitful discussions during the work. I also thank Dr. Chad Groer and Mark Craven for their assistance in the pharmacokinetic study and the *in vitro* studies, respectively. Special thanks to Dr. Justin Douglas for his help with the NMR experiments.

## 2.8 References

- (1) PubChem. Ingenol 3-angelate <https://pubchem.ncbi.nlm.nih.gov/compound/23581946> (accessed 2022 -03 -11).
- (2) Vasas, A.; Redei, D.; Csupor, D.; Molnar, J.; Hohmann, J. Diterpenes from European Euphorbia Species Serving as Prototypes for Natural-Product-Based Drug Discovery. *European Journal of Organic Chemistry* **2012**, 2012 (27), 5115–5130. <https://doi.org/10.1002/ejoc.201200733>.
- (3) Liang, X.; Grue-Sørensen, G.; Petersen, A. K.; Högberg, T. Semisynthesis of Ingenol 3-Angelate (PEP005): Efficient Stereoconservative Angeloylation of Alcohols. *Synlett* **2012**, 23 (18), 2647–2652. <https://doi.org/10.1055/s-0032-1317415>.
- (4) Anderson, L.; Jarratt, M.; Schmieder, G.; Shumack, S.; Katsamas, J.; Welburn, P. Tolerability and Pharmacokinetics of Ingenol Mebutate 0.05% Gel Applied to Treatment Areas up to 100cm<sup>2</sup> on the Forearm(s) of Patients with Actinic Keratosis. *J Clin Aesthet Dermatol* **2014**, 7 (12), 19–29.
- (5) Ali, F. R.; Wlodek, C.; Lear, J. T. The Role of Ingenol Mebutate in the Treatment of Actinic Keratoses. *Dermatol Ther (Heidelb)* **2012**, 2 (1), 8. <https://doi.org/10.1007/s13555-012-0008-4>.
- (6) Dinehart, S. M.; Nelson-Adesokan, P.; Cockerell, C.; Russell, S.; Brown, R. Metastatic Cutaneous Squamous Cell Carcinoma Derived from Actinic Keratosis. *Cancer* **1997**, 79 (5), 920–923. [https://doi.org/10.1002/\(sici\)1097-0142\(19970301\)79:5<920::aid-cncr8>3.0.co;2-f](https://doi.org/10.1002/(sici)1097-0142(19970301)79:5<920::aid-cncr8>3.0.co;2-f).
- (7) Ogbourne, S. M.; Suhrbier, A.; Jones, B.; Cozzi, S.-J.; Boyle, G. M.; Morris, M.; McAlpine, D.; Johns, J.; Scott, T. M.; Sutherland, K. P.; Gardner, J. M.; Le, T. T. T.; Lenarczyk, A.;



- Aylward, J. H.; Parsons, P. G. Antitumor Activity of 3-Ingenyl Angelate: Plasma Membrane and Mitochondrial Disruption and Necrotic Cell Death. *Cancer Res* **2004**, *64* (8), 2833–2839. <https://doi.org/10.1158/0008-5472.can-03-2837>.
- (8) Berman, B. New Developments in the Treatment of Actinic Keratosis: Focus on Ingenol Mebutate Gel. *Clin Cosmet Investig Dermatol* **2012**, *5*, 111–122. <https://doi.org/10.2147/CCID.S28905>.
- (9) Bertelsen, M.; Stahlhut, M.; Grue-Sørensen, G.; Liang, X.; Christensen, G. B.; Skak, K.; Engell, K. M.; Högberg, T. Ingenol Disoxate: A Novel 4-Isioxazolecarboxylate Ester of Ingenol with Improved Properties for Treatment of Actinic Keratosis and Other Non-Melanoma Skin Cancers. *Dermatol Ther (Heidelb)* **2016**, *6* (4), 599–626. <https://doi.org/10.1007/s13555-016-0137-2>.
- (10) Peplin. *A Phase 2 Multi-Centre, Parallel Group, Open Label Study to Evaluate the Safety and Efficacy of PEP005 (Ingenol Mebutate) Gel, 0.05%, When Administered for up to Three Consecutive Days to a Superficial Basal Cell Carcinoma (SBCC) on the Trunk or Extremities*; Clinical trial registration NCT01325688; clinicaltrials.gov, 2016.
- (11) Iannazzone, S. S.; Ingordo, V. Nodular Basal Cell Carcinoma of the Face Successfully Treated with Ingenol Mebutate 0.015% Gel. *Dermatol Pract Concept* **2018**, *8* (2), 129–131. <https://doi.org/10.5826/dpc.0802a12>.
- (12) Le, T. T. T.; Gardner, J.; Hoang-Le, D.; Schmidt, C. W.; MacDonald, K. P.; Lambley, E.; Schroder, W. A.; Ogbourne, S. M.; Suhrbier, A. Immunostimulatory Cancer Chemotherapy Using Local Ingenol-3-Angelate and Synergy with Immunotherapies. *Vaccine* **2009**, *27* (23), 3053–3062. <https://doi.org/10.1016/j.vaccine.2009.03.025>.

- (13) Emmert, S.; Haenssle, H. A.; Zibert, J. R.; Schön, M.; Hald, A.; Hansen, M. H.; Litman, T.; Schön, M. P. Tumor-Preferential Induction of Immune Responses and Epidermal Cell Death in Actinic Keratoses by Ingenol Mebutate. *PLOS ONE* **2016**, *11* (9), e0160096. <https://doi.org/10.1371/journal.pone.0160096>.
- (14) Kedei, N.; Lundberg, D. J.; Toth, A.; Welburn, P.; Garfield, S. H.; Blumberg, P. M. Characterization of the Interaction of Ingenol 3-Angelate with Protein Kinase C. *Cancer Research* **2004**, *64* (9), 3243–3255. <https://doi.org/10.1158/0008-5472.CAN-03-3403>.
- (15) Challacombe, J. M.; Suhrbier, A.; Parsons, P. G.; Jones, B.; Hampson, P.; Kavanagh, D.; Rainger, G. E.; Morris, M.; Lord, J. M.; Le, T. T. T.; Hoang-Le, D.; Ogbourne, S. M. Neutrophils Are a Key Component of the Antitumor Efficacy of Topical Chemotherapy with Ingenol-3-Angelate. *J Immunol* **2006**, *177* (11), 8123–8132. <https://doi.org/10.4049/jimmunol.177.11.8123>.
- (16) Freiburger, S. N.; Cheng, P. F.; Iotzova-Weiss, G.; Neu, J.; Liu, Q.; Dziunycz, P.; Zibert, J. R.; Dummer, R.; Skak, K.; Levesque, M. P.; Hofbauer, G. F. L. Ingenol Mebutate Signals via PKC/MEK/ERK in Keratinocytes and Induces Interleukin Decoy Receptors IL1R2 and IL13RA2. *Molecular Cancer Therapeutics* **2015**, *14* (9), 2132–2142. <https://doi.org/10.1158/1535-7163.MCT-15-0023-T>.
- (17) Brown, C. E.; Aguilar, B.; Starr, R.; Yang, X.; Chang, W.-C.; Weng, L.; Chang, B.; Sarkissian, A.; Brito, A.; Sanchez, J. F.; Ostberg, J. R.; D'Apuzzo, M.; Badie, B.; Barish, M. E.; Forman, S. J. Optimization of IL13R $\alpha$ 2-Targeted Chimeric Antigen Receptor T Cells for Improved Anti-Tumor Efficacy against Glioblastoma. *Mol Ther* **2018**, *26* (1), 31–44. <https://doi.org/10.1016/j.ymthe.2017.10.002>.

- (18) Luo, Y.; Liu, Z.; Zhang, X.; Huang, J.; Yu, X.; Li, J.; Xiong, D.; Sun, X.; Zhong, Z. Effect of a Controlled-Release Drug Delivery System Made of Oleanolic Acid Formulated into Multivesicular Liposomes on Hepatocellular Carcinoma in Vitro and in Vivo. *Int J Nanomedicine* **2016**, *11*, 3111–3129. <https://doi.org/10.2147/IJN.S108445>.
- (19) Shen, Y.; Ji, Y.; Xu, S.; Chen, D. Q.; Tu, J. Multivesicular Liposome Formulations for the Sustained Delivery of Ropivacaine Hydrochloride: Preparation, Characterization, and Pharmacokinetics. *Drug Deliv* **2011**, *18* (5), 361–366. <https://doi.org/10.3109/10717544.2011.557788>.
- (20) Zhang, L.; Ding, L.; Tang, C.; Li, Y.; Yang, L. Liraglutide-Loaded Multivesicular Liposome as a Sustained-Delivery Reduces Blood Glucose in SD Rats with Diabetes. *Drug Deliv* **2016**, *23* (9), 3358–3363. <https://doi.org/10.1080/10717544.2016.1180723>.
- (21) Ye, Q.; Asherman, J.; Stevenson, M.; Brownson, E.; Katre, N. V. DepoFoam™ Technology: A Vehicle for Controlled Delivery of Protein and Peptide Drugs. *Journal of Controlled Release* **2000**, *64* (1), 155–166. [https://doi.org/10.1016/S0168-3659\(99\)00146-7](https://doi.org/10.1016/S0168-3659(99)00146-7).
- (22) Zhang, L.; Zhang, Q.; Wang, X.; Zhang, W.; Lin, C.; Chen, F.; Yang, X.; Pan, W. Drug-in-Cyclodextrin-in-Liposomes: A Novel Drug Delivery System for Flurbiprofen. *International Journal of Pharmaceutics* **2015**, *492* (1), 40–45. <https://doi.org/10.1016/j.ijpharm.2015.07.011>.
- (23) Qiu, J.; Wei, X.; Geng, F.; Liu, R.; Zhang, J.; Xu, Y. Multivesicular Liposome Formulations for the Sustained Delivery of Interferon  $\alpha$ -2b. *Acta Pharmacologica Sinica* **2005**, *26* (11), 1395–1401. <https://doi.org/10.1111/j.1745-7254.2005.00188.x>.

- (24) Katre, N. V.; Asherman, J.; Schaefer, H.; Hora, M. Multivesicular Liposome (DepoFoam) Technology for the Sustained Delivery of Insulin-Like Growth Factor-I (IGF-I). *Journal of Pharmaceutical Sciences* **1998**, 87 (11), 1341–1346. <https://doi.org/10.1021/js980080t>.
- (25) Sadaquat, H.; Akhtar, M. Comparative Effects of  $\beta$ -Cyclodextrin, HP- $\beta$ -Cyclodextrin and SBE7- $\beta$ -Cyclodextrin on the Solubility and Dissolution of Docetaxel via Inclusion Complexation. *J Incl Phenom Macrocycl Chem* **2020**, 96 (3), 333–351. <https://doi.org/10.1007/s10847-020-00977-0>.
- (26) Lu, R.; Groer, C.; Kleindl, P. A.; Moulder, K. R.; Huang, A.; Hunt, J. R.; Cai, S.; Aires, D. J.; Berkland, C.; Forrest, M. L. Formulation and Preclinical Evaluation of a Toll-like Receptor 7/8 Agonist as an Anti-Tumoral Immunomodulator. *J Control Release* **2019**, 306, 165–176. <https://doi.org/10.1016/j.jconrel.2019.06.003>.
- (27) Groer, C.; Zhang, T.; Lu, R.; Cai, S.; Mull, D.; Huang, A.; Forrest, M.; Berkland, C.; Aires, D.; Forrest, M. L. Intratumoral Cancer Chemotherapy with a Carrier-Based Immunogenic Cell-Death Eliciting Platinum (IV) Agent. *Mol. Pharmaceutics* **2020**, 17 (11), 4334–4345. <https://doi.org/10.1021/acs.molpharmaceut.0c00781>.
- (28) Béres, T.; Dragull, K.; Pospíšil, J.; Tarkowská, D.; Dančák, M.; Bíba, O.; Tarkowski, P.; Doležal, K.; Strnad, M. Quantitative Analysis of Ingenol in Euphorbia Species via Validated Isotope Dilution Ultra-High Performance Liquid Chromatography Tandem Mass Spectrometry. *Phytochem Anal* **2018**, 29 (1), 23–29. <https://doi.org/10.1002/pca.2711>.
- (29) Teng, R.-W.; Teng, R.-W.; McManus, D.; Teng, R.-W.; McManus, D.; Aylward, J.; Ogbourne, S.; Armstrong, D.; Mau, S.-L.; Johns, J.; Bacic, A. Biotransformation of Ingenol-3-Angelate in Four Plant Cell Suspension Cultures. *Biocatalysis and Biotransformation* **2009**, 27 (3), 186–194. <https://doi.org/10.1080/10242420902811105>.

- (30) Hampson, P.; Chahal, H.; Khanim, F.; Hayden, R.; Mulder, A.; Assi, L. K.; Bunce, C. M.; Lord, J. M. PEP005, a Selective Small-Molecule Activator of Protein Kinase C, Has Potent Antileukemic Activity Mediated via the Delta Isoform of PKC. *Blood* **2005**, *106* (4), 1362–1368. <https://doi.org/10.1182/blood-2004-10-4117>.
- (31) Gillespie, S. K.; Zhang, X. D.; Hersey, P. Ingenol 3-Angelate Induces Dual Modes of Cell Death and Differentially Regulates Tumor Necrosis Factor–Related Apoptosis-Inducing Ligand–Induced Apoptosis in Melanoma Cells. *Molecular Cancer Therapeutics* **2005**, *3* (12), 1651–1658. <https://doi.org/10.1158/1535-7163.1651.3.12>.
- (32) Furuishi, T.; Sekino, K.; Gunji, M.; Fukuzawa, K.; Nagase, H.; Endo, T.; Ueda, H.; Yonemochi, E. Effect of Sulfobutyl Ether- $\beta$ -Cyclodextrin and Propylene Glycol Alginate on the Solubility of Clozapine. *Pharm Dev Technol* **2019**, *24* (4), 479–486. <https://doi.org/10.1080/10837450.2018.1514521>.
- (33) Briuglia, M.-L.; Rotella, C.; McFarlane, A.; Lamprou, D. A. Influence of Cholesterol on Liposome Stability and on in Vitro Drug Release. *Drug Deliv Transl Res* **2015**, *5* (3), 231–242. <https://doi.org/10.1007/s13346-015-0220-8>.
- (34) Langston, M. V.; Ramprasad, M. P.; Kararli, T. T.; Galluppi, G. R.; Katre, N. V. Modulation of the Sustained Delivery of Myelopoietin (Leridestim) Encapsulated in Multivesicular Liposomes (DepoFoam). *Journal of Controlled Release* **2003**, *89* (1), 87–99. [https://doi.org/10.1016/S0168-3659\(03\)00073-7](https://doi.org/10.1016/S0168-3659(03)00073-7).
- (35) Jain, S. K.; Jain, R. K.; Chourasia, M. K.; Jain, A. K.; Chalasani, K. B.; Soni, V.; Jain, A. Design and Development of Multivesicular Liposomal Depot Delivery System for Controlled Systemic Delivery of Acyclovir Sodium. *AAPS PharmSciTech* **2005**, *6* (1), E35–E41. <https://doi.org/10.1208/pt060108>.

- (36) Wang, T.; Gao, L.; Quan, D. Multivesicular Liposome (MVL) Sustained Delivery of a Novel Synthetic Cationic GnRH Antagonist for Prostate Cancer Treatment. *J Pharm Pharmacol* **2011**, *63* (7), 904–910. <https://doi.org/10.1111/j.2042-7158.2011.01295.x>.
- (37) Ramprasad, M. P.; Amini, A.; Kararli, T.; Katre, N. V. The Sustained Granulopoietic Effect of Progenipoyetin Encapsulated in Multivesicular Liposomes. *International Journal of Pharmaceutics* **2003**, *261* (1), 93–103. [https://doi.org/10.1016/S0378-5173\(03\)00291-6](https://doi.org/10.1016/S0378-5173(03)00291-6).
- (38) Li, N.; Shi, A.; Wang, Q.; Zhang, G. Multivesicular Liposomes for the Sustained Release of Angiotensin I-Converting Enzyme (ACE) Inhibitory Peptides from Peanuts: Design, Characterization, and In Vitro Evaluation. *Molecules* **2019**, *24* (9). <https://doi.org/10.3390/molecules24091746>.
- (39) Azzi, J.; Jraij, A.; Auezova, L.; Fourmentin, S.; Greige-Gerges, H. Novel Findings for Quercetin Encapsulation and Preservation with Cyclodextrins, Liposomes, and Drug-in-Cyclodextrin-in-Liposomes. *Food Hydrocolloids* **2018**, *81*, 328–340. <https://doi.org/10.1016/j.foodhyd.2018.03.006>.
- (40) Abuzar, S. M.; Park, E. J.; Seo, Y.; Lee, J.; Baik, S. H.; Hwang, S.-J. Preparation and Evaluation of Intraperitoneal Long-Acting Oxaliplatin-Loaded Multi-Vesicular Liposomal Depot for Colorectal Cancer Treatment. *Pharmaceutics* **2020**, *12* (8), 736. <https://doi.org/10.3390/pharmaceutics12080736>.
- (41) Vatankhah, M.; Mahboubi, A.; Haeri, A.; Naeini, S. B. M.; Abbasian, Z.; Dadashzadeh, S. Preparation and Optimization of Vancomycin Hydrochloride Encapsulated Multivesicular Liposomes for Sustained Locoregional Delivery. *International Pharmacy Acta* **2021**, *4* (1), 4e6:1-12. <https://doi.org/10.22037/ipa.v4i1.34461>.

- (42) Serova, M.; Ghoul, A.; Benhadji, K. A.; Faivre, S.; Le Tourneau, C.; Cvitkovic, E.; Lokiec, F.; Lord, J.; Ogbourne, S. M.; Calvo, F.; Raymond, E. Effects of Protein Kinase C Modulation by PEP005, a Novel Ingenol Angelate, on Mitogen-Activated Protein Kinase and Phosphatidylinositol 3-Kinase Signaling in Cancer Cells. *Molecular Cancer Therapeutics* **2008**, 7 (4), 915–922. <https://doi.org/10.1158/1535-7163.MCT-07-2060>.
- (43) Applied Biopharmaceutics and Pharmacokinetics, Leon Shargel and Andrew B. C. Yu. - Aarons - 1981 - Journal of Clinical Pharmacy and Therapeutics - Wiley Online Library <https://onlinelibrary.wiley.com/doi/abs/10.1111/j.1365-2710.1981.tb01006.x> (accessed 2022 -03 -24).

**Chapter III: Development of long-acting formulations for Kifunensine  
analogues as potent inhibitors of type I mannosidase and potential agents for  
cancer immunotherapy**



### 3.1 Introduction

The development of cancer cells is accompanied with significant changes in the cellular processes and the surrounding microenvironment. One of these common changes is the alteration in protein glycosylation, which is the enzymatic process of attaching glycans to cell proteins.<sup>1</sup> Protein glycosylation is linked with various essential cell processes such as cell adhesion, cell proliferation, signal transduction and the communication with the immune system.<sup>2,3</sup> Alteration in such a substantial process has been connected to some of the cancer hallmarks such as angiogenesis and metastasis.<sup>4</sup> Also, abnormal glycan biosynthesis can be sensed by the immune system through lectins, glycan-binding proteins, which may trigger immunosuppressive events.<sup>5,6</sup> For instance, the aberrant overexpression of branched N-glycans in the tumor microenvironment was shown to inhibit the production of Interferon gamma (IFN $\gamma$ ) and induce the overexpression of regulatory T cells, which are signs of immune suppression.<sup>7</sup> Therefore, modulating the responsible enzymes for glycan biosynthesis may be utilized as a therapeutic target for improving the anticancer immune response.

An example of these enzymes is the  $\alpha$ -mannosidases, which is the family of enzymes responsible for the biosynthesis, trimming or catabolism of glycoproteins depending on their subcellular location.<sup>8</sup>  $\alpha$ -Mannosidases are classified into two categories according to the type of mannose analogue inhibitors; Type I mannosidase (MAN I) is inhibited by pyranose analogues and can cleave  $\alpha$ -1,2-linked mannose residues. The other category is type II mannosidase (MAN II), which is inhibited by furanose analogues and can hydrolyze  $\alpha$ -1,2-,  $\alpha$ -1,3-, and  $\alpha$ -1,6-linked mannose residues.<sup>9</sup> Kifunensine (KIF) is a potent inhibitor of MAN I that results in an overexpression of high mannose N-glycans instead of branched N-glycans, which has been shown to enhance tumor immune recognition.<sup>7</sup> However, attempts to develop more potent KIF analogues

were impeded by the need to find a lectin-based assay that is capable of specifically detecting high mannose N-glycans. Fortunately, Kurhade et al. (2021) recently developed a functionalized cyanovirin-N (CVN) lectin that exhibits high specificity for high mannose N-glycans. CVN lectin was capable of distinguishing the glycans resulting from the inhibition of MAN I over MAN II, and also to evaluate the activity of various MAN I inhibitors.<sup>10</sup> Therefore, CVN lectin has paved the way for the development and evaluation of more potent KIF analogues. In addition, the relationship between the overexpression of high mannose N-glycans, resulting from MAN I inhibition, and the antitumor immune response can now be investigated.

KIF is a small molecule compound that exhibits a high water solubility (Log P: -3.7), but also exhibits a low cellular permeability resulting in low activity.<sup>11</sup> It was demonstrated that increasing the lipophilicity of the KIF structure could enhance its cellular permeability, and thus improve the efficacy to a nanomolar range. The hydroxyl groups of KIF could be conjugated with lipophilic esters that could impart better permeability to KIF analogues.<sup>10</sup> Intracellular ester-cleaving enzymes would then convert KIF prodrugs back to the active form of KIF to perform its activity. Nevertheless, such lipophilic KIF analogues limit the formulation options for administering them into cells due to the poor resulting solubility. Thus, a formulation strategy with high affinity to lipophilic compounds is needed to deliver the KIF prodrugs into cells. Long-acting depot formulations with lipophilic affinity present a potential vehicle for administration of KIF analogues, as they can prolong the retention of therapeutic doses, decrease administration frequency, and enhance patient compliance.<sup>12</sup>

In this chapter, we hypothesize that overexpression of high mannose N-glycans by KIF analogues may lead to a positive antitumor immune recognition. To do that, two potential KIF analogues were investigated for their influence on the high mannose N-glycans production. The

first KIF analogue is JDW-II-002 (LogP: 3.56) with four chains of valerate branched from the four hydroxyl groups of KIF, while the other analogue is JDW-II-008 (LogP: 5.23) with four chains of hexanoate as shown in **Figure 1**. In this study, we developed a long-acting formulation that can retain the lipophilic analogues and extend their release profile. Afterwards, the optimized formulation was administered to an immunocompetent mouse cancer model to examine the antitumor activity and to detect immune cells in extracted tumors. The results showed a promising influence of the tested KIF analogues on the expression of high mannose N-glycans and a marginal improvement of the antitumor immune recognition.

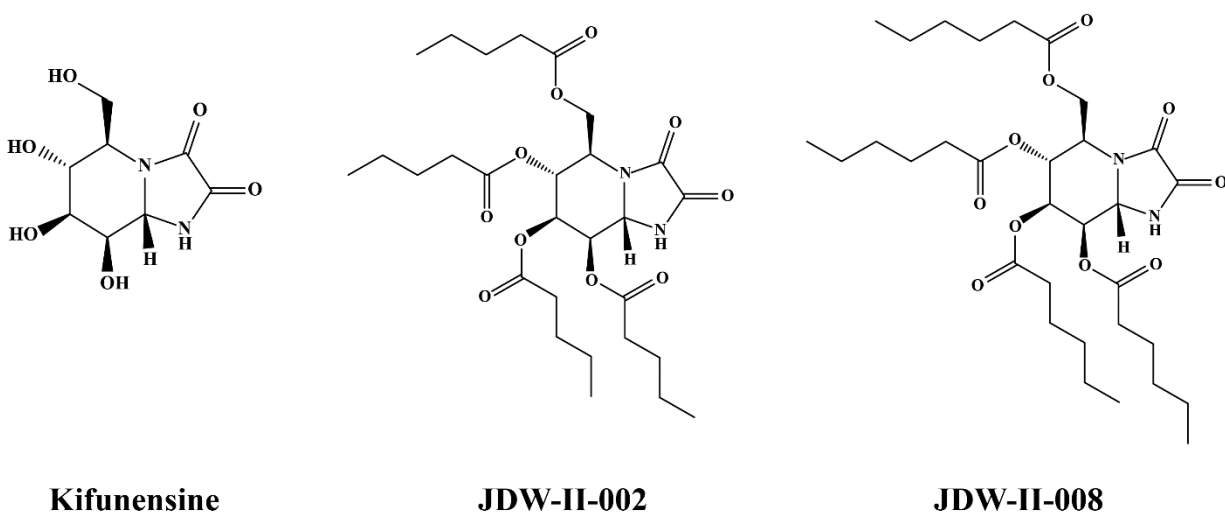


**Figure 1** The chemical structure of parent Kifunensine (KIF) and the lipophilic KIF analogues (JDW-II-002 and JDW-II-008).

## 3.2 Materials and Methods

### 3.2.1 Materials

Kifunensine analogues (JDW-II-002 & JDW-II-008) were provided from our collaborator Dr. Mark Farrell (Department of Medicinal Chemistry, The University of Kansas). Sodium

hyaluronan (32 kDa) was brought from Lifecore Biomedical (Chaska, MN). (+)- $\alpha$ -tocopherol, ethyl oleate (Pharmacopoeia Europaea grade) and hexane were purchased from Sigma Aldrich (St. Louis, MO). HPLC grade solvents were purchased from Fisher Scientific (Hampton, NH). Ethanol was obtained from Decon Labs (King of Prussia, PA). Float-A-Lyzer<sup>®</sup>G2 dialysis devices (MWCO: 3.5-5 kDa) were obtained from Repligen (Boston, MA). Hydrophilic PTFE Syringe Filters (0.22  $\mu$ m Pore Size) were purchased from Premium Vials (Tullytown, PA). Alexa Fluor<sup>®</sup> staining antibodies were purchased from BioLegend (San Diego, CA).

### 3.2.2 HPLC method

The chromatographic analysis of KIF analogues was performed by high performance liquid chromatography (HPLC) (LC-2010C HT, Shimadzu). The highest absorbance wavelength ( $\lambda_{\text{max}}$ ) of KIF analogues was determined by running a sample of these compounds dissolved in H<sub>2</sub>O/acetonitrile (ACN) (1:1, v/v) on a photodiode array (PDA) detector, which demonstrated that the absorbance maximum of the compounds occurs at 221 nm. Given the high lipophilicity of these analogues, a reverse-phase C18 column (Phenomenex, 5  $\mu$ m particle size, 4.6  $\times$  150 mm) was used to separate the analogues from their injection solution. The mobile phases were 0.1% acetic acid in water (A) and 0.1% acetic acid in ACN (B). All mobile phases were degassed by bath sonication for 20 min and filtered using a 0.45- $\mu$ m filter under vacuum. Gradient elution was employed at a flow rate of 1 ml/min and oven temperature of 25 °C. The time program started with 35% (B) to 65% (B) at 5 min and maintained at that gradient until 8.75 min, then re-equilibrated to 35% (B) at 13 min. The injection volume was 20  $\mu$ l, and the KIF analogues were detected using the PDA at 221 nm.

The validation of the HPLC method was performed by testing the method specificity, linearity, sensitivity, and extraction recovery for the KIF analogues. Specificity and extraction

recovery were examined by running each analogue alone and then with the subsequently developed formulation. Linearity was tested using least squares regression analysis. Sensitivity was evaluated by the limit of detection (LOD) and limit of quantification (LOQ), which were calculated for both analogues using the formulas:

$$\text{LOD} = \frac{3.3\sigma}{S}, \text{ LOQ} = \frac{10\sigma}{S}$$

where  $\sigma$  is the standard deviation of the response and  $S$  is the slope of the calibration curve.<sup>13</sup>

### 3.2.3 Determination of oil-buffer distribution coefficient

The oil-buffer distribution coefficient ( $D_{oil-PBS}$ ) of the KIF analogues was determined by the shake-flask method.<sup>14,15</sup> Ethyl oleate (EO) oil was used as the oil vehicle, whereas the buffer phase was phosphate buffer saline adjusted to a pH of 7.4 (PBS 7.4). For each KIF analogue, 0.3 mg was dissolved in 1 ml of the oil vehicle, then brought into contact with 5 ml of PBS 7.4 under moderate shaking for 48 h at 37 °C, allowing the drugs to attain equilibrium between the oil and buffer phases. Afterwards, the mixture was kept still for an additional 24 h without shaking to ensure phase separation. Then, a 10  $\mu$ l aliquot of the oil phase was sampled to determine the concentration of the KIF analogues initially and after equilibrium using the HPLC method. The distribution coefficient was calculated as following:

$$D_{oil-PBS} = \frac{[Solute]_{oil-equ}}{[Solute]_{aqu-equ}}$$

Where  $[Solute]_{oil-equ}$  expresses the equilibrium concentration of the solute within the oil phase and  $[Solute]_{aqu-equ}$  expresses the equilibrium concentration of the solute within the aqueous phase as calculated from the difference between the initial and equilibrium concentration of the solute in the oil phase.

### **3.2.4 Development of formulation strategy**

The main desired characteristic of the formulation is to sustain the release of the KIF analogues; thus, the therapeutic concentration of the drug can be maintained for a convenient time period and the mice do not have to be frequently injected. Besides, the formulation should be able to retain lipophilic compounds, since the KIF analogues exhibit logPs of 3.56 for JDW-II-002 and 5.23 for JDW-II-008. It was also preferred that the formulation of choice to be simple and straightforward, thus maximizing the reproducibility of the results. To satisfy these characteristics, two long-acting formulations were examined that can dissolve the lipophilic analogues and obtain a sustained and reproducible release profile.

#### **3.2.4.1 Hyaluronan- $\alpha$ -Tocopherol (HA-Toco) conjugate**

##### **3.2.4.1.1 Loading KIF analogues into HA-Toco**

Hyaluronan (HA) is a natural polymer that is extensively utilized for drug delivery applications due to its outstanding properties such as high water solubility, biocompatibility, and biodegradability. The modification of HA with hydrophobic moieties was shown to provide an amphiphilic nature to the resulting conjugates, which can self-assemble in water to solubilize lipophilic drugs through non-covalent interactions forming a nanosuspension depot upon injection. An example of these hydrophobic moieties is (+)- $\alpha$ -Tocopherol (Toco), also called vitamin E, which was conjugated to HA through multi-step reactions as reported recently by our lab.<sup>16</sup> The HA-Toco conjugate was kindly provided by a colleague in Dr. Forrest's lab. The loading of KIF analogues into HA-Toco conjugates was performed following a modified emulsification-solvent evaporation method. Briefly, KIF analogues were dissolved in 2 ml of ethanol (1 mg/ml), then 3 ml of HA-Toco in water (1 mg/ml) was added dropwise over 30 min while stirring at room temperature. Then, the mixture was dried using a CentriVap concentrator (Labconco, KS) for 3 h

and reconstituted by adding 2 ml of PBS overnight forming a nanosuspension depot of HA-Toco loaded with KIF analogues.

#### **3.2.4.1.2 Determination of entrapment efficiency**

A 50 µl sample of the HA-Toco nanosuspension was diluted with acetone (1:50 v/v) and bath sonicated for 15 min to liberate the KIF analogues. Afterwards, the solution was centrifuged at  $13,000 \times g$  for 10 min, and the supernatant was filtered through a 0.22-µm syringe filter. The content of each analogue was determined using HPLC (LC-2010C HT, Shimadzu) with PDA detection at 221 nm ( $\lambda_{\text{max}}$  of KIF analogues) and a reverse-phase C18 column (Phenomenex, 5 µm particle size,  $4.6 \times 150$  mm) maintained at 25 °C. The entrapment efficiency (EE%) was calculated as follows:

$$EE\% = \frac{C_{\text{liberated}} \times Vol}{W_{\text{initial}}} \times 100$$

Where  $C_{\text{liberated}}$  expresses the concentration of KIF analogues liberated from HA-Toco which is calculated from a calibration curve,  $Vol$  expresses the sample volume and  $W_{\text{initial}}$  expresses the total amount of drug.

#### **3.2.4.1.3 *In vitro* release profile**

The donor phase consisted of 1 ml of the loaded HA-Toco nanosuspension in PBS 7.4 (0.2 mg/ml) in a Float-A-Lyzer®G2 dialysis cell (MWCO: 3.5-5 kDa). The acceptor phase consisted of 500 ml of PBS 7.4 maintained at 37 °C and stirring at 150 rpm. The sample aliquots (10 µl) were taken from inside the dialysis cell, given the high lipophilicity of the analogues and the limit of detection of the HPLC method. At each time point, the solution in the dialysis cell was weighted before and after taking the sampling aliquot (10 µl) to determine the percent drug remaining

through a density calculation as reported before.<sup>16</sup> The aliquot samples were diluted with acetone, sonicated, centrifuged, filtered, and analyzed by HPLC to determine drug content.

#### 3.2.4.2 Ethyl oleate vehicle

##### **3.2.4.2.1 Loading KIF analogues into ethyl oleate (EO)**

Acetone solutions of the KIF analogues (250  $\mu$ l, 1 mg/ml) were dried using nitrogen gas flushing. Then, 1 ml of EO was added (250  $\mu$ g/ml) to reconstitute the dried analogues, and that was sonicated for 15 min to ensure that all drug residues went into solution.

##### **3.2.4.2.2 Drug quantification**

The quantification of KIF analogues dissolved into EO was determined following a modified solvent extraction method.<sup>17,18</sup> KIF analogues-loaded EO solution (10  $\mu$ l) was diluted with 90  $\mu$ l of 90% EtOH in H<sub>2</sub>O. Then, 100  $\mu$ l of hexane was added to 90% EtOH solution. The mixture was well vortexed and centrifuged at  $13,000 \times g$  for 15 min, resulting in two immiscible phases. The upper layer was hexane which should probably contain most of the EO because of their affinity to each other. While the lower layer was the 90% EtOH which should probably contain the KIF analogues. Afterwards, the hexane layer containing the EO was carefully removed, and another 100  $\mu$ l of the mobile phase H<sub>2</sub>O/ACN (1:1, v/v) was added. Before analyzing on the HPLC, the samples were filtered using 0.22- $\mu$ m hydrophilic PTFE membranes (Premium Vials) to prevent the EO micro droplets from passing through. The same HPLC method described above was used to determine the drug content. The extraction recovery of the KIF analogues from EO was determined by measuring low (5  $\mu$ g/ml), medium (25  $\mu$ g/ml) and high concentrations (100  $\mu$ g/ml) of JDW-II-002 on the same day and on a different day.



### 3.2.4.2.3 *In vitro* release profile

The release of the KIF analogues from EO was measured by immersing a Float-A-Lyzer<sup>®</sup>G2 dialysis cell (MWCO: 3.5-5 kDa) containing 1 ml of EO (250 µg/ml) in a large release sink of 500 ml PBS 7.4 at 37 °C, stirred at 200 rpm. The purpose of the setup is to increase the interface area between the oil and the release medium and to maintain the sink conditions.<sup>19,20</sup> At predetermined points, an aliquot of 10 µl was removed from the oil phase for analysis of the percent drug remaining as follows:

$$\% \text{ drug remaining} = \frac{C_t \times V_t}{W_{\text{initial}}} \times 100$$

Where  $C_t$  is the measured concentration of drug at each time point,  $V_t$  is the remaining EO volume, and  $W_{\text{initial}}$  is the initial amount of drug content.

### 3.2.5 *In vivo* antitumor activity

#### 3.2.5.1 Study design

The *in vivo* study was performed using BALB/c immunocompetent mice at the University of Kansas (KU) Animal Care Unit under an approved protocol from the KU Institutional Animal Care and Use Committee (IACUC), Animal Use Statement Number: 168-04. Male and female BALB/c mice were used in the study. No differences found between both sexes; thus, the results of both sexes are represented in the same group. A Heterotopic flank tumor was induced by subcutaneous (s.c.) introduction of  $1 \times 10^5$  cells of the colon carcinoma cell line CT26WT resuspended in 100 µl of PBS/Matrigel, which helps hold the cells within the injection site and improves the formation of uniform tumors.<sup>21</sup>

### 3.2.5.2 Tumor model for efficacy

The tumor injections were monitored regularly until they reached a measurable size (4-6 days postinoculation). Then, 15 mice were randomly divided into five treatment groups (n = 3) and intratumoral (i.t.) injections began under isoflurane anesthesia. The injection volume was 50  $\mu$ l of EO oil containing either no drug, 300  $\mu$ g or 400  $\mu$ g of analogue drug. Injections into the right flank of the tumor mice were repeated every three days to maintain the therapeutic dose of KIF analogues. At each injection day, the body weight, body condition score (BCS) and ambulation were recorded. The tumor size was calculated by measuring the length (L) and width (W) of the tumor via a caliper, and inserting their values into the following equation:

$$\text{Tumor volume (mm}^3\text{)} = 0.52 \times L \times W^2$$

The longest dimension is termed the length (L), whereas a perpendicular smaller dimension is the width (W).

### **3.2.6 Immunohistochemistry analysis for immune markers**

In all treatment groups, whenever tumor size reached 1800 mm<sup>3</sup>, the maximum allowable size according to IACUC protocol, the mouse was euthanized within 24 h. Tumors were then excised, dissected, and immersed in optimal cutting temperature (OCT) medium (Fischer Scientific) prior to freezing into liquid N<sub>2</sub> and storing at -80 °C. Afterwards, the frozen tumor tissue was cryosectioned into 8  $\mu$ m slices using a Shandon Cryotome FSE (Thermo Scientific) and placed on a positively charged microscope slide (Walter Products). Then, each tissue slice was prepared for a staining protocol as described before.<sup>22</sup> At first, the tissue slices were fixed with 10% formalin and rinsed with PBS in triplicate for 5 min each. The tumor section was then isolated from the rest of the slide with a solvent resistant pen, and a blocking buffer of 10% goat serum in PBS was added to avoid non-specific binding of the applied antibodies. Then, primary antibodies

(diluted in 5% goat serum) were added to the tissue slices and left in a dark space overnight at 4 °C. The nuclei of each slice were stained with Hoechst 33342 (10 µg/mL) in PBS, then a microscope cover glass was mounted on each tissue section using SouthernBiotech™ Fluoromount-G medium and left overnight at 4 °C. The whole area of slices was imaged using an Olympus IX-81 inverted epifluorescence microscope at 10× magnification, and the images were combined together using the montage feature of the SlideBook 6 software. The list of applied antibodies is summarized at **Table 1**.

Set #	Fluorophores	Marker
Set 1	CVN Lectin - Alexa Fluor® 594	High mannose N-glycans
	Alexa Fluor® 647 anti-FoxP3	T-regulatory cells
Set 2	Alexa Fluor® 488 anti-CD8a	Cytotoxic T cells
	Alexa Fluor® 594 anti-CD11b	Macrophages
	Alexa Fluor® 594 anti-CD11c	Dendritic cells
Set 3	APC anti-mouse CD3 488	Pan T cells
	APC anti-mouse NK1.1 645	Natural killer T cells

**Table 1** Summary of the fluorophore sets that were applied to the tumor sections treated with either EO vehicle, JDW-II-002 or JDW-II-008. Each set contains only one fluorophore at each instrument channel.

### 3.2.7 Statistical analysis

All experiments were conducted in triplicate and the data are expressed as the mean  $\pm$  standard deviation. Significant differences were examined by student t-test or one-way analysis of variance (ANOVA) followed by Tukey's post hoc tests ( $*p \leq 0.05$ ,  $**p \leq 0.01$ ,  $***p \leq 0.001$  and  $****p \leq 0.0001$ ) using GraphPad Prism Software version 8. Comparisons are considered not statistically significant (ns) when  $p > 0.05$ .

### 3.3 Results

#### 3.3.1 HPLC method validation

The developed HPLC method was validated by examining its specificity, linearity, sensitivity, and extraction recovery for the KIF analogues. In regard to specificity, the developed HPLC method was able to detect both KIF analogues with no interfering or overlapping peaks. The chromatograms of the KIF analogues dissolved in 1:1 ACN to water solution demonstrated a retention time of ~ 9 min for JDW-II-002, whereas JDW-II-008 showed a retention time of ~ 10 min. For linearity, a calibration curve of six standard concentration levels from 5 – 100 µg/ml was plotted and tested using least squares regression analysis. A linear equation between the peak area (A) of each analogue and its corresponding concentration (C) was obtained as following:  $A = (16320 \times C) + 40417$  for JDW-II-002 ( $R^2 = 0.9960$ ), while  $A = (16017 \times C) - 10376$  for JDW-II-008 ( $R^2 = 0.9985$ ). In terms of the sensitivity, LOD was found to be 5.43 µg/ml and LOQ of 16.44 µg/ml for JDW-II-002, Whereas JDW-II-008 showed LOD of 3.33 µg/ml and LOQ of 10.09 µg/ml. These results suggest a good predictive calibration curve and based on it; the unknown distribution and release samples can be quantitated.

#### 3.3.2 Determination of oil-buffer distribution coefficient

The oil-buffer distribution coefficient denotes the partitioning nature of a chemical species between the oil and aqueous buffer phases at equilibrium. The purpose of measuring the oil-buffer distribution coefficient is to help estimate the solubility of the KIF analogues in both the oil and PBS 7.4. With the aid of the shake-flask method, both analogues were examined for the distribution coefficient between EO and PBS 7.4 at 37 °C. An aliquot from the oil phase was diluted with isopropanol (1:20, v/v) and quantitated using the aforementioned HPLC method. As shown in **Figure 2**, the distribution coefficient of JDW-II-002 was measured to be  $19.99 \pm 0.54$ , while for

JDW-II-008, it is  $37.95 \pm 2.76$ . Both values suggest a high affinity for the KIF analogues to the oil phase over PBS 7.4, which is expected due to their highly lipophilic nature. In addition, JDW-II-008 demonstrated higher affinity to the EO oil than JDW-II-002, which could be ascribed to its higher lipophilicity (LogP: 5.23). Therefore, KIF analogues could be considered as poorly soluble in aqueous solutions, which requires the development of a formulation strategy that could dissolve such lipophilic compounds.

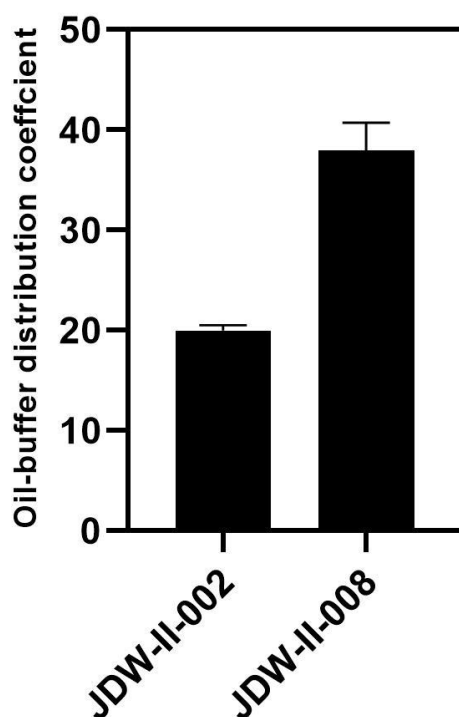


**Figure 2** Oil-buffer distribution coefficient of JDW-II-002 and JDW-II-008 in EO oil. (Plotted values are the mean  $\pm$  SD, n = 3).

### 3.3.3 Development of formulation strategy

#### 3.3.3.1 HA-Toco vehicle

The loading of KIF analogues into HA-Toco, via the solvent-emulsification method, resulted in a light grey nanosuspension with no observed precipitates. This observation suggests that most of the KIF analogues were brought into the suspension. To confirm that observation, the

EE% of each analogue nanosuspension was measured directly by recovering the drug molecules from HA-Toco using acetone dilution and ultrasonication. The EE% of JDW-II-002 is 84.2%, while the EE% of JDW-II-008 is 97.5% in HA-Toco. These high EE% suggest that most of the drug molecules were brought into solution. Also, the higher EE% of JDW-II-008, compared to the less lipophilic JDW-II-002, suggests that lipophilic character of the molecule enhances its interaction with HA-Toco.

The *in vitro* release study of the KIF analogues was carried out in PBS 7.4 maintained at 37 °C. The release of the KIF analogues was indirectly determined by measuring the percent drug remaining inside the release cartridge. The rationale of indirect measurement is the poor aqueous solubility of the KIF analogues, which requires a large sink volume that would substantially dilute the release samples below the detection limit of the HPLC method. The release samples were stored at 4 °C until the end of the study, then all of them were acetone treated and analyzed by HPLC. As shown in **Figure 3**, the release of JDW-II-002 showed a half-life of 3.1 h, while JDW-II-008 showed a higher half-life of 10.4 h. Looking into the release profiles of both KIF analogues demonstrates that HA-Toco prolonged the release of JDW-II-008 relatively more than JDW-II-002, which is consistent with more hydrophobic interactions occurring between JDW-II-008 and HA-Toco as observed earlier. However, the release of JDW-II-008 (10.4 h) from HA-Toco was not extended enough for the *in vivo* study, as it would still require at least two daily injections. HA-Toco formulation was able to solubilize the KIF analogues but did not sufficiently sustain their release. Thus, a better long-acting formulation was still needed.

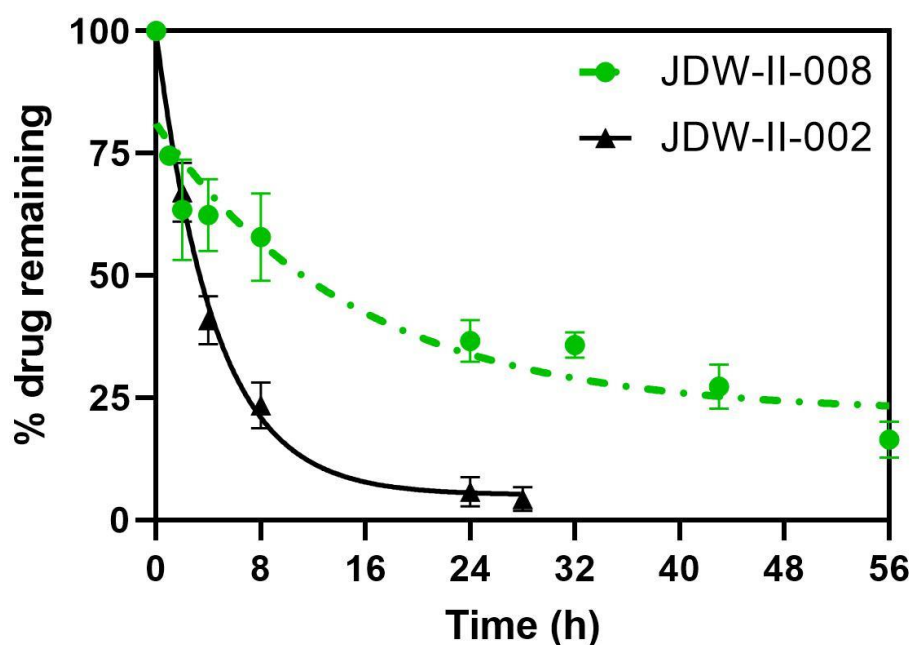


**Figure 3** Release profile of JDW-II-002 and JDW-II-008 from HA-Toco. The half-life was estimated by first order decay least squares fit using GraphPad Prism 8, JDW-II-002 = 3.1 h and JDW-II-008 = 10.4 h (% drug remaining values are the mean  $\pm$  SD, n = 3).

### 3.3.3.2 Ethyl oleate vehicle

Oil depot formulations exhibit several advantages when it comes to the loading of lipophilic compounds ( $\text{LogP} > 3$ ). These advantages include the simple manufacturing and the high affinity to lipophilic compounds, which potentiates the sustained release of the loaded compounds. Therefore, ethyl oleate (EO) vehicle was chosen for the loading of KIF analogues. The amount of KIF analogues that was added to EO was completely loaded given the high oil-buffer distribution coefficient and the low added concentration of KIF analogues (0.25 mg/ml) compared to its EO saturation solubility ( $> 9$  mg/ml). The extraction of KIF analogues from EO was accomplished by a solvent extraction method.<sup>17,18</sup> Drug compounds were liberated from EO using 90% EtOH dilution, then hexane was added to extract the EO and subsequently removed.



Afterwards, the sample was further diluted with another 100  $\mu$ l of the mobile phase H<sub>2</sub>O/ACN (1:1, v/v) (final dilution factor is 20x) and filtered to ensure the removal of EO microdroplets. Running the samples on HPLC demonstrated the efficiency of the extraction method as reflected by the appearance of the drug peaks on the chromatogram without any interfering peaks (**Figure 4a**). The extraction recovery for JDW-II-002 from EO following intraday and inter-day measurements showed good accuracy as summarized in **Table 2**.

For the release study, a Float-A-Lyzer<sup>®</sup>G2 dialysis cell (MWCO: 3.5-5 kDa) was employed to contain the drug-loaded EO vehicles, as it can maximize the interface area between the oil solution and the release media. The results showed the EO could effectively sustain the release of JDW-II-002 with a half-life of 162 h, which is about 7 days (**Figure 4b**). This release profile satisfies the study requirements as it is able to prolong the analogues release, reduce mouse injection frequency, and it is reproducible. Therefore, we relied on EO as a formulation strategy for loading KIF analogues and applying it into the *in vivo* mouse model.

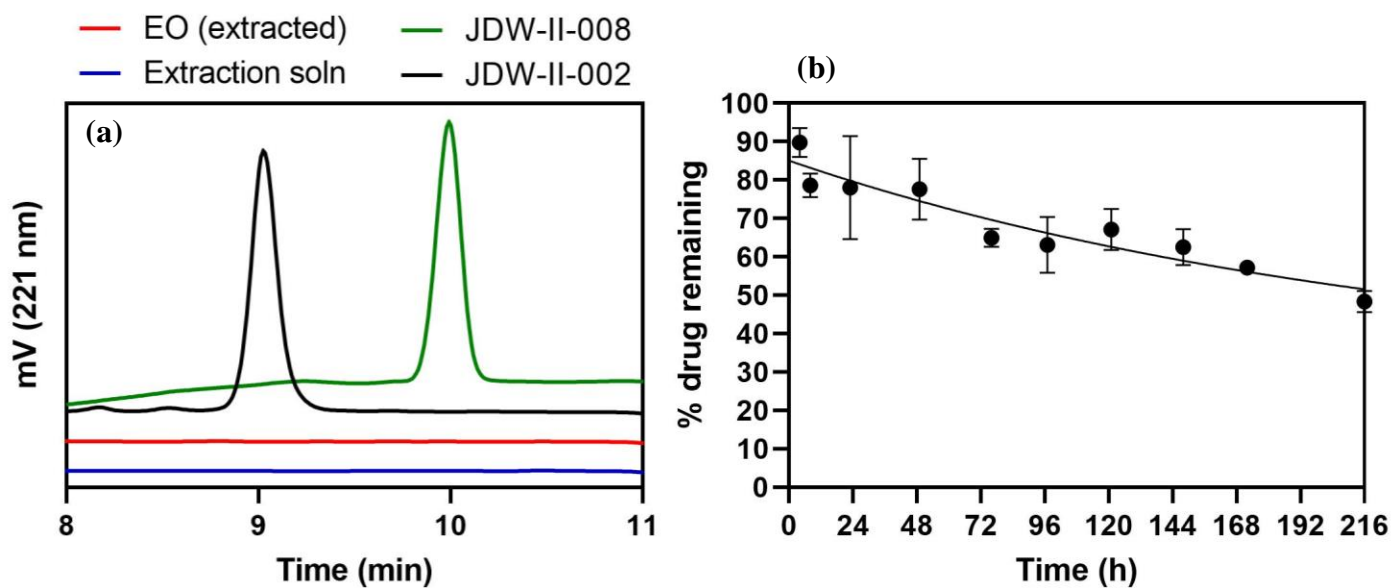


**Figure 4** (a) HPLC chromatogram of the EO-extracted JDW-II-002, JDW-II-008 (50  $\mu\text{g/ml}$ ) and their extraction solution (b) Release profile of JDW-II-002 from EO oil vehicle. The half-life was estimated by first order decay least squares fit using GraphPad Prism 8, JDW-II-002 = 162 h (% drug remaining values are the mean  $\pm$  SD,  $n = 3$ ).

Theoretical concentration (µg/ml)	Intraday measurement		Inter-day measurement	
	Measured concentration (µg/ml)	Accuracy (%)	Measured concentration (µg/ml)	Accuracy (%)
5	5.16	103.27	5.95	119.06
25	24.30	97.22	24.27	97.07
100	99.46	99.46	105.38	105.38

**Table 2** The extraction recovery of JDW-II-002 from EO vehicle following intraday and inter-day measurements at 5, 25, and 100 µg/ml. (Values are the mean ± SD, n = 3)

### 3.3.4 *In vivo* antitumor activity

The KIF analogues loaded in the EO formulation was administered to BALB/c immunocompetent mice to examine the efficacy of JDW-II-002 and JDW-II-008 at doses of 300 µg or 400 µg. Animals were dosed every three days for a total of five doses. The tumor growth study showed that JDW-II-008 treatments delayed the tumor growth compared to the vehicle, while JDW-II-002 treatments did not show any suppression in the tumor growth (**Figure 5**). JDW-II-008 300 µg was the most effective treatment to retard the tumor growth with average size  $1002 \pm 353 \text{ mm}^3$  as compared to the vehicle  $1444 \pm 599 \text{ mm}^3$  at day 21 representing 31% tumor growth inhibition. JDW-II-008 400 µg showed a smaller tumor inhibition with an average size of  $1277 \pm 536 \text{ mm}^3$ , representing 12% tumor growth inhibition. Nonetheless, the suppression of the tumor growth by JDW-II-008 was not statistically significant, which may be attributed to the low animal

number per group. To help understand this observation, high mannose N-glycans and the tumor cell infiltration were investigated with immunohistochemistry.

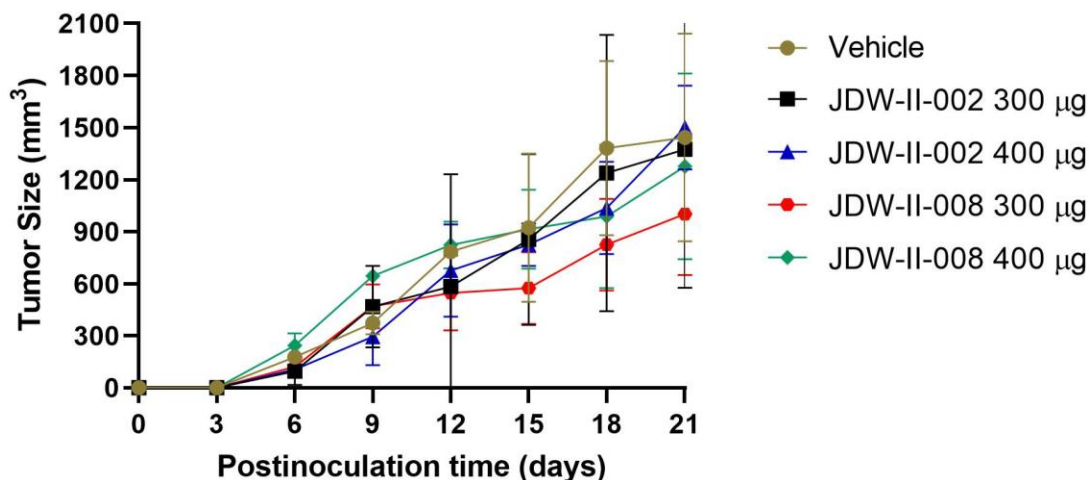


**Figure 5** Tumor growth monitoring following the treatment with JDW-II-002 and JDW-II-008 with either 300 µg or 400 µg dose (n = 3/group) of CT26WT mouse model, euthanasia occurs when one of the tumors reached 1800 mm<sup>3</sup>. Tumor length and width (mm) were measured every 3 days starting at day 6 postinoculation. (Values are the mean ± SD, n = 3)

### 3.3.5 Immunohistochemistry analysis for immune markers

Upon the end of the *in vivo* study, tumors were excised and stored in OCT medium at −80 °C for further analysis. Each tumor was cryosectioned into 8 µm slices that were later stained with multiple immune markers (**Table 1**). The screening of the immune cells was partially supported by reported studies on the parent KIF and the MAN II inhibitor, swainsonine, where such compounds were able to recruit immune cells.<sup>5,7</sup> These markers can recognize cytotoxic T cells, dendritic cells, natural killer T cells, macrophages, and regulatory T cells. Percent area stained of treated sample to the whole tumor slice was used to indicate the relative recruitment of the corresponding immune cells.

At first, we tested the effect of KIF analogues on increasing the high mannose N-glycans using CVN lectin that can specifically bind to the glycans resulting from the inhibition of MAN I inhibitors such as our KIF analogues. As shown in **Figure 6a**, All KIF analogues were able to significantly increase the expression of high mannose N-glycans over the control with percent staining area over 90%. Also, none of the KIF analogues was significantly better than the others in increasing the glycans levels. These results suggest that KIF analogues, both doses, were able to effectively permeate the cells, which supports our hypothesis that lipophilicity enhanced the cell uptake of the KIF analogues. In **Figure 6b**, CD8a was investigated as a marker for the cytotoxic T cells. There is a gradual increase in T cell recruitment from JDW-II-002 400  $\mu\text{g}$  ( $0.03 \pm 0.01$  %), to JDW-II-008 300  $\mu\text{g}$  ( $0.05 \pm 0.04$  %), and 400  $\mu\text{g}$  ( $0.20 \pm 0.17$  %). However, the only statistically significant increase was witnessed with JDW-II-008 400  $\mu\text{g}$  with  $0.20 \pm 0.17$  % compared to  $0.008 \pm 0.009$  % for the control. In **Figure 6c**, FoxP3 was examined as a marker for T-regulatory cells. Although all treatments failed to have a significant change than the vehicle, it was observed that JDW-II-008 treatments exhibit lower T-regulatory cells infiltration; JDW-II-008 300  $\mu\text{g}$  showed  $2.5 \pm 1.6$  % and JDW-II-008 400  $\mu\text{g}$  showed  $4.1 \pm 3.5$  % compared to  $13.2 \pm 15.8$  % for the vehicle. The increase in the T-cell infiltration and the decrease in the T-regulatory cells both occurred only with JDW-II-008 treatment groups, which is consistent with the results of the tumor growth inhibition study. Such observation may explain the reason why JDW-II-008 groups showed more tumor growth inhibition than JDW-II-002, since the first was able to recruit T cells and downregulate the T-regulatory cells. Such events accompanying the JDW-II-008 treatments may be assigned to an antitumor immune response that led to the inhibition of the tumor growth.

We also investigated other immune markers (**Figure 6 d-g**), but none of them showed any significant difference than the control or even any obvious relationship. This could be assigned to

the absence of these immune cells at the tumor site, but we cannot be confident at this point due to the relatively low number of mice per treatment group. **Figures 7-9** demonstrate the fluorescence intensity of the examined fluorophores, which could be used qualitatively to infer relationships among the treatment groups. Quantitative analysis of these figures using ImageJ software led to the graphs shown at **Figure 6**.

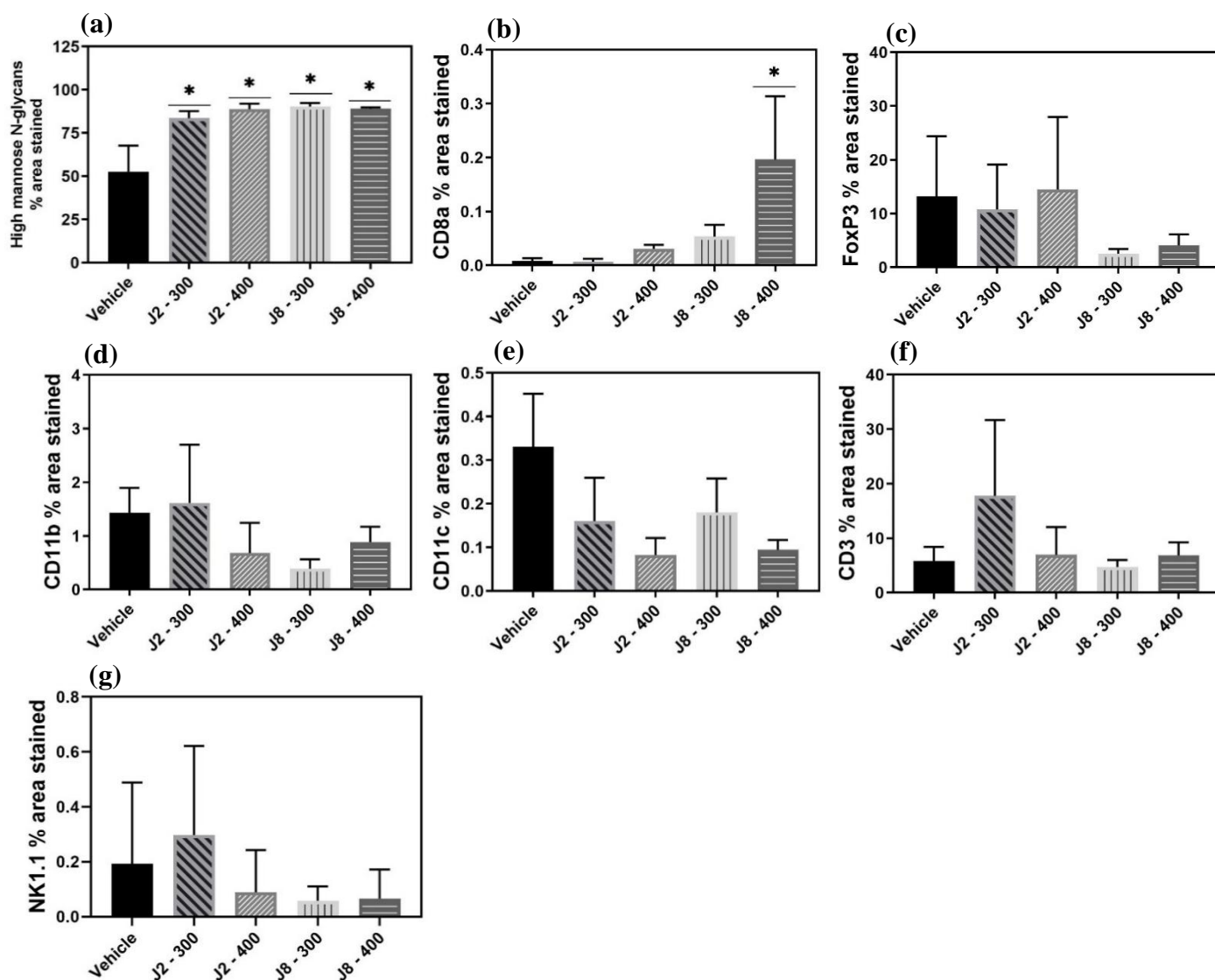


**Figure 6** Immunohistochemistry analysis of CT26WT mouse model treated with intratumoral KIF analogues (JDW-II-002 and JDW-II-008) with either 300  $\mu$ g or 400  $\mu$ g dose presented as % area stained with respect to the whole tumor area estimated from the DAPI staining. All graphs have been processed with ImageJ to calculate the area resulting from each fluorophore (\*  $P \leq 0.05$ ,  $n = 3$ ).

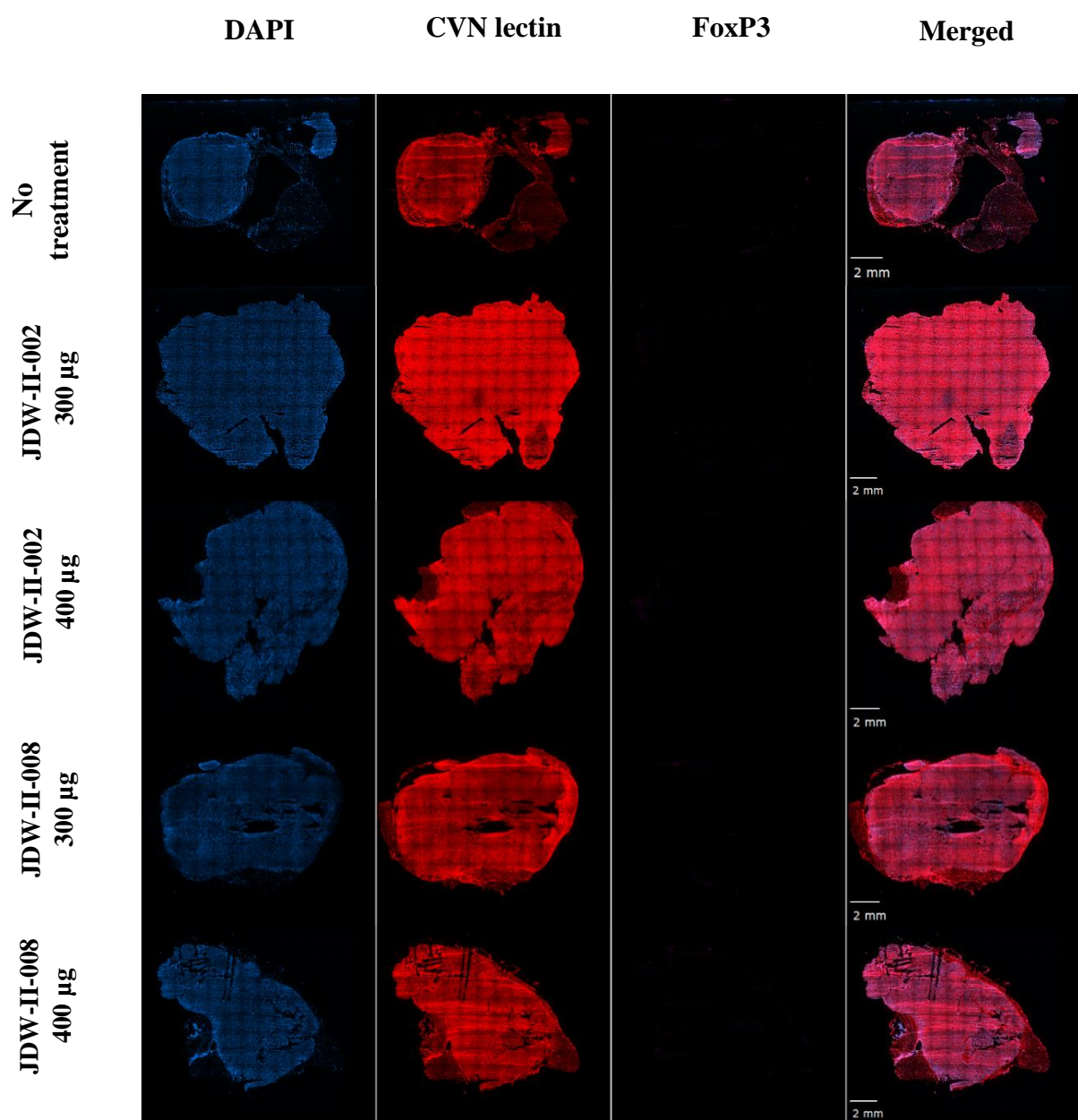


**Figure 7** Immunohistochemistry analysis of CT26WT mouse model treated with intratumoral KIF analogues (JDW-II-002 and JDW-II-008) with either 300 µg or 400 µg dose, and stained with DAPI, CVN lectin and FoxP3. Scale bar is 2 mm and all images adjusted equally.



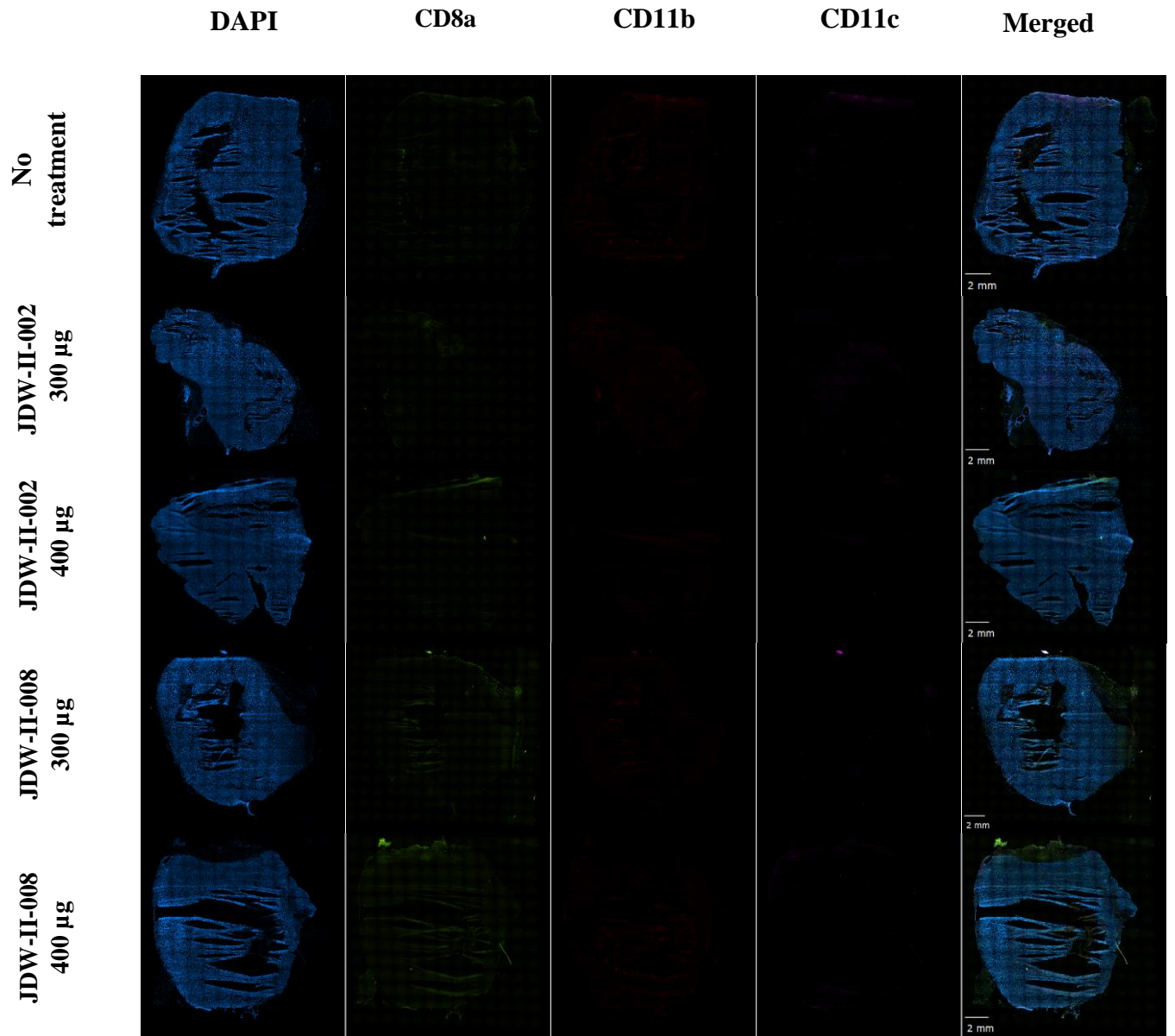


**Figure 8** Immunohistochemistry analysis of CT26WT mouse model treated with intratumoral KIF analogues (JDW-II-002 and JDW-II-008) with either 300 µg or 400 µg dose, and stained with DAPI, CD8a, CD11b and CD11c. Scale bar is 2 mm and all images adjusted equally.

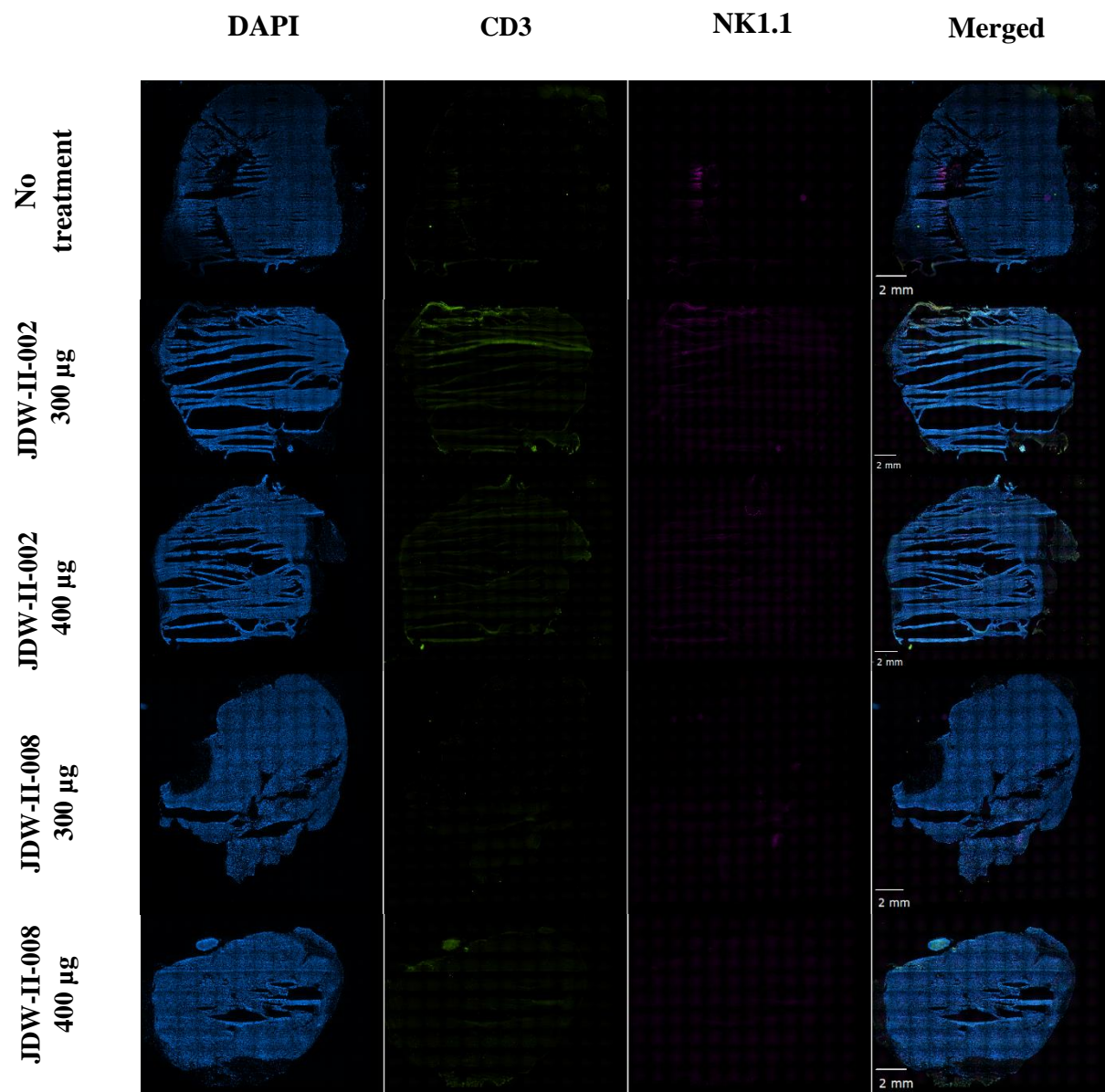


**Figure 9** Immunohistochemistry analysis of CT26WT mouse model treated with intratumoral KIF analogues with either 300 µg or 400 µg dose, and stained with DAPI, CD3 and NK1.1. Scale bar is 2 mm and all images adjusted equally.

### 3.4 Discussion

Changes in glycan signature are one of the events commonly accompanying the cancer cell development. Lectins of immune cells can detect alterations to glycan signature and trigger certain immune responses. For example, the predominance of branched glycans over high mannose ones was showed to contribute into immunosuppressive events such as overexpression of T-regulatory cells.<sup>7</sup> Thus, we hypothesized if such process was prevented by an overexpressing the high mannose N-glycans, it may lead to better immune cell infiltration and tumor growth suppression. We utilized the MAN I inhibitor KIF and modified its structure to be more lipophilic in order to improve the cell uptake and potentiate the overexpression of high mannose N-glycans. However, since increasing the lipophilicity of KIF analogues substantially reduced its aqueous solubility, we needed to develop a long-acting formulation that can solubilize such compounds and sustain their release over appropriate time spans. Afterwards, we examined the therapeutic efficiency of the developed formulation on an immunocompetent *in vivo* tumor model and investigated the immune cell infiltration using immunohistochemistry marker analysis.

KIF analogues showed high oil-buffer distribution coefficients, which suggest its high affinity for oily/lipophilic formulations. Accordingly, formulations that are able to solubilize lipophilic compounds were pursued. At first, HA-Toco was examined as it was reported previously to solubilize lipophilic prodrugs such as cisplatin and resiquimod prodrugs.<sup>16,22</sup> Complexation of KIF analogues with HA-Toco resulted in a nanosuspension with high EE%. JDW-II-008 demonstrated higher EE% (97.5%.) than JDW-II-002 (84.2%.), which may be connected to the more lipophilic character of JDW-II-008 and thus the incidence of more hydrophobic interactions. The *in vitro* release study showed more extended release of JDW-II-008 ( $t_{1/2} = 10.4$  h) than JDW-II-002 ( $t_{1/2} = 3.1$  h), which agrees with the hydrophobic interaction interpretation. This conclusion

aligns with Lu et al. (2019) when they observed that a resiquimod prodrug ( $c\text{LogP} = 14.9$ ) complexed with HA-Toco demonstrated higher EE% than the parent resiquimod ( $c\text{LogP} = 1.84$ ).<sup>16</sup> However, this release profile was not sufficient for the study requirements, which requires a longer acting formulation so as not to inject the mice multiple times per day. In contrast, EO showed better performance as a long-acting formulation, in which the half-life of JDW-II-002 was around 162 h. The ability of EO to extend the release more than HA-toco may be attributed to EO's higher lipophilicity. Upon injection, EO droplets may be visualized as flattened spheres in the injection site, which limits the surface area and requires longer time for partitioning into tissue fluids. On the other hand, HA-Toco nanosuspension exhibits relatively higher affinity to the aqueous tissue fluids compared to EO, due to the highly-water soluble HA chains, conferring more surface area and allowing better drug partition. EO exhibits a low viscosity (5.1 mPa.s) as compared to other common oil vehicles (30 – 40 mPa.s), which facilitates handling and injection process.<sup>17</sup> low viscosity was also reported to influence the *in vivo* release performance, since it could easily spread into the injection site, relatively increase the interface between oil vehicle and tissue fluids, allow more partitioning opportunities, and thus may encounter faster release than observed *in vitro*, compared to more viscous oil vehicles.<sup>19</sup> Thus, EO was chosen as the formulation to be applied to the *in vivo* efficacy model.

KIF analogues loaded into EO formulation were applied to a heterotopic flank CT26WT tumor model, which is frequently used for immunotherapy studies.<sup>23</sup> The injection dose was determined on the basis of giving the maximum tolerable amount, since the increase in KIF analogues concentration was showed to increase the expression of the high mannose N-glycans.<sup>10</sup> To determine such tolerable dose, an *in vitro* CT26WT viability study was conducted by the collaborating group that indicated the safety of the KIF on the cell lines up to 100  $\mu\text{M}$  (data are

not shown). We also conducted a pilot study with four mice (two as treatment and two as control) to examine the applicability of the *in vitro* study on the mice model, which did not show any side effects on body condition or ambulation. The selection of three days as an injection period was based on the difference occurring in the *in vivo* release behavior compared to the *in vitro* study as discussed earlier. Thus, a three-day dose interval of either 300 µg or 400 µg was examined to test the efficiency of KIF analogues. JDW-II-008 treatment demonstrated better tumor growth inhibition than JDW-II-002. Silva et al. (2020) showed a similar tumor growth suppression when they applied the parent KIF intratumorally on the MC38 murine tumor model.<sup>7</sup> However, they treated the cells with KIF for 48 h before inoculating the cells into the mice, which may bias the results they obtained. In contrast, we did not treat the cells before inoculation, but we observed a similar tumor suppression especially with JDW-II-008 300 µg.

The immunohistochemistry analysis showed that each KIF analogue treatment was able to significantly overexpress the high mannose N-glycans compared to the control group, while none of them was significantly better than one another. For the immune cell infiltration, only JDW-II-008 400 µg demonstrated a significant increase in CD8a over the control. Also, FoxP3 analysis showed a noticeable decrease, although non-statistically significant, in the fluorescence intensity for JDW-II-008 compared to the control group. The expression of CD8a is evidence for the recruitment of cytotoxic T lymphocytes, while FoxP3 is a marker of T-regulatory cells. Both findings were only witnessed with JDW-II-008 treatments, which is probably connected to the observed delay in the tumor growth. Based on the immunohistochemistry analysis, we interpret the efficiency of JDW-II-008 was due to upregulation of cytotoxic T lymphocytes and downregulation of T-regulatory cells, which represent features of antitumor immune response.<sup>24,25</sup> Silva et al. (2020) was able to correlate the tumor growth suppression with the downregulation of

T-regulatory cells in colorectal cancer.<sup>7</sup> Therefore, the *in vivo* study points out that JDW-II-008 could delay the tumor growth, and significantly increase expression of high mannose N-glycans. However, our study should be further expanded in order to gain more confidence in whether JDW-II-008 can significantly recruit immune cells to the tumor site.

### **3.5 Conclusion**

The loading of KIF analogues were examined on HA-Toco and EO vehicles. HA-Toco was able to solubilize the KIF analogues but did not sufficiently sustain their release for the *in vivo* study, as it would still require at least two daily mice injections. While EO showed a desirable sustained release profile that reduced the frequency of administration to a dose every three days. Thus, EO loaded with KIF analogues were used to examine the therapeutic efficiency using an immunocompetent mice model of colon cancer. The *in vivo* study results indicated a delay in the tumor growth with JDW-II-008 treatments, in particular. The immunohistochemistry analysis demonstrated an overexpression of high mannose N-glycans with all KIF treatments. However, only JDW-II-008 was able to recruit cytotoxic T lymphocytes and downregulate T-regulatory cells. Although the study requires further investigation, it could be considered as a proof-of-concept for the potential of KIF analogues to overexpress the high mannose N-glycans and trigger antitumor immune responses.

### **3.6 Funding**

This work was funded by the Brandmeyer family foundation. MMA acknowledges the Binational Fulbright Commission in Egypt - Fulbright Egyptian Student Program for their financial support during the master's degree.

### 3.7 Acknowledgments

I would like to thank our collaborator Dr. Mark Farrell for providing the KIF analogues, the fluorophores and for all the informative discussions along the duration of the work. I also thank Dr. Chad Groer and Aric Huang for their assistance in the *in vivo* study and the subsequent immune marker analysis.

### 3.8 References

- (1) Stowell, S. R.; Ju, T.; Cummings, R. D. Protein Glycosylation in Cancer. *Annual Review of Pathology: Mechanisms of Disease* **2015**, *10* (1), 473–510. <https://doi.org/10.1146/annurev-pathol-012414-040438>.
- (2) Mereiter, S.; Balmaña, M.; Campos, D.; Gomes, J.; Reis, C. A. Glycosylation in the Era of Cancer-Targeted Therapy: Where Are We Heading? *Cancer Cell* **2019**, *36* (1), 6–16. <https://doi.org/10.1016/j.ccell.2019.06.006>.
- (3) Ohtsubo, K.; Marth, J. D. Glycosylation in Cellular Mechanisms of Health and Disease. *Cell* **2006**, *126* (5), 855–867. <https://doi.org/10.1016/j.cell.2006.08.019>.
- (4) Pinho, S. S.; Reis, C. A. Glycosylation in Cancer: Mechanisms and Clinical Implications. *Nat Rev Cancer* **2015**, *15* (9), 540–555. <https://doi.org/10.1038/nrc3982>.
- (5) Shi, S.; Gu, S.; Han, T.; Zhang, W.; Huang, L.; Li, Z.; Pan, D.; Fu, J.; Ge, J.; Brown, M.; Zhang, P.; Jiang, P.; Wucherpfennig, K. W.; Liu, X. S. Inhibition of MAN2A1 Enhances the Immune Response to Anti-PD-L1 in Human Tumors. *Clin Cancer Res* **2020**, *26* (22), 5990–6002. <https://doi.org/10.1158/1078-0432.CCR-20-0778>.
- (6) van Kooyk, Y.; Rabinovich, G. A. Protein-Glycan Interactions in the Control of Innate and Adaptive Immune Responses. *Nat Immunol* **2008**, *9* (6), 593–601. <https://doi.org/10.1038/ni.f.203>.
- (7) Silva, M. C.; Fernandes, Â.; Oliveira, M.; Resende, C.; Correia, A.; de-Freitas-Junior, J. C.; Lavelle, A.; Andrade-da-Costa, J.; Leander, M.; Xavier-Ferreira, H.; Bessa, J.; Pereira, C.; Henrique, R. M.; Carneiro, F.; Dinis-Ribeiro, M.; Marcos-Pinto, R.; Lima, M.; Lepenies, B.; Sokol, H.; Machado, J. C.; Vilanova, M.; Pinho, S. S. Glycans as Immune Checkpoints: Removal of Branched N-Glycans Enhances Immune Recognition Preventing Cancer



- Progression. *Cancer Immunol Res* **2020**, 8 (11), 1407–1425. <https://doi.org/10.1158/2326-6066.CIR-20-0264>.
- (8) Beccari, T. Lysosomal Alpha-Mannosidase and Alpha-Mannosidosis. *Front Biosci* **2017**, 22 (1), 157–167. <https://doi.org/10.2741/4478>.
  - (9) Shah, N.; Kuntz, D. A.; Rose, D. R. Comparison of Kifunensine and 1-Deoxymannojirimycin Binding to Class I and II  $\alpha$ -Mannosidases Demonstrates Different Saccharide Distortions in Inverting and Retaining Catalytic Mechanisms,. *Biochemistry* **2003**, 42 (47), 13812–13816. <https://doi.org/10.1021/bi034742r>.
  - (10) Kurhade, S. E.; Weiner, J. D.; Gao, F. P.; Farrell, M. P. Functionalized High Mannose-Specific Lectins for the Discovery of Type I Mannosidase Inhibitors. *Angewandte Chemie* **2021**, 133 (22), 12421–12426. <https://doi.org/10.1002/ange.202101249>.
  - (11) Kifunensine <https://go.drugbank.com/drugs/DB02742> (accessed 2022 -03 -02).
  - (12) O'Brien, M. N.; Jiang, W.; Wang, Y.; Loffredo, D. M. Challenges and Opportunities in the Development of Complex Generic Long-Acting Injectable Drug Products. *Journal of Controlled Release* **2021**, 336, 144–158. <https://doi.org/10.1016/j.jconrel.2021.06.017>.
  - (13) Pardhi, V.; Pant, G.; Flora, S. J. S. RP-HPLC Method Development and Validation for Bedaquiline Fumarate to Evaluate Its Forced Degradation Behaviour and Stability in Official Dissolution Media. *Future Journal of Pharmaceutical Sciences* **2020**, 6 (1), 42. <https://doi.org/10.1186/s43094-020-00061-x>.
  - (14) Larsen, S. W.; Østergaard, J.; Friberg-Johansen, H.; Jessen, M. N. B.; Larsen, C. In Vitro Assessment of Drug Release Rates from Oil Depot Formulations Intended for Intra-Articular Administration. *European Journal of Pharmaceutical Sciences* **2006**, 29 (5), 348–354. <https://doi.org/10.1016/j.ejps.2006.07.002>.

- (15) Larsen, S. W.; Jessen, M. N. B.; Østergaard, J.; Larsen, C. Assessment of Drug Release from Oil Depot Formulations Using an In Vitro Model—Potential Applicability in Accelerated Release Testing. *Drug Development and Industrial Pharmacy* **2008**, *34* (3), 297–304. <https://doi.org/10.1080/03639040701655994>.
- (16) Lu, R.; Groer, C.; Kleindl, P. A.; Moulder, K. R.; Huang, A.; Hunt, J. R.; Cai, S.; Aires, D. J.; Berkland, C.; Forrest, M. L. Formulation and Preclinical Evaluation of a Toll-like Receptor 7/8 Agonist as an Anti-Tumoral Immunomodulator. *J Control Release* **2019**, *306*, 165–176. <https://doi.org/10.1016/j.jconrel.2019.06.003>.
- (17) Abcha, I.; Souilem, S.; Neves, M. A.; Wang, Z.; Nefatti, M.; Isoda, H.; Nakajima, M. Ethyl Oleate Food-Grade O/W Emulsions Loaded with Apigenin: Insights to Their Formulation Characteristics and Physico-Chemical Stability. *Food Research International* **2019**, *116*, 953–962. <https://doi.org/10.1016/j.foodres.2018.09.032>.
- (18) Treesuwan, W.; Ichikawa, S.; Wang, Z.; Neves, M. A.; Uemura, K.; Nakajima, M.; Kobayashi, I. Formulation and Storage Stability of Baicalein-Loaded Oil-in-Water Emulsions. *European Journal of Lipid Science and Technology* **2013**, *115* (10), 1115–1122. <https://doi.org/10.1002/ejlt.201300125>.
- (19) Weng Larsen, S.; Larsen, C. Critical Factors Influencing the In Vivo Performance of Long-Acting Lipophilic Solutions—Impact on In Vitro Release Method Design. *AAPS J* **2009**, *11* (4), 762–770. <https://doi.org/10.1208/s12248-009-9153-9>.
- (20) Larsen, S. W.; Frost, A. B.; Østergaard, J.; Marcher, H.; Larsen, C. On the Mechanism of Drug Release from Oil Suspensions in Vitro Using Local Anesthetics as Model Drug Compounds. *European Journal of Pharmaceutical Sciences* **2008**, *34* (1), 37–44. <https://doi.org/10.1016/j.ejps.2008.02.005>.

- (21) Badea, M. A.; Balas, M.; Hermenean, A.; Ciceu, A.; Herman, H.; Ionita, D.; Dinischiotu, A. Influence of Matrigel on Single- and Multiple-Spheroid Cultures in Breast Cancer Research. *SLAS DISCOVERY: Advancing the Science of Drug Discovery* **2019**, *24* (5), 563–578. <https://doi.org/10.1177/2472555219834698>.
- (22) Groer, C.; Zhang, T.; Lu, R.; Cai, S.; Mull, D.; Huang, A.; Forrest, M.; Berkland, C.; Aires, D.; Forrest, M. L. Intratumoral Cancer Chemotherapy with a Carrier-Based Immunogenic Cell-Death Eliciting Platinum (IV) Agent. *Mol. Pharmaceutics* **2020**, *17* (11), 4334–4345. <https://doi.org/10.1021/acs.molpharmaceut.0c00781>.
- (23) Castle, J. C.; Loewer, M.; Boegel, S.; de Graaf, J.; Bender, C.; Tadmor, A. D.; Boisguerin, V.; Bukur, T.; Sorn, P.; Paret, C.; Diken, M.; Kreiter, S.; Türeci, Ö.; Sahin, U. Immunomic, Genomic and Transcriptomic Characterization of CT26 Colorectal Carcinoma. *BMC Genomics* **2014**, *15* (1), 190. <https://doi.org/10.1186/1471-2164-15-190>.
- (24) Bailly, C.; Thuru, X.; Quesnel, B. Combined Cytotoxic Chemotherapy and Immunotherapy of Cancer: Modern Times. *NAR Cancer* **2020**, *2* (1), zcaa002. <https://doi.org/10.1093/narcan/zcaa002>.
- (25) Li, C.-H.; Kuo, W.-H.; Chang, W.-C.; Huang, S.-C.; Chang, K.-J.; Sheu, B.-C. Activation of Regulatory T Cells Instigates Functional Down-Regulation of Cytotoxic T Lymphocytes in Human Breast Cancer. *Immunol Res* **2011**, *51* (1), 71. <https://doi.org/10.1007/s12026-011-8242-x>.

## **Chapter IV: Hyaluronic acid carrier-based photodynamic therapy for head and neck squamous cell carcinoma**

## 4.1 Introduction

Head and neck squamous cell carcinomas (HNSCC) and epithelial carcinomas constitute the majority of malignancies in the head and neck region. Tumors in the head and neck region can arise from a variety of tissues in the upper aerodigestive tract, which includes the oral cavity, nasal cavity, pharynx, larynx, sinuses, and other related soft tissues and bones.<sup>1</sup> Within head and neck carcinomas, 90% of malignancies are HNSCC with over 900,000 new cases in 2020, ranking as the sixth common cancer worldwide.<sup>2,3</sup> HNSCC is a heterogeneous disease originating from the most superficial tissues throughout the head and neck area. Early diagnosis and treatment of local HNSCC improves quality of life as well as disease prognosis.<sup>4,5</sup> Currently, locally advanced HNSCC carries five year survival rate of approximately 80%, while locally advanced disease with lymph node involvement has a 60% survival.<sup>6</sup> Although earlier detection can improve outcomes dramatically, there remains a need for more effective and less invasive treatments for patients with early locally advanced tumors.

Conventional treatments for localized cancers include surgery, radiation, and systemic chemotherapy, all of which have significant limitations. To preserve critical tissues of the head and neck, surgical margins are generally not aggressive; however, malignant cells beyond the surgical field often cause recurrence.<sup>7</sup> Furthermore, while tissue-sparing chemotherapy and radiotherapy can help preserve speech and swallowing in locally advanced disease, they achieve only modest improvements in survival.<sup>8,9</sup> Even when used conservatively, these conventional treatments can cause long-term vascular damage and irreversible injury in key surrounding tissues, including oral mucosa, muscle, and bone. Furthermore, dose-limiting oral toxicity can compromise therapeutic efficacy via dose reduction, regimen delay, or insufficient treatment.<sup>10</sup> Thus, there is a

need for effective, safe, and minimally invasive treatment modalities for managing locally advanced HNSCC.

Photodynamic therapy (PDT) uses a photosensitizer (PS) that is activated by a focused optical energy to destroy abnormal tissues. PDT is a promising modality for HNSCC due to its non-invasive nature, the minimum cytotoxicity of unirradiated PSs, and the likelihood to be repeated without cumulative side effects.<sup>11–13</sup> Pyropheophorbide-a (PPa) is a second-generation PS used for PDT, following Photofrin<sup>®</sup> which was FDA approved in 1995 for esophageal cancer and Barrett's esophagus.<sup>14</sup> Second-generation PSs were developed to overcome the shortcomings of the first-generation PSs such as low tissue penetration, skin sensitivity and limited tumor selectivity.<sup>15</sup> Among them, PPa represents one of the potential second-generation PSs as it confers deep tissue penetration because of a red-shifted absorbance maximum (670 nm), reduced skin photosensitivity, and minimal dark toxicity.<sup>16</sup> In addition, PPa is more stable than its parent pheophorbides due to the removal of the ester group.<sup>17</sup> However, PPa exhibits a wide tissue distribution and poor water solubility given its highly lipophilic nature.<sup>18</sup>

To address these issues, various nanocarriers have been reported to enhance PS accumulation in malignant tissues, including polymeric nanoparticles, micelles, liposomes, and polymeric conjugates.<sup>19–23</sup> Hyaluronic acid (HA) may be a potential solution since it could act as a PS carrier, a water solubility enhancer, and a targeting moiety to localize PS into the local lymph nodes. HA is a highly-soluble natural polysaccharide, composed of D-glucuronic acid and D-N-acetylglucosamine.<sup>24–26</sup> HA can enhance the selectivity of PS as it exhibits natural tropism for CD44,<sup>27</sup> hyaluronan-mediated motility receptor (RHAMM),<sup>28,29</sup> and lymphatic vessel endothelial receptor-1 (LYVE-1),<sup>30</sup> which are overexpressed in metastatic cancer cells.<sup>28</sup> In addition to the

outstanding biophysical properties of HA, PDT can decrease the metastatic potential of cancer cells.<sup>31</sup>

In this chapter, a novel PPa-hyaluronan conjugate was developed to enhance the PPa aqueous solubility, tumor selectivity and overall efficacy. The conjugation of PPa to HA was conducted via an adipic acid dihydrazide (ADH) linker utilizing the presence of a carboxyl group on PPa terminal. The PPa-hyaluronan conjugate was injected subcutaneously in NU/NU mice bearing human HNSCC MDA-1986 tumors, while employing a diode laser and near-infrared (NIR) imaging to activate PPa and monitor its distribution, respectively. The conjugation of PPa to HA dramatically improved the water solubility and the tumor selectivity while maintaining the photoactivity of PPa. These results demonstrate that HA-ADH-PPa could be useful for in vivo locoregional photodynamic therapy of HNSCC.

## **4.2 Materials and Methods**

### **4.2.1 Materials**

Sodium hyaluronan (35 kDa) was purchased from Lifecore Biomedical (Chaska, MN). PPa was purchased from Frontier Scientific (Logan, Utah). 1-[Bis(dimethylamino)methylene]-1H-1,2,3-triazolo[4,5-b] pyridinium 3-oxid hexafluorophosphate (HATU) was purchased from Chem-Impex International, Inc. (Wood Dale, IL). N-(3-Dimethylaminopropyl)-N'-ethylcarbodiimide hydrochloride (EDC•HCl), adipic acid dihydrazide (ADH) and TWEEN® 80 were purchased from Sigma-Aldrich Co. (St. Louis, MO). Other chemicals and organic solvents, *N*, *N*-Diisopropylethylamine (DIPEA), *N*, *N*-dimethylformamide (DMF) and dimethyl sulfoxide (DMSO), and cell culture supplies were purchased from Fisher Scientific (Pittsburgh, PA). Dulbecco's Modified Eagle's Medium (DMEM) was purchased from Lonza (Allendale, NJ). LysoTracker® Blue DND-22 (ex/em, 373/422 nm), 4', 6-Diamidino-2-Phenylindole (DAPI,

ex/em, 358/461 nm) and Singlet Oxygen Sensor Green (SOSG) were purchased from Life Technologies™ (Grand Island, NY). The MDA-1986 human oral squamous carcinoma cell line was kindly provided by Dr. Jeffery Myers (The University of Texas, M.D. Anderson Cancer Center, Houston, TX). Double distilled water (ddH<sub>2</sub>O) was used for preparing all of the aqueous solutions.

#### 4.2.2 Synthesis and Characterization of HA-ADH-PPa

The conjugation of PPa to HA was accomplished using an ADH linker. Briefly, 100 mg of sodium hyaluronate was dissolved in 20 ml of ddH<sub>2</sub>O, followed by addition of ADH (200 mg) and EDC•HCl (24 mg). The pH of the mixture was adjusted to *ca.* 5.0 using 1-N HCl, and the mixture was stirred at room temperature (*ca.* 20 °C) for 20 min to form the HA-ADH intermediates. The resulting solution was neutralized using 1-N NaOH, dialyzed against ddH<sub>2</sub>O (Thermo Scientific™, SnakeSkin™ Dialysis Tubing, MWCO 3,500 Da) for 24 h and lyophilized (Labconco 2.5 Plus FreeZone, Kansas City, MO). To synthesize the HA-ADH-PPa, the carboxyl terminal of PPa (5 mg, 9.35 μmol) was pre-activated with HATU (14.2 mg, 37.3 μmol) and DIPEA (13 μl, 74.6 μmol) in 4 ml of DMF for 0.5 h prior to the addition of the HA-ADH (100 mg, 25 mg/ml) aqueous solution (**Figure 1**). The reaction was allowed to proceed overnight protected from light at room temperature. The unreacted PPa was removed by precipitation in excess ddH<sub>2</sub>O, and the supernatant was further dialyzed (MWCO 3,500 Da) against 25% (v/v) ethanol-water mixture for 48 h in the dark.



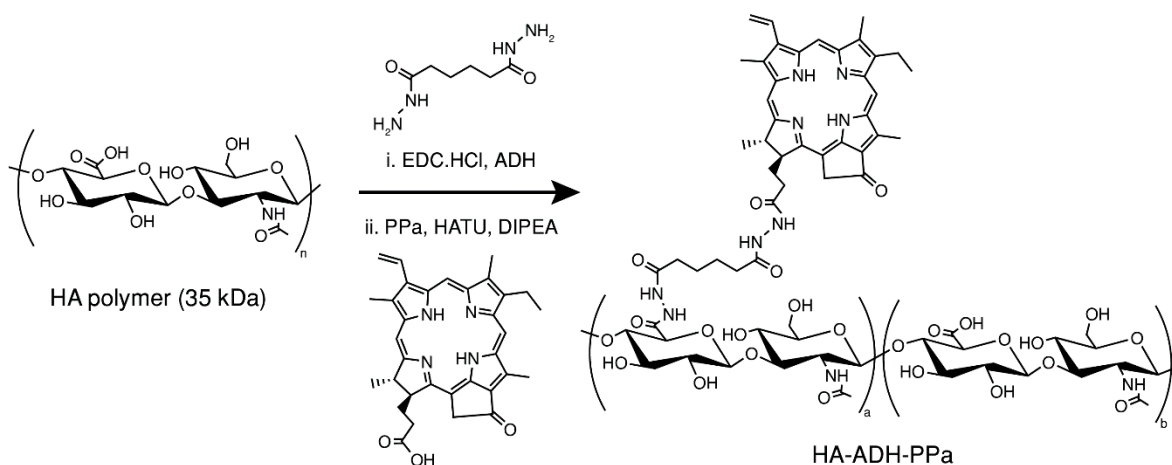


**Figure 1** Synthesis scheme of HA-ADH-PPa

The synthesis of HA-ADH-PPa was confirmed using  $^1\text{H}$ -NMR spectroscopy (AVIIIHD 400 MHz, Bruker, MA). Solutions of HA-ADH (10 mg/ml in  $\text{D}_2\text{O}$ ) and HA-ADH-PPa (10 mg/ml in 6:1 (v/v)  $\text{DMSO-d}_6$ :  $\text{D}_2\text{O}$ ) were prepared. The chemical shifts of the structure and the degree of PPa conjugation were obtained from the resulting  $^1\text{H}$ -NMR spectrum. Spectrofluorometry (ex/em 400 nm/680 nm, Shimadzu RF-5301PC Spectrofluorophotometer, Columbia, MD) and UV/Vis spectrophotometry (675 nm, Molecular Devices SpectraMax Plus, Sunnyvale, CA) were also used to determine the degree of conjugation. A solution of HA-ADH-PPa (1 mg/ml) was prepared in 1:5:94 (v/v/v) TWEEN® 80/DMSO/ddH $_2\text{O}$  (solution A). Calibration solutions (2.5, 5, 8, 10 and 20  $\mu\text{g/ml}$ ) were prepared by dissolving PPa in solution A with HA-ADH (1 mg/ml). Gel permeation chromatography (GPC) was used to confirm the conjugation by comparing the elution time of HA-ADH and HA-ADH-PPa. GPC analysis was performed on a Shodex HQ-806 M column thermostated at 40  $^\circ\text{C}$  with 5-mM ammonium acetate (pH 5) as the mobile phase at a flow rate of 0.8 ml/min, and peaks were detected using an evaporative light scattering detector (ELSD, 70  $^\circ\text{C}$ ) and an UV/Vis detector at 600 nm. To observe the morphology of HA-ADH-PPa nano-

conjugates, 10  $\mu$ l of the ethanolic dispersion of the particles was spotted on a negatively charged Holey carbon supported copper grid (Sigma Aldrich) to facilitate the spreading of the sample on the grid, and high-resolution transmission electron microscopy (TEM) (FEI Tecnai F20 XT Field Emission TEM) images were recorded at an accelerating voltage of 200 kV.

#### **4.2.3 Singlet Oxygen Generation**

The generation of singlet oxygen from PPa or HA-ADH-PPa was quantitatively evaluated using SOSG. Photoirradiation was performed using a diode laser (HL6750MG, Thorlabs, Newton, NJ; power: 50 mW; wavelength: 685 nm), which was driven by a laser diode current controller (LDC220, Thorlabs, Newton, NJ). The light beam illuminated directly above the cell holder of the fluorescent spectrometer with a power density of 7.5 mW/cm<sup>2</sup>. Free PPa (10  $\mu$ M) or HA-ADH-PPa (10  $\mu$ M of PPa) with 10-nmol/ml SOSG in 400  $\mu$ l of 1% TWEEN<sup>®</sup> 80 and 5% DMSO solution in PBS were placed in a 5 mm  $\times$  5 mm quartz cuvette and irradiated continuously for 5 min, and the fluorescence intensity was acquired every 30 s at ex/em wavelengths of 505/525 nm with a 5-mm slit width. The shutter was closed between acquisitions.

#### **4.2.4 Cellular Uptake and Exclusion**

MDA-1986 cells were cultured in DMEM media containing 10% fetal bovine serum (FBS) and 1% L-glutamine at 37 °C in a 5% CO<sub>2</sub> incubator. To determine the cellular uptake of PPa and HA-ADH-PPa, cells were seeded onto 6-well plates with a density of  $1 \times 10^5$  cells/well and incubated for 24 h. The original media was replaced with 1:5:94 (v/v/v) TWEEN<sup>®</sup> 80/DMSO/media containing free PPa (1.89  $\mu$ g/ml) or HA-ADH-PPa (1.89  $\mu$ g/ml of PPa). Cells were incubated for another 1, 2, 5, 8, 24 and 48 h at 37 °C in dark. The media were then removed, and cells were washed with 3 ml of PBS and removed after incubation with 250  $\mu$ l lysis buffer [5 mM EDTA, 10 mM NaOH, 10 mM Tris base, 150 mM NaCl and 1% (v/v) Triton X-100] per well

for 10 min at room temperature. Another 750  $\mu$ l of ddH<sub>2</sub>O was added to each well, and the resulting cell lysate samples were transferred to 2-ml eppendorf tubes and centrifuged at  $20,000 \times g$  for 5 min. The fluorescence intensity of the supernatants was obtained and analyzed based on a standard curve of free PPa solution prepared in 1:3 (v/v) lysis buffer/ddH<sub>2</sub>O at a wavelength of 675 nm. The cell protein content was quantified using a Pierce™ BCA protein assay (Thermo Scientific).

To examine the exclusion of PPa or HA-ADH-PPa from MDA-1986 cells, the cells were seeded onto 6-well plates at a density of  $2.8 \times 10^5$  cells/well for 24 h and treated with the same concentrations of PPa and HA-ADH-PPa as used in the cellular uptake study. Cells were incubated for 1 h after treatment, followed by washes with PBS and incubation with fresh media for another 0.5, 1, 2, 6 or 12 h. For the HA competitive inhibition experiments, MDA-1986 cells were exposed to HA (10 mg/ml) for 24 h before the incubation with HA-ADH-PPa or PPa for 5 h. The cell lysis procedures and analysis method were identical to cellular uptake study.

#### **4.2.5 Cellular Localization**

All cell imaging experiments were performed using a Nikon Eclipse 80i epifluorescence microscope (Melville, NY) with a 60x 1.40 oil objective, and a Hamamatsu ORCA ER digital camera (Houston, TX) was used to acquire images. The MDA-1986 cells were seeded onto poly-L-lysine precoated glass coverslips (BD, Franklin Lakes, NJ) in 12-well culture plates at a density of 50,000 cells per well and allowed to grow overnight. Subsequently, cells were treated with PPa (6.48  $\mu$ g/ml) or HA-ADH-PPa (6.48  $\mu$ g/ml of PPa) in 1:5:94 (v/v/v) TWEEN® 80/DMSO/media followed by incubation at 37 °C for 5 h. The cell nuclei and lysosomes were stained with DAPI (10  $\mu$ g/ml) for 5 min and LysoTracker® Blue DND-22 (4  $\mu$ M) for 30 min, respectively. After three washes with 3 ml of PBS, the coverslips were placed on the slide glasses for imaging. The live cells were immediately imaged using a yellow fluorescent protein (YFP, ex/em, 500/535 nm) filter

set (Nikon, NY) for imaging PPa and Ultraviolet excitation (UV-2E/C, ex/em, 360/400 nm) filter set (Nikon, NY) for imaging DAPI and LysoTracker® Blue DND-22 separately.

#### **4.2.6 *In Vitro* Phototoxicity**

The MDA-1986 cells (5000/well) were seeded onto 96-well plates in 100 µl culture media and incubated for 24 h. The media was then replaced with 1:5:94 (v/v/v) TWEEN® 80/DMSO/media containing HA-ADH-PPa or free PPa with a series of different PPa concentrations (8.1 ng/ml to 8.1 µg/ml). After incubation for 24 h, cells were washed with fresh culture media three times and maintained in fresh media during irradiation with a 671-705 nm filtered halogen light (5.89 mW/cm<sup>2</sup>) for 0, 2, 5 or 10 min. Two days after irradiation, the cell viability of irradiated cells was evaluated by Resazurin-blue assay.

#### **4.2.7 *In Vivo* Fluorescence Imaging**

Female NU/NU mice were used under the guidance of the Institutional Animal Care and Use Committee at the University of Kansas. To minimize skin autofluorescence caused by chlorophyll in feed, mice were fed low chlorophyll feed (Harlan 2918 irradiated diet, Harlan Laboratories, Indianapolis, IN) for at least two weeks before imaging. A 50-µl MDA-1986 cell suspension ( $3 \times 10^7$  cells/ml) in PBS was injected into the oral sub-mucosa of a mouse using a 30-ga needle. When tumors grew to a size range of *ca.* 40 to 80 mm<sup>3</sup> [tumor volume =  $0.52 \times (\text{width})^2 \times (\text{length})$ ], 50 µl of PBS containing HA-ADH-PPa [0.5 mg/kg body weight (B.W.) of PPa] was injected subcutaneously into the cheek of the animal, which were anesthetized with 1.5% isoflurane in oxygen. The injection area was fluorescently imaged from 5 min to 48 h using a CRI Maestro Flex fluorescence imager (CRI Inc., Woburn, MA) equipped with a 503 - 555 nm filtered

xenon excitation light and a 580 nm long-pass emission filter. The fluorescence intensity of the tumor site was quantified using ImageJ and the following equation:

Corrected Total Fluorescence = Integrated Density - (Tumor Area  $\times$  Mean Fluorescence of Normal tissue).

#### **4.2.8 *In Vivo* PDT Treatment**

NU/NU mice bearing head and neck tumors were prepared in an identical manner as described above. When tumors reached *ca.* 40 to 80 mm<sup>3</sup> in size, mice were randomly divided to four groups: saline *s.c.* group (N = 4), HA-ADH-PPa *s.c.* group (0.5 mg PPa/kg B.W., N = 4), PPa *i.v.* group (0.5 mg PPa/kg B.W., N = 4), HA-ADH-PPa *s.c.* group (0.8 mg PPa/kg B.W., N = 3). At 6 h (PPa *i.v.* group) or 24 h (HA-ADH-PPa *s.c.* group) post-injection, the primary tumor and the parotid lymph nodes were irradiated by a diode laser with a laser intensity of 150 J/cm<sup>2</sup> at 685 nm. The treatment was repeated 4 times at a frequency of once per week or terminated early if the tumors disappeared. The therapeutic response of each group was monitored by measuring the tumor volume with a digital caliper. The animals were euthanized when tumor size reached 1000 mm<sup>3</sup> or the tumor became ulcerated.

#### **4.2.9 Statistical Analysis**

All experiments were conducted in triplicate and the data are expressed as the mean  $\pm$  standard deviation. Significant differences were examined by student t-test or one-way analysis of variance (ANOVA) followed by Tukey's post hoc tests (\* $p \leq 0.05$ , \*\* $p \leq 0.01$ , \*\*\* $p \leq 0.001$  and \*\*\*\* $p \leq 0.0001$ ) using GraphPad Prism Software version 8. Comparisons are considered not statistically significant (ns) when  $p > 0.05$ .

## 4.3 Results

### 4.3.1 Synthesis and Physical Characterization of HA-ADH-PPa Conjugate

HA-ADH-PPa was synthesized by the conjugation of the carboxyl group on PPa to the glucuronic acid of HA via ADH linker. The conjugation between PPa and HA-ADH was verified and calculated using  $^1\text{H}$ -NMR spectroscopy (400 MHz, 6:1 (v/v) DMSO- $d_6$ :  $\text{D}_2\text{O}$ ). The spectrum showed HA characteristic peaks at  $\delta$  1.82 (s, 3H, HA acetyl group), 3.0-3.9 (HA backbone) and 4.10 (s, 4H, HA hydroxyl groups), while the methylene groups of ADH was observed at  $\delta$  1.50 (p, 4H) and 2.34 (t, 4H).<sup>33</sup> Besides, many characteristic peaks of PPa were observed at  $\delta$  7.22 (dd, 1H), 7.87 (s, 4H, CONH), 8.1 (dd, 1H), 8.37 (dd, 1H), 8.84 (s, 1H), 9.38 (s, 1H) and 9.67 (s, 1H) as shown in **Figure 2**.<sup>34</sup> The degree of PPa conjugation was determined by comparing the integration of the PPa peak at ( $\delta$  9.38) with the methylene protons of HA acetyl group ( $\delta$  1.82) which calculated to be *ca.* 2.70 % (wt/wt). Further evidence on the PPa conjugation to HA-ADH was observed based on the difference in equivalent retention times using a GPC coupled with ELSD (dotted) and UV/Vis detection (dashed, 600 nm) at approximately 10 min (**Figure 3**). HA-ADH-PPa displayed a slightly smaller hydrodynamic volume compared to HA (solid) on GPC. This was possibly due to the reduced repulsive interactions among the carboxylate anions on HA-ADH-PPa after conjugation.<sup>35</sup> The absorption and fluorescence spectra of HA-ADH-PPa conjugate and free PPa are shown in **Figure 4**. To collect their individual spectra, HA-ADH-PPa, free PPa and a physical mixture of HA and PPa were prepared in 1:5:94 (v/v/v) TWEEN® 80/DMSO/ddH<sub>2</sub>O, as free PPa is insoluble in purely aqueous solutions. Compared with free PPa and the physical mixture, HA-ADH-PPa conjugates have broader PPa absorbance peaks at both the Soret band region around 400 nm and the Q band region around 670 nm (**Figure 4a**). In addition, the Soret band and the Q band of HA-ADH-PPa conjugate have a blueshift of

approximately 30 nm and a redshift of approximately 10 nm, respectively. This phenomenon was also observed by Savellano and his co-workers on their PPa-immunoconjugates.<sup>36</sup> Moreover, HA-ADH-PPa and PPa showed identical fluorescence emission spectra with maximum emission wavelengths of 673 nm when excited at 419 nm (**Figure 4b**). The absorbance intensity at 675 nm and the fluorescence intensity at 400/600 nm (ex/em) were measured to calculate the loading degree of PPa on the HA-ADH polymer, which was determined to be 2% (wt/wt). Additionally, TEM images were collected, which showed that the HA-ADH-PPa nanoparticles were roughly spherical with a mean diameter of  $83.1 \pm 17.5$  nm, as analyzed by ImageJ software (**Figure 5**). The conjugates could not be size measured by dynamic light scattering due to the fluorescent overlap with the red laser used in available instruments (ZetaPALS, Brookhaven Instrument Corporation).

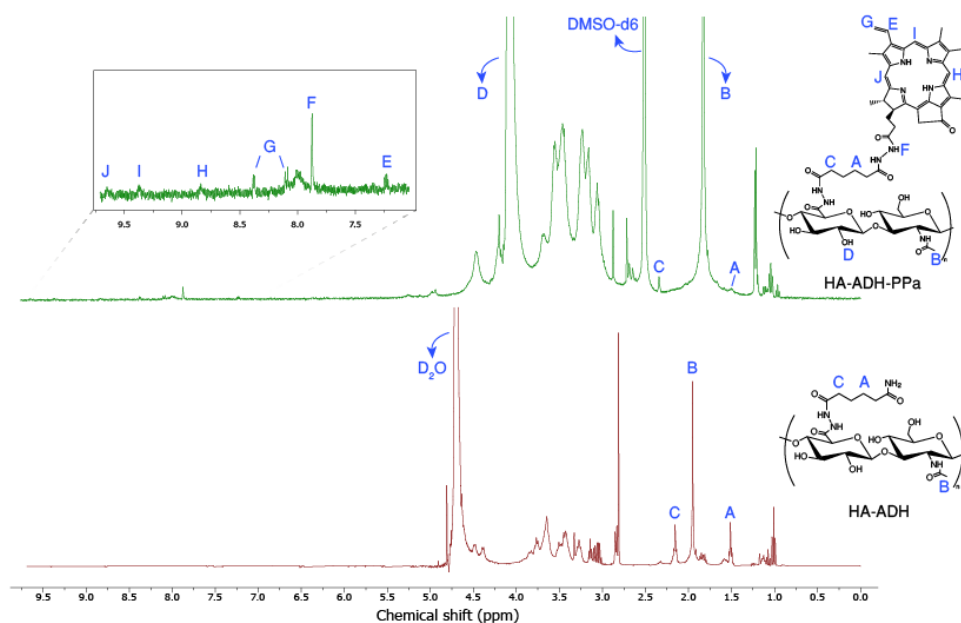


**Figure 2** <sup>1</sup>H-NMR spectra of (a) HA-ADH and (b) HA-ADH-PPa.

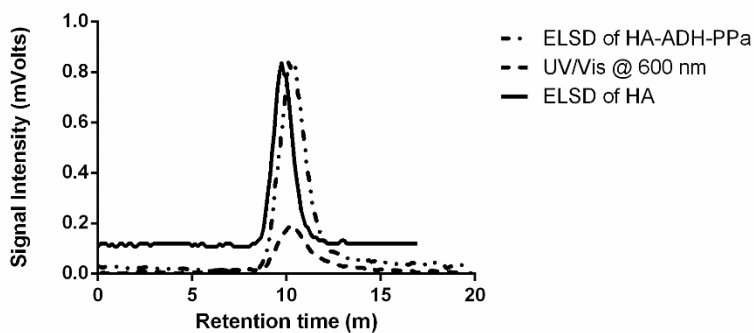


**Figure 3** Chromatograms of HA and HA-ADH-PPa conjugates. Chromatograms of HA (ELSD, solid) HA-ADH-PPa conjugates generated by a GPC with an ELSD (dash-dot) detector and a UV-Vis (600 nm, dashed) detector.

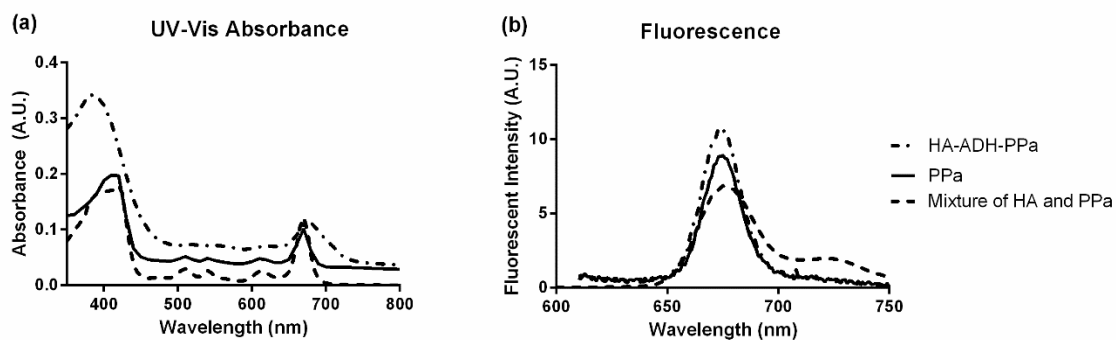


**Figure 4** UV-Vis spectra and fluorescence emission spectra of PPa and HA-ADH-PPa conjugates. (a) UV-Vis spectra, and (b) fluorescence emission spectra at excitation wavelength of 419 nm of HA-ADH-PPa polymer nanoparticle (dash-dot), free PPa (solid) and physical mixture of HA and PPa (dashed).



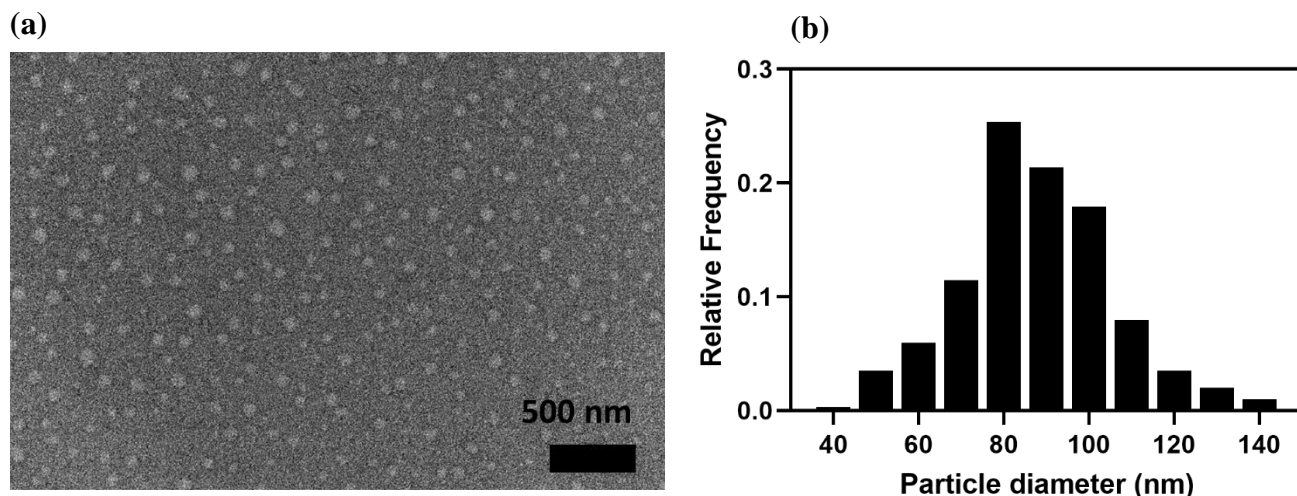


**Figure 5** (a) TEM image of HA-ADH-PPa conjugates, (b) the size distribution of the particles as analyzed by ImageJ software

#### 4.3.2 Singlet oxygen generation of PPa from HA-ADH-PPa

Upon laser irradiation, PPa generates singlet oxygen that kills tumor cells. The release of the singlet oxygen can be analyzed qualitatively by monitoring the increase in the fluorescence intensity of SOSG solution due to the production of SOSG endoperoxide (SOSG-EP), which is a strong green fluorescent, when SOSG reacts with singlet oxygen.<sup>37</sup> **Figure 6** shows the fluorescence intensity at 525 nm as a function of photoirradiation time for detecting the generation of singlet oxygen. In the absence of laser irradiation, the rates of singlet oxygen generation from free PPa and HA-ADH-PPa were decreased significantly. Moreover, there was no obvious difference in the rates of singlet oxygen generation between free PPa and HA-ADH-PPa. It is reported that SOSG-EP is also an efficient singlet oxygen photosensitizer,<sup>38</sup> thus we measured fluorescence intensity of an SOSG solution without PPa or HA-ADH-PPa. The result suggested that the generation of singlet oxygen was specifically from PPa upon laser irradiation.

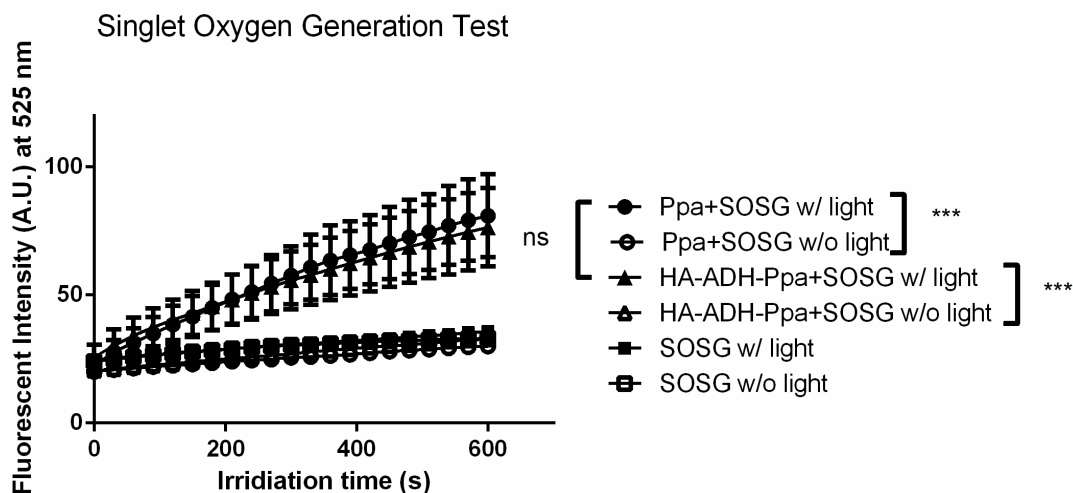


**Figure 6** Measurements of  $^1\text{O}_2$  generation using SOSG as a reporter probe (\*\*\*)  $P \leq 0.001$ ; ns,  $P > 0.05$ ).

#### 4.3.3 Cellular Internalization and Exclusion of HA-ADH-PPa and PPa in MDA-1986 Cells

The cellular uptake behavior of HA-ADH-PPa was monitored as a function of incubation time (1, 2, 5, 8, 24 and 48 h) and compared with the same concentration of free PPa by measuring the intracellular fluorescence intensity of PPa. As shown in **Figure 7a**, both free PPa and HA-ADH-PPa showed increased cellular accumulation as the incubation time was increased. Although the intracellular concentration of HA-ADH-PPa was lower than that of PPa, it was noted that the accumulative internalization of HA-ADH-PPa increased by *ca.* 5 times in 48 h, comparing to *ca.* 1.4 times increase in intracellular content of free PPa. The more efficient cellular uptake of HA-ADH-PPa was possibly due to the more effective endocytosis by the cancer cells and slower passive diffusion of free PPa into the cells. After 1 h exposure to HA-ADH-PPa and PPa (1.89  $\mu\text{g}/\text{ml}$ ) and subsequent incubation in PPa-free cell culture media, the intracellular concentrations of PPa were determined. As shown in **Figure 7b**, more than 90% of free PPa molecules were

cleared from the cells via passive diffusion across plasma membrane into PPa-free media in 2 h; while around 60% of PPa remained in the MDA-1986 cancer cells 2 h after HA-ADH-PPa treatment. It took more than 12 h, 5-fold longer than that of free PPa, for HA-ADH-PPa to be excluded from cells below detectable limits. This result suggested that PPa molecules were transported by HA nanoparticles via an endocytic pathway, and PPa was slowly released from HA in the cells. To determine whether the cellular uptake of HA-ADH-PPa nanoconjugates is regulated by the receptors for HA, cells were pretreated with excess amount of HA to saturate specific HA-receptors on the surface of tumor cells, potentially inhibiting the uptake of HA-ADH-PPa but not free PPa. It was shown that pretreatment with 10 mg/ml HA for 24 h prior to the addition of HA-ADH-PPa caused a significant (*ca.* 20%) reduction in the cellular uptake compared to the non-pretreated cells (**Figure 7c**). Whereas the internalization of free PPa remained unaffected by the exposure to 10 mg/ml HA. This result indicated that the internalization of HA-ADH-PPa nanoconjugates was inhibited by blocking HA receptors, and thus a receptor-mediated endocytic pathway was important for HA-ADH-PPa uptake.

#### **4.3.4 Cellular Localization of HA-ADH-PPa Vs free PPa**

Confocal fluorescence imaging was used to evaluate the localization of HA-ADH-PPa and PPa in subcellular organelles upon entering the cells. The confocal images of MDA-1986 cells preincubated with HA-ADH-PPa and PPa for 5 h without laser irradiation are shown in **Figure 8 A-L**. Co-staining experiments were performed using DAPI to stain cell nuclei (blue), and LysoTracker<sup>®</sup> Blue to stain lysosomes (red). For lysosomal localization, HA-ADH-PPa was observed to have significant co-localization in lysosomes as shown in **Figure 8C**. However, free PPa molecules were partially co-localized with lysosomes (**Figure 8I**). For nuclei localization, the

clear green fluorescence surrounded the cell nuclei in both **Figure 8F** and **8L**, indicates that neither HA-ADH-PPa nor PPa entered the cell nuclei.

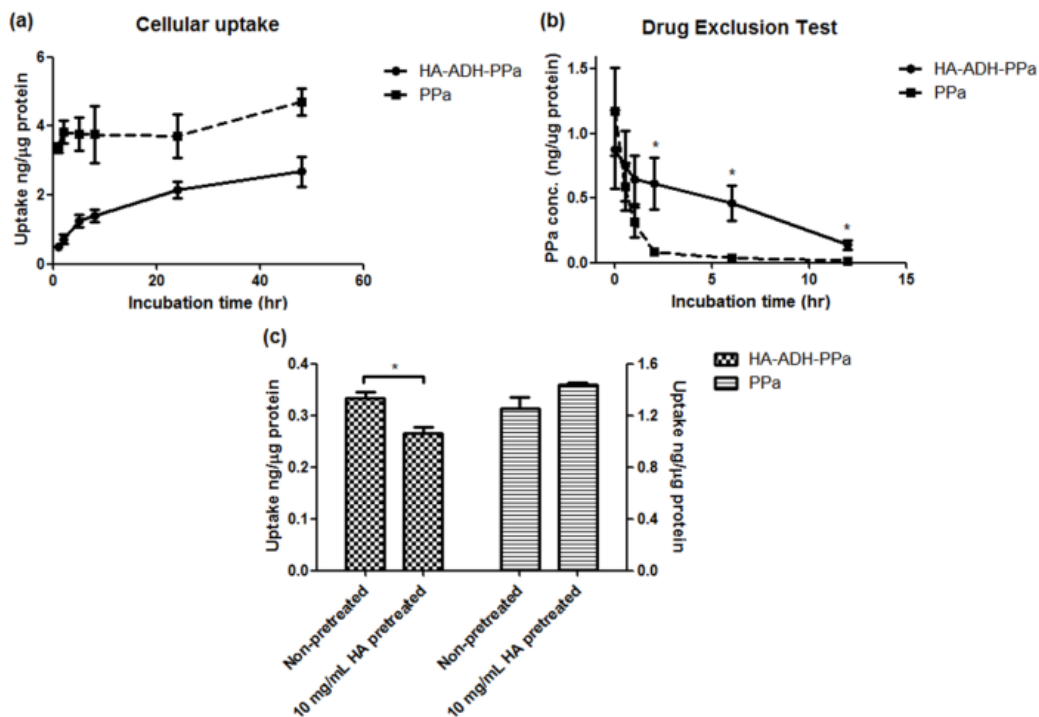


**Figure 7** Cellular uptake of HA-ADH-PPa and PPa by MDA-1986 cells. (a) Cellular uptake by MDA-1986 cells after incubation with HA-ADH-PPa (solid) and PPa (dashed) for 1, 2, 5, 8, 24 and 48 h; (b) Cellular exclusion by MDA-1986 cells after 1 h treatment with HA-ADH-PPa (solid) or PPa (dashed), followed by washes with PBS and incubation with fresh media for another 0.5, 1, 2, 6 and 12 h; (c) Cellular uptake by MDA-1986 cells after pretreatment with 10 mg/ml HA (24 h) and incubation with HA-ADH-PPa and PPa for 5 h (\*  $P \leq 0.05$ ).

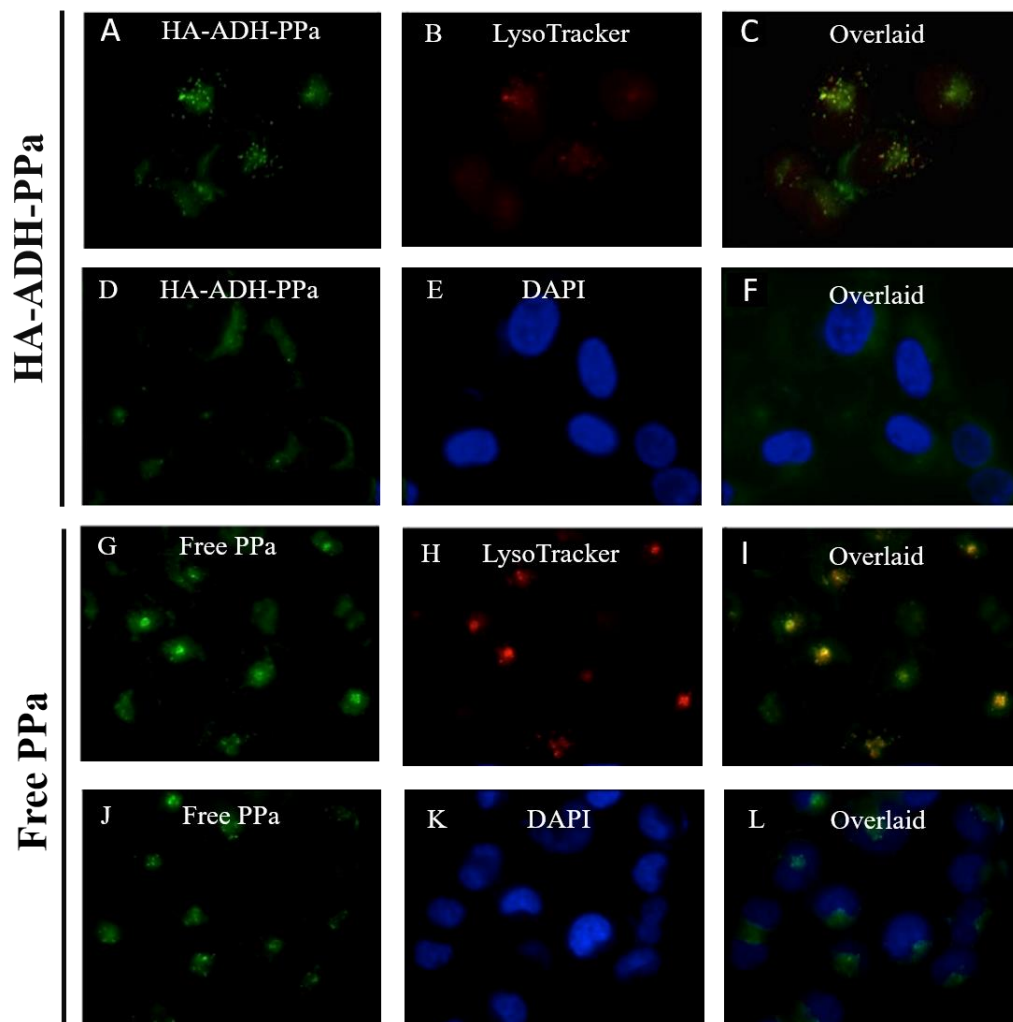


**Figure 8** Confocal fluorescence microscopy of MDA-1986 cells treated with HA-ADH-PPa or PPa (green), and co-stained with DAPI (blue) and LysoTracker® Blue (red). Left panels are photosensitizer fluorescence images (A & D, HA-ADH-PPa; G & J, free PPa). Middle panels show the LysoTracker® Blue (B & H) and DAPI (E & K) co-staining, while right panels (C, F, I & L) show the overlaid images (60x magnification).

#### 4.3.5 Cellular Phototoxicity of HA-ADH-PPa

Cellular internalization experiments showed that the intracellular fluorescence of PPa plateaued at *ca.* 24 h (**Figure 7a**). Therefore, MDA-1986 cells were incubated with HA-ADH-PPa

at a series of PPa concentrations (8.1 ng/ml to 8.1  $\mu$ g/ml) for 24 h, followed by washing with PPa-free media and light irradiation at a fluence of 5.89 mW/cm<sup>2</sup> and compared to free PPa. In the absence of light, no significant cytotoxicity was observed on MDA-1986 cells with both HA-ADH-PPa and PPa, using equivalent PPa concentrations of 4  $\mu$ g/ml as shown in **Figure 9a**. In case of irradiation, cytotoxicity began to appear at much lower concentrations of PPa with different times of irradiation, as shown in **Figure 9**, b-d. The cytotoxicity of PPa increased as the light irradiation time increased (**Table 1**). It could be assumed that intracellular concentration of PPa in HA-ADH-PPa treated cells was comparable to that of free PPa treated cells. For example, after 24 h incubation with drugs, the uptake of free PPa in MDA-1986 cells was *ca.* 1.7 times higher than that of HA-ADH-PPa (**Figure 7a**), whereas the amount of free PPa excluded by cells within 30 min was 2.8 times greater than that of the polymeric conjugates (**Figure 7b**), and hence the PPa concentrations in both groups were roughly equal. However, in corresponding phototoxicity experiments, the IC<sub>50</sub> values of HA-ADH-PPa were higher than those of free PPa in response to every light dose tested (**Table 1**). It is well documented that singlet oxygen is unable to diffuse beyond the intracellular compartment where it is being produced, and the lysosomes are less critical organelles than mitochondria in photosensitizing process.<sup>39</sup> Thus, the major subcellular localization into lysosomes, and not the mitochondria, may account for the lower phototoxicity of HA-ADH-PPa. The concentration of HA-ADH-PPa at the treatment site could help compensate for the lower phototoxicity.

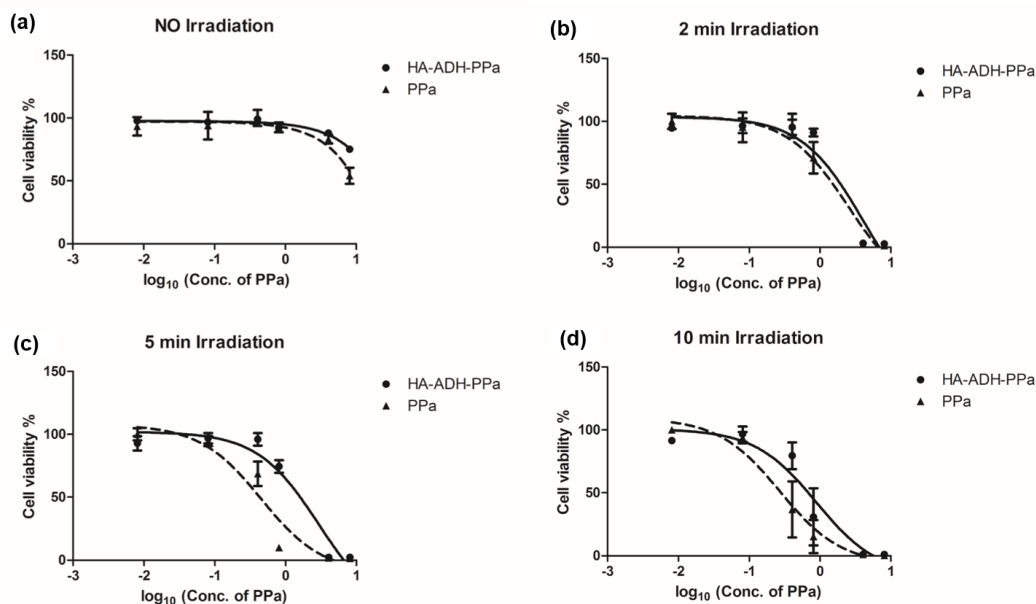


**Figure 9** Anti-proliferation of HNSCC MDA-1986 cells by HA-ADH-PPa conjugates and free PPa. Inhibition of HNSCC MDA-1986 cell growth by HA-ADH-PPa (solid lines and ●) or free PPa (dashed lines and ▲) after 24 h incubation with 0-, 2-, 5- and 10-min light irradiation (a-d) respectively.

IC <sub>50</sub> (μg/ml of PPa) <sup>a</sup>			
Irradiation time	2 min	5 min	10 min
HA-ADH-PPa	4.13 ± 0.55	3.05 ± 0.79	1.42 ± 1.50
PPa	2.58 ± 1.18	0.45 ± 0.10	0.47 ± 0.51

<sup>a</sup> Determined from data shown in **Figure 8**

**Table 1** IC<sub>50</sub> values of HA-ADH-PPa or free PPa in MDA-1986 cells at different irradiation durations.

#### 4.3.6 *In Vivo* Fluorescence Imaging

An orthotopic murine tumor xenograft was established by injecting highly tumorigenic human HNSCC MDA-1986 cells into the buccal mucosa of nude mice. The primary tumor invaded the mandible and metastasized to the parotid and cervical lymph nodes. The incidence of distant metastasis has been verified in our previous study.<sup>40</sup> The intrinsic fluorescence of the photosensitizer, PPa, enables the detection of HA-ADH-PPa in the region of lymphatic metastases using fluorescence imaging *in vivo*. Thus, HA-ADH-PPa was injected adjacent to the primary tumor; and fluorescent images of the head and neck area were obtained at various time points from 0 to 48 h. As shown in **Figure 10**, HA-ADH-PPa nanoconjugates were drained toward and accumulated effectively at both of the periphery of the neoplastic tissue and the peripheral locoregional lymphatics (parotid lymph nodes) in 24 h, which is possibly due to the lymphangiogenesis and lymphatic metastasis. Moreover, the exact location of the tumor was clearly outlined as a result of the intense fluorescence signal emitted by the surrounding tissues and lymph nodes, which provides a valuable guidance for photodynamic therapy of metastatic HNSCC.



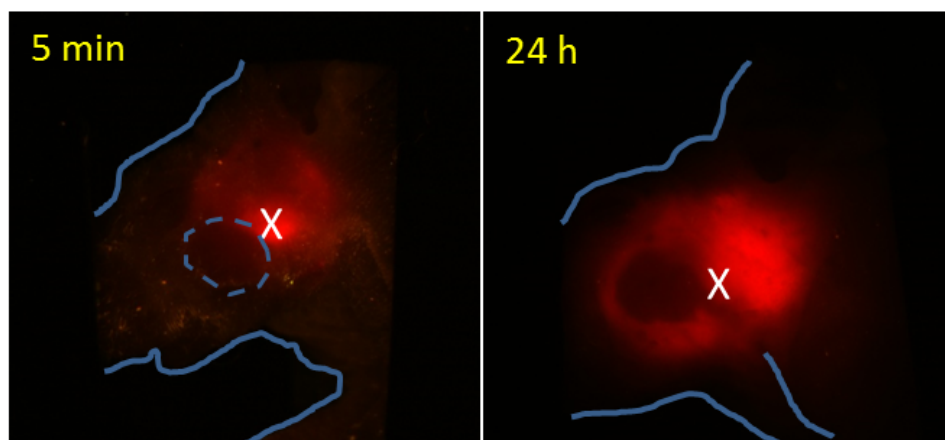


**Figure 10** Fluorescence images of the head and neck area of a mouse at 5 min and 24 h post-injection of HA-ADH-PPa. Dashed circle and × indicate the primary tumor and the injection site, respectively.

#### 4.3.7 *In Vivo* PDT Treatment

In order to evaluate the therapeutic potential of HA-ADH-PPa compared to free PPa, four groups of female nude mice bearing HNSCC xenografts were treated with saline s.c., free PPa i.v. (0.5 mg/kg B.W.), HA-ADH-PPa s.c. (0.5 mg/kg PPa) and HA-ADH-PPa s.c. (0.8 mg/kg). Laser irradiation was conducted at 6 h post-injection of free PPa and 24 h post-injection of HA-ADH-PPa. These time points were chosen based on observations by *in vivo* imaging of the  $T_{\max}$  of fluorescence in the tumor region after s.c. injection of HA-ADH-PPa or tail vein i.v. injection of PPa. The tumor growth rates of the three groups, including saline s.c., free PPa i.v. (0.5 mg/kg B.W.) and HA-ADH-PPa s.c. (0.5 mg/kg PPa) after four consecutive treatments were compared to evaluate the therapeutic efficacy of HA-ADH-PPa nanoconjugates (**Figure 11a**). It was found that HA-ADH-PPa s.c. combined with laser treatment caused significant tumor suppression. The final mean tumor size was *ca.* 300 mm<sup>3</sup> after 25 days, which was 60% smaller than that of the non-treated group. As shown in **Figure 11b**, survival time was greatly improved for the mice treated

with HA-ADH-PPa s.c. (0.5 mg/kg PPa) compared to the non-treated and free PPa i.v.(0.5 mg/kg) treated groups. No statistically significant difference was observed between the non-treated and the free PPa i.v. (0.5 mg/kg) groups. In addition, tumors on all mice treated with HA-ADH-PPa s.c. (0.8 mg/kg PPa) were cured after the 2<sup>nd</sup> treatment at week 2 (**Figure 11c**). The results of the *in vivo* treatment indicated that as a drug nanocarrier, HA greatly enhanced the anticancer efficacy of PPa compared to the conventional i.v. photosensitizer treatment.

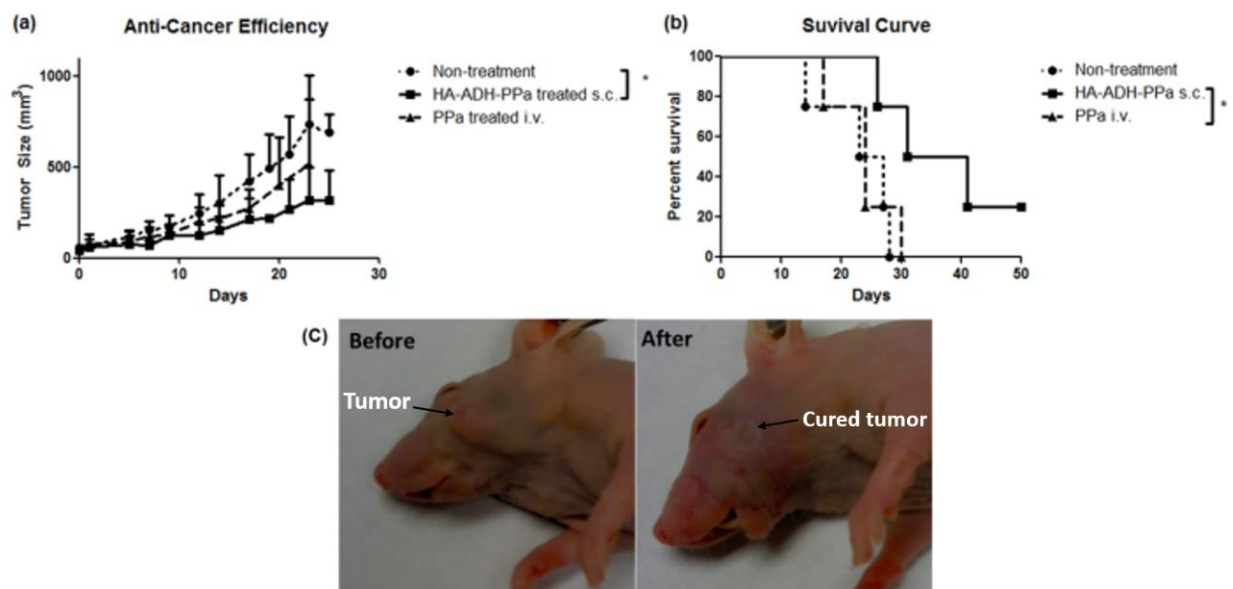


**Figure 11** Measurement of tumor size and survival time of mice. (a) Female NU/NU mice were administered saline s.c., HA-ADH-PPa s.c. and free PPa i.v. (0.5 mg/kg PPa, N=4). (b) Survival curve of treated and untreated NU/NU mice. (c) Picture of a NU/NU mouse with HNSCC before and after 2 weekly treatments of HA-ADH-PPa s.c. (0.8 mg/kg PPa, N = 3).

## 4.4 Discussion

The objective of the study is to develop HA-PPa nanoconjugate to enhance the PPa aqueous solubility, tissue selectivity, and maintain high photoactivity. The high aqueous solubility of HA, a carbohydrate that is a structural component of the tissue extracellular space, was expected to improve the solubility of the resulting HA-ADH-PPa nanoconjugate. The selective uptake of HA-ADH-PPa by tumor cells is attributed to the high affinity of HA to CD44 receptor,<sup>27</sup> RHAMM,<sup>28,29</sup> and LYVE-1,<sup>30</sup> which are overexpressed in tumor tissues.<sup>28</sup> The preservation of photoactivity may be ascribed to the low loading degree of PPa on HA-ADH. Thus, the nanoconjugates showed potential for delivering concentrated PPa for locoregional treatment of primary tumors and local lymphatic metastases.

A loading degree of 2% (wt/wt) PPa on HA-ADH was achieved and no aggregation of the nanoconjugates. However, when the loading degree was increased to 3% (wt/wt) by increasing the stoichiometric ratio of PPa to HA-ADH, the solubility of HA was significantly decreased; this could possibly be due to an irreversible aggregation of PPa in aqueous solution and increased occupation of ADH amino groups. An added advantage of the lower loading value arises in that native HA is transported via lymphatic vessels to lymph nodes where it is catabolized by receptor-mediated endocytosis followed by lysosomal degradation. A lower loading degree of PPa on HA-ADH may thus better preserve the binding specificity and affinity of HA to the receptors in the lymphatic system, such as LYVE-1 on the wall of lymph vessels.<sup>41</sup>

HA-ADH-PPa was synthesized via a covalent amide bond linkage of the carboxyl group on PPa to HA-ADH. The success of the synthesis was verified using both <sup>1</sup>H-NMR and GPC. The resulting conjugates could be self-assembled in aqueous solution into nanoparticles where HA

forms the hydrophilic shell and PPa forms the hydrophobic core. The morphology and particle size were determined via TEM as shown in **Figure 5**, which demonstrated a spherical morphology with a particle diameter  $83.1 \pm 17.5$  nm. The observed size range was reported for different HA conjugates. Yoon et al.<sup>42</sup> prepared chlorin e6 – Conjugated HA nanoparticles which had a particle size around 200 nm. Also, Choi et al. (43) synthesized Amphiphilic HA-5 $\beta$ -cholanic acid conjugates with particle sizes around 300 nm. The difference in size may be attributed to the different conjugating material, differing particle preparation conditions and imaging method. The self-organizing behavior of polymer is very concentration dependent, thus their relationship is usually described using critical concentration terms such as critical self-quenching concentration (CQC). The CQC of HA-PS conjugates was investigated by Li et al.<sup>44</sup> who found that the micelle-like nanoparticles were formed significantly when the polymer concentration was higher than 0.1 mg/ml and PS concentration was higher than 0.013 mg/ml. However, in our work, no polymer aggregation was detected, and thus no photoactivity quenching was expected due to the lower loading degree of PPa on HA-ADH.

Upon irradiation of the HA-ADH-PPa in the tumor area with light equivalent to its absorption band, singlet oxygen is generated which causes irreversible damage to the tumor cells leading to an apoptosis.<sup>45</sup> The mechanism of singlet oxygen generation is due to the interaction of an excited state of PPa, i.e. “triplet state” that forms due to the irradiation, with oxygen molecules present in the cells. An energy transfer occurs between the PPa and oxygen to form a singlet oxygen free radical, which is responsible for the PDT therapeutic efficiency.<sup>46</sup> Thus, any PS polymeric carrier should satisfy two fundamental requirements; the first is the nanocarrier should not significantly quench singlet oxygen, while the other is the PS-encapsulated polymer matrix should be permeable to the newly generated singlet oxygen.<sup>47</sup> As shown in **Figure 6**, no significant

difference in the rates of singlet oxygen generation was observed between HA-ADH-PPa and free PPa at same concentrations of PPa under increased light intensity up to 2.35 J/cm<sup>2</sup>, suggesting that HA-ADH-PPa nanocomposite neither quenched, entrapped singlet oxygen nor blocked its diffusion into the intracellular domains.

The results of the intracellular localization study showed green-fluorescent puncta, attributed to PPa, were widely distributed within the cytoplasm. In addition, significant co-localization of HA-ADH-PPa with lysosomes was observed, while no nuclei localization was observed. These findings agree with Liu et al.<sup>48</sup> where they loaded PPa to a polymeric nanocarrier. The loaded-PPa was observed to localize at mitochondria and lysosomes but not the nucleus. Due to pH trapping, lysosomes can accumulate weakly basic compounds such as PPa.<sup>49</sup> Mitochondria and lysosomes are crucial for cell viability, thus any damage to them by PDT could efficiently induce the cell to undergo apoptosis.<sup>50</sup>

To better understand the uptake of nanoconjugates versus free PPa by MDA-1986 cells, intracellular PPa concentration was measured after 1 h PPa treatment. Only 10% of free PPa was retained by cells after 2 hours, versus 60% of PPa for HA-ADH-PPa polymeric conjugates (**Figure 7b**). This may be attributed to enzymatic degradation of HA-ADH-PPa by lysosomal hyaluronidase followed by a slow release of PPa into the cytosol. A similar PS release pattern from HA nanoparticles was also observed by Yoon et al.<sup>42</sup> in their *in vitro* release study, in which *ca.* 40% of Ce6 was released after 2 hours while incubating Ce6-HA with hyaluronidase at 37 °C.

To evaluate the therapeutic efficacy, mice bearing MDA-1986 tumors were treated with either (a) HA-ADH-PPa (0.5 mg/kg PPa) injected directly into peri-tumoral subcutaneous tissue, or (b) free PPa injected i.v. into the tail vein. Tumor growth was suppressed more successfully by s.c. HA-ADH-PPa (0.5 mg/kg PPa) than by i.v. free PPa treated mice (**Figure 11a**). The result of

the tumor response suggests that s.c. HA-ADH-PPa achieved enhanced therapeutic efficacy relative to the conventional i.v. PPa, which might be ascribed to the specific lymphatic drainage of the HA nanocarrier and the direct localized route of drug administration. Furthermore, tumors in mice treated with a higher dose of HA-ADH-PPa (0.8 mg/kg PPa) demonstrated hemorrhage suggesting notable efficacy. All three high-dose mice were cured after two treatments, and treated tissues recovered readily during the course of one week. This rapid healing might be due to the reparative and protective effects of HA, which has been used widely for healing cutaneous wounds, burns and ulcers.

## 4.5 Conclusion

This study describes a novel polymeric HA nanocarrier conjugated to the photosensitizer PPa for intratumoral and intralymphatic delivery. The conjugation of PPa to HA-ADH was shown to enhance the water solubility of PPa, increase its accumulation in HNSCC, and preserve its photoactivity. The study also demonstrated the novel compound's use in treating a focal malignancy and its locoregional lymphatics. In HNSCC tumor-bearing mice, *in vivo* efficacy and survival time were greatly improved versus conventional PDT therapy. Accordingly, the proposed HA-based nanocarrier has been demonstrated as a promising vehicle for PDT. In future studies, we plan to test the synergistic potential of PDT and immunotherapy. Wherein, we believe the ability to highly localize tumor apoptosis with the HA-PPa and PDT, without destruction of surrounding tissues, may activate the immune system in immunologically cold tumors.<sup>51</sup>

## 4.6 Funding

This work was funded in part by the National Institutes of Health (1R01CA173292-01, PI MLF; 5-P30-CA168524-02, PI Jensen). Daniel J Aires and M Laird Forrest have a financial interest in HylaPharm, a company developing HA-based therapeutics.

## 4.7 Acknowledgments

This chapter has been recently published in the journal of Photodiagnosis and Photodynamic Therapy.<sup>52</sup> The study was conducted by Ti Zhang, Moustafa M Abdelaziz and Shuang Cai under the supervision of Xinmai Yang, Daniel J Aires, M Laird Forrest. Portions of that work were also published in Ti Zhang's PhD dissertation. My contribution was mainly to validate and reproduce the synthetic methods, further characterize the crucial material properties to *in vivo* behavior (e.g. NMR characterization, sizing and imaging of particles) and to complete the writeup of the study.

## 4.8 References

- (1) Johnson, D. E.; Burtneß, B.; Leemans, C. R.; Lui, V. W. Y.; Bauman, J. E.; Grandis, J. R. Head and Neck Squamous Cell Carcinoma. *Nat Rev Dis Primers* **2020**, *6* (1), 1–22.  
<https://doi.org/10.1038/s41572-020-00224-3>.
- (2) Sunar, U. Monitoring Photodynamic Therapy of Head and Neck Malignancies with Optical Spectroscopies. *World J Clin Cases* **2013**, *1* (3), 96–105.  
<https://doi.org/10.12998/wjcc.v1.i3.96>.
- (3) Sung, H.; Ferlay, J.; Siegel, R. L.; Laversanne, M.; Soerjomataram, I.; Jemal, A.; Bray, F. Global Cancer Statistics 2020: GLOBOCAN Estimates of Incidence and Mortality Worldwide for 36 Cancers in 185 Countries. *CA Cancer J Clin* **2021**, *71* (3), 209–249.  
<https://doi.org/10.3322/caac.21660>.
- (4) Saba, N. F.; Khuri, F. R. Optimizing Systemic Therapy in Squamous Cell Carcinoma of the Head and Neck with a Focus on Targeted Agents. *Curr Opin Oncol* **2009**, *21* (3), 232–237. <https://doi.org/10.1097/cco.0b013e32832a56b3>.
- (5) Yan, F.; Knochelmann, H. M.; Morgan, P. F.; Kaczmar, J. M.; Neskey, D. M.; Graboyes, E. M.; Nguyen, S. A.; Ogretmen, B.; Sharma, A. K.; Day, T. A. The Evolution of Care of Cancers of the Head and Neck Region: State of the Science in 2020. *Cancers (Basel)* **2020**, *12* (6). <https://doi.org/10.3390/cancers12061543>.
- (6) Conley, B. A. Treatment of Advanced Head and Neck Cancer: What Lessons Have We Learned? *J Clin Oncol* **2006**, *24* (7), 1023–1025.  
<https://doi.org/10.1200/JCO.2005.05.0682>.
- (7) Upile, T.; Jerjes, W.; Sterenborg, H. J. C. M.; El-Naggar, A. K.; Sandison, A.; Witjes, M. J. H.; Biel, M. A.; Bigio, I.; Wong, B. J. F.; Gillenwater, A.; MacRobert, A. J.; Robinson,



- D. J.; Betz, C. S.; Stepp, H.; Bolotine, L.; McKenzie, G.; Mosse, C. A.; Barr, H.; Chen, Z.; Berg, K.; D'Cruz, A. K.; Stone, N.; Kendall, C.; Fisher, S.; Leunig, A.; Olivo, M.; Richards-Kortum, R.; Soo, K. C.; Bagnato, V.; Choo-Smith, L.-P.; Svanberg, K.; Tan, I. B.; Wilson, B. C.; Wolfson, H.; Yodh, A. G.; Hopper, C. Head & Neck Optical Diagnostics: Vision of the Future of Surgery. *Head Neck Oncol* **2009**, *1*, 25.  
<https://doi.org/10.1186/1758-3284-1-25>.
- (8) Bourhis, J.; Overgaard, J.; Audry, H.; Ang, K. K.; Saunders, M.; Bernier, J.; Horiot, J.-C.; Le Maître, A.; Pajak, T. F.; Poulsen, M. G.; O'Sullivan, B.; Dobrowsky, W.; Hliniak, A.; Skladowski, K.; Hay, J. H.; Pinto, L. H. J.; Fallai, C.; Fu, K. K.; Sylvester, R.; Pignon, J.-P.; Meta-Analysis of Radiotherapy in Carcinomas of Head and neck (MARCH) Collaborative Group. Hyperfractionated or Accelerated Radiotherapy in Head and Neck Cancer: A Meta-Analysis. *Lancet* **2006**, *368* (9538), 843–854.  
[https://doi.org/10.1016/S0140-6736\(06\)69121-6](https://doi.org/10.1016/S0140-6736(06)69121-6).
- (9) Pignon, J.-P.; le Maître, A.; Maillard, E.; Bourhis, J.; MACH-NC Collaborative Group. Meta-Analysis of Chemotherapy in Head and Neck Cancer (MACH-NC): An Update on 93 Randomised Trials and 17,346 Patients. *Radiother Oncol* **2009**, *92* (1), 4–14.  
<https://doi.org/10.1016/j.radonc.2009.04.014>.
- (10) Block, K. I.; Koch, A. C.; Mead, M. N.; Tothy, P. K.; Newman, R. A.; Gyllenhaal, C. Impact of Antioxidant Supplementation on Chemotherapeutic Toxicity: A Systematic Review of the Evidence from Randomized Controlled Trials. *International Journal of Cancer* **2008**, *123* (6), 1227–1239. <https://doi.org/10.1002/ijc.23754>.

- (11) Biel, M. A. Photodynamic Therapy Treatment of Early Oral and Laryngeal Cancers. *Photochem Photobiol* **2007**, 83 (5), 1063–1068. <https://doi.org/10.1111/j.1751-1097.2007.00153.x>.
- (12) Li, X.; Lee, S.; Yoon, J. Supramolecular Photosensitizers Rejuvenate Photodynamic Therapy. *Chem. Soc. Rev.* **2018**, 47 (4), 1174–1188. <https://doi.org/10.1039/C7CS00594F>.
- (13) Sunar, U.; Rohrbach, D.; Rigual, N.; Tracy, E.; Keymel, K.; Cooper, M. T.; Baumann, H.; Henderson, B. H. Monitoring Photobleaching and Hemodynamic Responses to HPPH-Mediated Photodynamic Therapy of Head and Neck Cancer: A Case Report. *Opt Express* **2010**, 18 (14), 14969–14978. <https://doi.org/10.1364/OE.18.014969>.
- (14) Photofrin - FDA prescribing information, side effects and uses <https://www.drugs.com/pro/photofrin.html> (accessed 2021 -06 -20).
- (15) Delanaye, L.; Ali Bahri, M.; Tfibel, F.; Fontaine-Aupart, M.-P.; Mouithys-Mickalad, A.; Heine, B.; Piette, J.; Hoebeke, M. Physical and Chemical Properties of Pyropheophorbide-a Methyl Ester in Ethanol, Phosphate Buffer and Aqueous Dispersion of Small Unilamellar Dimyristoyl-1- $\alpha$ -Phosphatidylcholine Vesicles. *Photochemical & Photobiological Sciences* **2006**, 5 (3), 317–325. <https://doi.org/10.1039/B513219C>.
- (16) Stamati, I.; Kuimova, M. K.; Lion, M.; Yahioğlu, G.; Phillips, D.; Deonarain, M. P. Novel Photosensitisers Derived from Pyropheophorbide-a: Uptake by Cells and Photodynamic Efficiency in Vitro. *Photochem Photobiol Sci* **2010**, 9 (7), 1033–1041. <https://doi.org/10.1039/c0pp00038h>.
- (17) Pandey, R. K.; Sumlin, A. B.; Constantine, S.; Aoudia, M.; Potter, W. R.; Bellnier, D. A.; Henderson, B. W.; Rodgers, M. A.; Smith, K. M.; Dougherty, T. J. Alkyl Ether Analogs of Chlorophyll-a Derivatives: Part 1. Synthesis, Photophysical Properties and Photodynamic

- Efficacy. *Photochemistry and Photobiology* **1996**, 64 (1), 194–204.  
<https://doi.org/10.1111/j.1751-1097.1996.tb02442.x>.
- (18) Liu, Q.; Wang, J.; Li, S.; Li, G.; Chen, Q.; Hong, Z. Folate-Targeted Polyethylene Glycol–Modified Photosensitizers for Photodynamic Therapy. *Journal of Pharmaceutical Sciences* **2019**, 108 (6), 2102–2111. <https://doi.org/10.1016/j.xphs.2019.01.014>.
- (19) Choi, K. Y.; Saravanakumar, G.; Park, J. H.; Park, K. Hyaluronic Acid-Based Nanocarriers for Intracellular Targeting: Interfacial Interactions with Proteins in Cancer. *Colloids Surf B Biointerfaces* **2012**, 99, 82–94.  
<https://doi.org/10.1016/j.colsurfb.2011.10.029>.
- (20) Jin, C. S.; Zheng, G. Liposomal Nanostructures for Photosensitizer Delivery. *Lasers Surg Med* **2011**, 43 (7), 734–748. <https://doi.org/10.1002/lsm.21101>.
- (21) Li, L.; Huh, K. M. Polymeric Nanocarrier Systems for Photodynamic Therapy. *Biomaterials Research* **2014**, 18 (1), 19. <https://doi.org/10.1186/2055-7124-18-19>.
- (22) Lee, S. J.; Park, K.; Oh, Y.-K.; Kwon, S.-H.; Her, S.; Kim, I.-S.; Choi, K.; Lee, S. J.; Kim, H.; Lee, S. G.; Kim, K.; Kwon, I. C. Tumor Specificity and Therapeutic Efficacy of Photosensitizer-Encapsulated Glycol Chitosan-Based Nanoparticles in Tumor-Bearing Mice. *Biomaterials* **2009**, 30 (15), 2929–2939.  
<https://doi.org/10.1016/j.biomaterials.2009.01.058>.
- (23) Pais-Silva, C.; de Melo-Diogo, D.; Correia, I. J. IR780-Loaded TPGS-TOS Micelles for Breast Cancer Photodynamic Therapy. *European Journal of Pharmaceutics and Biopharmaceutics* **2017**, 113, 108–117. <https://doi.org/10.1016/j.ejpb.2017.01.002>.

- (24) Yang, X.-Y.; Li, Y.-X.; Li, M.; Zhang, L.; Feng, L.-X.; Zhang, N. Hyaluronic Acid-Coated Nanostructured Lipid Carriers for Targeting Paclitaxel to Cancer. *Cancer Lett* **2013**, *334* (2), 338–345. <https://doi.org/10.1016/j.canlet.2012.07.002>.
- (25) Downie, J. B.; Grimes, P. E.; Callender, V. D. A Multicenter Study of the Safety and Effectiveness of Hyaluronic Acid with a Cohesive Polydensified Matrix for Treatment of Nasolabial Folds in Subjects with Fitzpatrick Skin Types IV, V, and VI. *Plastic and Reconstructive Surgery* **2013**, *132* (4S-2), 41S. <https://doi.org/10.1097/PRS.0b013e318299ff53>.
- (26) Iannitti, T.; Elhensheri, M.; Bingöl, A. O.; Palmieri, B. Preliminary Histopathological Study of Intra-Articular Injection of a Novel Highly Cross-Linked Hyaluronic Acid in a Rabbit Model of Knee Osteoarthritis. *J Mol Histol* **2013**, *44* (2), 191–201. <https://doi.org/10.1007/s10735-012-9457-4>.
- (27) Rios de la Rosa, J. M.; Tirella, A.; Gennari, A.; Stratford, I. J.; Tirelli, N. The CD44-Mediated Uptake of Hyaluronic Acid-Based Carriers in Macrophages. *Adv Healthc Mater* **2017**, *6* (4). <https://doi.org/10.1002/adhm.201601012>.
- (28) Shigeishi, H.; Higashikawa, K.; Takechi, M. Role of Receptor for Hyaluronan-Mediated Motility (RHAMM) in Human Head and Neck Cancers. *J Cancer Res Clin Oncol* **2014**, *140* (10), 1629–1640. <https://doi.org/10.1007/s00432-014-1653-z>.
- (29) Song, J. M.; Im, J.; Nho, R. S.; Han, Y. H.; Upadhyaya, P.; Kassie, F. Hyaluronan-CD44/RHAMM Interaction-Dependent Cell Proliferation and Survival in Lung Cancer Cells. *Molecular Carcinogenesis* **2019**, *58* (3), 321–333. <https://doi.org/10.1002/mc.22930>.

- (30) Banerji, S.; Ni, J.; Wang, S. X.; Clasper, S.; Su, J.; Tammi, R.; Jones, M.; Jackson, D. G. LYVE-1, a New Homologue of the CD44 Glycoprotein, Is a Lymph-Specific Receptor for Hyaluronan. *J Cell Biol* **1999**, *144* (4), 789–801. <https://doi.org/10.1083/jcb.144.4.789>.
- (31) Rousset, N.; Vonarx, V.; Eléouet, S.; Carré, J.; Kerninon, E.; Lajat, Y.; Patrice, T. Effects of Photodynamic Therapy on Adhesion Molecules and Metastasis. *J Photochem Photobiol B* **1999**, *52* (1–3), 65–73. [https://doi.org/10.1016/s1011-1344\(99\)00104-9](https://doi.org/10.1016/s1011-1344(99)00104-9).
- (32) Zhou, A.; Wei, Y.; Wu, B.; Chen, Q.; Xing, D. Pyropheophorbide A and c(RGDyK) Comodified Chitosan-Wrapped Upconversion Nanoparticle for Targeted Near-Infrared Photodynamic Therapy. *Mol. Pharmaceutics* **2012**, *9* (6), 1580–1589. <https://doi.org/10.1021/mp200590y>.
- (33) Duan, Y.; Li, X.; Zuo, X.; Shen, T.; Yu, S.; Deng, L.; Gao, C. Migration of Endothelial Cells and Mesenchymal Stem Cells into Hyaluronic Acid Hydrogels with Different Moduli under Induction of Pro-Inflammatory Macrophages. *J. Mater. Chem. B* **2019**, *7* (36), 5478–5489. <https://doi.org/10.1039/C9TB01126A>.
- (34) Kavakka, J. S.; Heikkinen, S.; Kilpeläinen, I.; Mattila, M.; Lipsanen, H.; Helaja, J. Noncovalent Attachment of Pyro-Pheophorbide a to a Carbon Nanotube. *Chem. Commun.* **2007**, No. 5, 519–521. <https://doi.org/10.1039/B611461J>.
- (35) Hokputsa, S.; Jumel, K.; Alexander, C.; Harding, S. E. A Comparison of Molecular Mass Determination of Hyaluronic Acid Using SEC/MALLS and Sedimentation Equilibrium. *Eur Biophys J* **2003**, *32* (5), 450–456. <https://doi.org/10.1007/s00249-003-0299-6>.
- (36) Savellano, M. D.; Pogue, B. W.; Hoopes, P. J.; Vitetta, E. S.; Paulsen, K. D. Multiepitope HER2 Targeting Enhances Photoimmunotherapy of HER2-Overexpressing Cancer Cells

- with Pyropheophorbide-a Immunoconjugates. *Cancer Res* **2005**, *65* (14), 6371–6379.  
<https://doi.org/10.1158/0008-5472.CAN-05-0426>.
- (37) Lin, H.; Shen, Y.; Chen, D.; Lin, L.; Wilson, B. C.; Li, B.; Xie, S. Feasibility Study on Quantitative Measurements of Singlet Oxygen Generation Using Singlet Oxygen Sensor Green. *J Fluoresc* **2013**, *23* (1), 41–47. <https://doi.org/10.1007/s10895-012-1114-5>.
- (38) Gollmer, A.; Arnbjerg, J.; Blaikie, F. H.; Pedersen, B. W.; Breitenbach, T.; Daasbjerg, K.; Glasius, M.; Ogilby, P. R. Singlet Oxygen Sensor Green®: Photochemical Behavior in Solution and in a Mammalian Cell. *Photochemistry and Photobiology* **2011**, *87* (3), 671–679. <https://doi.org/10.1111/j.1751-1097.2011.00900.x>.
- (39) Kessel, D.; Luo, Y.; Mathieu, P.; Reiners, J. J. Determinants of the Apoptotic Response to Lysosomal Photodamage. *Photochem Photobiol* **2000**, *71* (2), 196–200.  
[https://doi.org/10.1562/0031-8655\(2000\)071<0196:dotart>2.0.co;2](https://doi.org/10.1562/0031-8655(2000)071<0196:dotart>2.0.co;2).
- (40) Cai, S.; Xie, Y.; Davies, N. M.; Cohen, M. S.; Forrest, M. L. Carrier-Based Intralymphatic Cisplatin Chemotherapy for the Treatment of Metastatic Squamous Cell Carcinoma of the Head & Neck. *Ther Deliv* **2010**, *1* (2), 237–245. <https://doi.org/10.4155/tde.10.38>.
- (41) Wu, M.; Du, Y.; Liu, Y.; He, Y.; Yang, C.; Wang, W.; Gao, F. Low Molecular Weight Hyaluronan Induces Lymphangiogenesis through LYVE-1-Mediated Signaling Pathways. *PLOS ONE* **2014**, *9* (3), e92857. <https://doi.org/10.1371/journal.pone.0092857>.
- (42) Yoon, H. Y.; Koo, H.; Choi, K. Y.; Lee, S. J.; Kim, K.; Kwon, I. C.; Leary, J. F.; Park, K.; Yuk, S. H.; Park, J. H.; Choi, K. Tumor-Targeting Hyaluronic Acid Nanoparticles for Photodynamic Imaging and Therapy. *Biomaterials* **2012**, *33* (15), 3980–3989.  
<https://doi.org/10.1016/j.biomaterials.2012.02.016>.

- (43) Choi, K. Y.; Chung, H.; Min, K. H.; Yoon, H. Y.; Kim, K.; Park, J. H.; Kwon, I. C.; Jeong, S. Y. Self-Assembled Hyaluronic Acid Nanoparticles for Active Tumor Targeting. *Biomaterials* **2010**, *31* (1), 106–114. <https://doi.org/10.1016/j.biomaterials.2009.09.030>.
- (44) Li, F.; Bae, B.-C.; Na, K. Acetylated Hyaluronic Acid/Photosensitizer Conjugate for the Preparation of Nanogels with Controllable Phototoxicity: Synthesis, Characterization, Autophotoquenching Properties, and in Vitro Phototoxicity against HeLa Cells. *Bioconjug Chem* **2010**, *21* (7), 1312–1320. <https://doi.org/10.1021/bc100116v>.
- (45) Kessel, D.; Oleinick, N. L. Photodynamic Therapy and Cell Death Pathways. *Methods Mol Biol* **2010**, *635*, 35–46. [https://doi.org/10.1007/978-1-60761-697-9\\_3](https://doi.org/10.1007/978-1-60761-697-9_3).
- (46) Kwiatkowski, S.; Knap, B.; Przystupski, D.; Saczko, J.; Kędzierska, E.; Knap-Czop, K.; Kotlińska, J.; Michel, O.; Kotowski, K.; Kulbacka, J. Photodynamic Therapy – Mechanisms, Photosensitizers and Combinations. *Biomedicine & Pharmacotherapy* **2018**, *106*, 1098–1107. <https://doi.org/10.1016/j.biopha.2018.07.049>.
- (47) Wang, S.; Gao, R.; Zhou, F.; Selke, M. Nanomaterials and Singlet Oxygen Photosensitizers: Potential Applications in Photodynamic Therapy. **2004**. <https://doi.org/10.1039/B311429E>.
- (48) Liu, H.; Zhao, M.; Wang, J.; Pang, M.; Wu, Z.; Zhao, L.; Yin, Z.; Hong, Z. Photodynamic Therapy of Tumors with Pyropheophorbide-a-Loaded Polyethylene Glycol–Poly(Lactic-Co-Glycolic Acid) Nanoparticles. *Int J Nanomedicine* **2016**, *11*, 4905–4918. <https://doi.org/10.2147/IJN.S112541>.
- (49) Duvvuri, M.; Krise, J. P. A Novel Assay Reveals That Weakly Basic Model Compounds Concentrate in Lysosomes to an Extent Greater Than PH-Partitioning Theory Would Predict. *Mol. Pharmaceutics* **2005**, *2* (6), 440–448. <https://doi.org/10.1021/mp050043s>.

- (50) Kessel, D.; Luguya, R.; Vicente, M. G. H. Localization and Photodynamic Efficacy of Two Cationic Porphyrins Varying in Charge Distribution¶. *Photochemistry and Photobiology* **2003**, 78 (5), 431–435. [https://doi.org/10.1562/0031-8655\(2003\)0780431LAPEOT2.0.CO2](https://doi.org/10.1562/0031-8655(2003)0780431LAPEOT2.0.CO2).
- (51) Hwang, H. S.; Shin, H.; Han, J.; Na, K. Combination of Photodynamic Therapy (PDT) and Anti-Tumor Immunity in Cancer Therapy. *Journal of Pharmaceutical Investigation* **2018**, 48 (2), 143–151. <https://doi.org/10.1007/s40005-017-0377-x>.
- (52) Zhang, T.; Abdelaziz, M. M.; Cai, S.; Yang, X.; Aires, D. J.; Forrest, M. L. Hyaluronic Acid Carrier-Based Photodynamic Therapy for Head and Neck Squamous Cell Carcinoma. *Photodiagnosis and Photodynamic Therapy* **2022**, 37, 102706. <https://doi.org/10.1016/j.pdpdt.2021.102706>.